DEPARTMENT OF AEROSPACE ENGINEERING COLLEGE OF ENGINEERING AND TECHNOLOGY OLD DOMINION UNIVERSITY NORFOLK, VA 23529

# DEVELOPMENT OF A THREE-DIMENSIONAL PSE CODE FOR COMPRESSIBLE FLOWS

#### By

Dr. P. Balakumar, Principal Investigator Department of Aerospace Engineering

## FINAL REPORT

For the period ending December 31, 1998

### Prepared for

NASA Langley Research Center Attn.: Ms. Barbara S. Thomson Grants Officer Mail Stop 126 Hampton, VA 23681-2199

#### Under

Research Grant NAG-1-2054 ODURF File No. 182431

February 1999

#### **ABSTRACT**

# STABILITY OF THREE-DIMENSIONAL COMPRESSIBLE BOUNDARY LAYERS.

Samarasingham Jeyasingham Old Dominion University, 1999 Director: Dr. P. Balakumar

A program is developed to investigate the linear stability of three-dimensional compressible boundary layer flows over bodies of revolutions. The problem is formulated as a 2D eigenvalue problem incorporating the meanflow variations in the normal and azimuthal directions. Normal mode solutions are sought in the whole plane rather than in a line normal to the wall as is done in the classical 1D stability theory. The stability characteristics of a supersonic boundary layer over a sharp cone with 5° half-angle at 2° angle of attack is investigated. The 1D eigenvalue computations showed that the most amplified disturbances occur around  $x_2 = 90^{\circ}$ and the azimuthal mode number for the most amplified disturbances range between m = -30 to -40. The frequencies of the most amplified waves are smaller in the middle region where the crossflow dominates the instability than the most amplified frequencies near the windward and leeward planes. The 2D eigenvalue computations showed that due to the variations in the azimuthal direction, the eigenmodes are clustered into isolated confined regions. For some eigenvalues, the eigenfunctions are clustered in two regions. Due to the nonparallel effect in the azimuthal direction, the eigenmodes are clustered into isolated confined regions. For some eigenvalues, the eigenfunctions are clustered in two regions. Due to the nonparallel effect in the azimuthal direction, the most amplified disturbances are shifted to 120° compared to 90° for the parallel theory. It is also observed that the nonparallel amplification rates are smaller than that is obtained from the parallel theory.

The format of this thesis is based on American Institute of Aeronautics and Astronautics Journal and was typeset in IAT<sub>E</sub>X 2<sub>ε</sub> by the author.

#### ACKNOWLEDGEMENTS

I would like to express my most sincere respect and appreciation to my faculty advisor, Professor Ponnampalam Balakumar. I owe a debt of gratitude to him for his technical guidance, genuine interest and motivation during the course of this study. Most of the background material has been derived from the lectures and works of Dr. P. Balakumar.

I also wish to express my special thanks for the dissertation committee, Prof Oktay Baysal of Old Dominion University and Dr. Richard A. Thompson of NASA Langley, Virginia for their time in reviewing this dissertation and valuable comments.

This work was supported by the NASA Langley Research Center, Aerodynamic Branch, under the grant NAG-1-2054. The computations are performed on the SUN workstations at ICASE/NASA Langley Research Center in Hampton, Virginia.

I want to thank my parents, brothers and sisters for enduring love and support.

Finally, I want to convey my deepest thanks to my classmates Dr. E. Janke and K. Ghayour for thier valuable suggestions and stimulating discussions and my friends for their care and encouragement.

# TABLE OF CONTENTS

ABSTR	ACT		i
ACKNO	)WLE	DGEMENTS	i
TABLE	OF C	ONTENTS	iii
LIST O	F TAF	BLES	v
LIST O	F FIG	URES	vi
CHAP'	rer 1	:INTRODUCTION	1
CHAP	TER 2	: FORMULATION	17
2.1		lation of the Stability Theory	18
	2.1.1	Governing Equations	19
	2.1.2	Linearization of the equations	23
	2.1.3	Nondimensionalization of the Equations	25
	2.1.4	Reduction of the Number of Variables	26
	2.1.5	Introduction of Harmonic Disturbances	28
	2.1.6	Boundary Conditions	30
	2.1.7	Linear Stability Equations	30
2.2		rical Method and Solution Procedures	
	2.2.1	1D Eigenvalue Problem	33
	2.2.2	2D Eigenvalue Problem	37
	2.2.3	Global Method	40
	2.2.4	Local Method	4.
2.3	Sumr	nary	. 4
СПУІ	OTER	3: MEANFLOW COMPUTATIONS	4
3.1	TI N	S3D	. 4
	Bour	dary-layer Profiles	. 5

	3.2.1 Computation of Viscosity and Coefficient of thermal Conduc-	
	tivity	73
CHAP	TER 4: RESULTS AND DISCUSSION	74
4.1	1D Eigenvalue problem	74
4.2	2D Eigenvalue Problem	101
CHAF	PTER 5: CONCLUSIONS	176
5.1	Recommendations for the future work	177
BIBLI	OGRAPHY	179

## LIST OF TABLES

3.1	Details of the cone problem	50
4.1	Parameters used in nondimensionalization of different scales	76
	The waveangles for the most amplified wave at different $x_2$ locations.	

## LIST OF FIGURES

1.1	Schematic of velocity components within a swept-wing boundary	
	layer illustrating the definition of the cross-flow velocity (Reed &	
	Saric)	3
1.2	Flow visualization for a spinning cone (Kobayashi et al. 1983)	14
1.3	Naphthalene surface patterns illustrating cross-flow vortices (Saric &	
	Yeates 1985). Flow is from left to right.	15
1.4	Flow visualization for a rotating sphere: spiral streaks are observed,	
	then the secondary instability superposed on the vortices, then tran-	
	sition (Kohama & Kobayashi 1983b).	15
1.5	Flow visualization illustrating the spiral vortices on a disk (Kohama	
	1984a)	16
2.1	Orthogonal curvilinear coordinate system	19
2.2	The coordinate system for the cone located in a supersonic flow at an	1
	angle of attack $(M_{\infty} = 3.5)$	32
2.3	Block penta-diagonal system	36
2.4	Stability problem formulation	45
3.1	The coordinate system for the cone located in a supersonic flow at	
	an angle of attack $(M_{\infty} = 3.5)$	47
3.2	Schematic diagram of cross-flow and streamwise velocity profile (Reed	
	& Saric)	51
3.3	The variation of boundary-layer thickness in the azimuthal direction	
	at different streamwise locations.	54
3.4	The variation of boundary-layer edge velocity in the azimuthal direc-	
	tion at different streamwise locations.	55
3.5	Mean velocity profiles in the direction of the inviscid streamlines. (Re	
	$= 531, x_1 = 0.033m$ )	56
3.6	Cross-flow velocity profiles (Re = 531, $x_1 = 0.033m$ )	57

3.7	Azimuthal velocity distributions at different $x_2$ locations. (Re =	
	531, $x_1 = 0.033m$ )	58
3.8	Mean density variation in the normal direction at different $x_2$ loca-	
	tions. (Re = 531, $x_1 = 0.033m$ )	59
3.9	Mean temperature variation in the normal direction at different $x_2$	
	locations. (Re = 531, $x_1 = 0.033m$ )	60
3.10	The distribution of Fourier components of $a$ ) streamwise velocity, $b$ )	
	azimuthal velocity and $c$ ) temperature with Fourier modes $m.\ .\ .\ .$	61
3.11	Mean velocity profiles in the direction of the inviscid streamlines. (Re	
	$= 1823, x_1 = 0.3505m$ )	62
3.12	Cross-flow velocity profiles. (Re = 1823, $x_1 = 0.3505m$ )	63
3.13	Azimuthal velocity distributions at different $x_2$ locations (Re = 1823, $x_1$	=
	0.3505m)	64
3.14	Mean density variation in the normal direction at different $x_2$ loca-	
	tions ( $Re = 2211, x_1=0.5105m$ )	65
3.15	Mean temperature variation in the normal direction at different $x_2$	
	locations (Re = 2211, $x_1 = 0.3505m$ )	66
3.16	Mean velocity profiles in the direction of the inviscid streamlines. Re	
	$= 2211, x_1 = 0.5105m$ )	67
3.17	Cross-flow velocity profiles. (Re = 2211, $x_1 = 0.5105m$ )	68
3.18	Azimuthal velocity distributions at different $x_2$ locations. (Re =	
	$2211, x_1 = 0.5105m$ )	69
3.19	Mean density variation in the normal direction at different $x_2$ (Re	
	$= 2211, x_1 = 0.5105m). \dots$	70
3.20	Mean temperature variation in the normal direction at different $x_2$	7.1
	$(\text{Re} = 2211, \ x_1 = 0.5105m). \ \dots \dots \dots \dots \dots \dots$	71
3.21	Contours of cross-flow Reynolds numbers along the cone	72
4.1	Schematic diagram of the flow and the wave directions	75
4.2	:The variation of temporal amplification rate $\omega_i$ and temporal fre-	0.1
	quency $\omega_r$ with streamwise wavenumber $\alpha$ . $(x_1 = 0.033m)$	81
4.3	:The variation of temporal amplification rate $\omega_i$ and temporal fre-	00
	quency $\omega_r$ with streamwise wavenumber $\alpha$ . $(x_1 = 0.033m)$	. 82

4.4	: Distribution of temporal amplification rate $(\omega_i)$ with $x_2$ (streamwise	
	location $x_1 = 0.033m$ , $\alpha = 0.05$ )	83
4.5	:Distribution of temporal frequency $(\omega_r)$ with $x_2$ (streamwise location	
	$x_1 = 0.033m, \ \alpha = 0.05$ )	84
4.6	:Distribution of temporal amplification rate $\omega_i$ with $x_2$ . $(x_1 = 0.033m,$	
	$\alpha = 0.07$ )	85
4.7	:Distribution of temporal frequency $(\omega_r)$ with $x_2$ (streamwise location	
	$x_1 = 0.033m,  \alpha = 0.07$ )	86
4.8	The variation of temporal amplification rate $\omega_i$ and temporal fre-	
1.0	quency $\omega_r$ with streamwise wavenumber $\alpha$ . $(x_1 = 0.1978m)$	87
4.9	The variation of temporal amplification rate $\omega_i$ and temporal fre-	
1.0	quency $\omega_r$ with streamwise wavenumber $\alpha$ . $(x_1 = 0.1978m)$	88
4.10	Distribution of temporal amplification rate $(\omega_i)$ with $x_2$ . (streamwise	
1.10	location $x_1 = 0.197m$ , $\alpha = 0.07$ )	89
4.11	Distribution of temporal frequency $(\omega_r)$ with $x_2$ ( $x_1 = 0.197m$ , $\alpha =$	
1.11	0.07)	90
4.12	The variation of temporal amplification rate $\omega_i$ and temporal fre-	
1.12	quency $\omega_r$ with streamwise wavenumber $\alpha$ . $(x_1 = 0.3505m)$	91
4.13	$\omega$ and temporal fre-	
4.10	quency $\omega_r$ with streamwise wavenumber $\alpha$ . $(x_1 = 0.3505m)$	92
4.14	$\omega$ and temporal fre-	
4.11	guency $\omega_r$ with streamwise wavenumber $\alpha$ . $(x_1 = 0.3505m)$	93
4.15	$x_2$ . (streamwise)	
1.10	location $x_1 = 0.3505m$ , $\alpha = 0.07$ )	94
4.16	$(x_1 = 0.3505m)$	
7.11	lpha = 0.07)	95
4.1	$\omega_r$ .	
4.1	$(x_1 = 0.3505m, \ \alpha = 0.07).$	. 96
4 1	$\hat{u}_1$ along	
4.1	azimuthal direction. $(x_1 = 0.3505m)$	. 97
4.1	$\hat{\mu}_{i}$ along azimuthal direction.	
4.1	$(x_{r}-0.3505m)$	. 98

4.20	The variation of temporal amplification rate $\omega_i$ and temporal frequency $\omega_r$ with streamwise wavenumber $\alpha$ . $(x_1 = 0.5105m)$	99
4.21	:Distribution of temporal amplification rate $\omega_i$ with $x_2$ . $(x_1 = 0.5105m, \alpha = 0.07)$	100
4.22	:Distribution of temporal frequency $(\omega_r)$ with $x_2$ (streamwise location $x_1 = 0.5105m, \ \alpha = 0.07$ )	100
4.23	Case 1: The distribution of eigenfunction and Fourier components for a symmetric mode with frequency $f=21$ kHz. ( $\omega=(0.0386, 0.00437)$ , $\alpha=0.07$ . ( $x_1=0.3505m$ and $Re=1823$ )	109
4.24	Case 1: Contour plot of streamwise velocity disturbance. (frequency $f=21$ kHz, $\omega=(0.0386,0.00437),\alpha=0.07,x_1=0.3505m$ and $Re=1823$ ).	110
4.25	Case 1: The distribution of disturbance profiles along the azimuthal direction. (frequency $f=21$ kHz, $\omega=(0.0386,0.00437)$ and $\alpha=0.07,x_1=0.3505m$ and $Re=1823)$	111
4.26	Case 2: The distribution of eigenfunction and Fourier components for a symmetric mode with frequency $f=22.9$ kHz. ( $\omega=(0.04205, 0.00272)$ ), $\alpha=0.07, x_1=0.3505m$ and $Re=1823$ )	112
4.27	Case 2: Contour plot of streamwise velocity disturbance $ \hat{u}_1 $ . (frequency $f=22.9$ kHz, $\omega=(0.04205,\ 0.00272),\ \alpha=0.07,\ x_1=0.3505m$ and $Re=1823$ )	113
4.28	Case 3: The distribution of eigenfunction and Fourier components for a symmetric mode with frequency $f=26.8$ kHz. ( $\omega=(0.0491, 0.0026)$ ), $\alpha=0.07$ , $x_1=0.3505m$ and $Re=1823$ )	114
4.29	Case 2: Contour plot of streamwise velocity disturbance $ \hat{u}_1 $ . (frequency $f=26.8$ kHz, $\omega=(0.0491,0.0026),\alpha=0.07,x_1=0.3505m$ and $Re=1823$ )	. 115
4.30		

4.31	Case 4: The distribution of Fourier components of streamwise ve-	
	locity disturbance $ u_{1f} $ with Fourier modes $m$ at different heights.	
	(frequency $f=22.87 \text{ kHz}, \ \omega=(0.0419,\ 0.00349), \ \alpha=0.07,\ x_1=0.07$	
	0.3505m  and  Re = 1823 )	117
4.32	Case 4: Contour plot of streamwise velocity disturbance. (frequency	
	$f=22.87~{\rm kHz},~\omega=(0.0419,~0.00349),~\alpha=0.07,~x_1=0.3505m$ and	
	Re = 1823)	118
4.33	Case 5: The distribution of eigenfunction for a symmetric mode with	
	frequency $f=24.6$ kHz, $\omega=(0.0451,\ 0.00272),\ \alpha=0.07,\ x_1=$	
	$0.3505m \text{ and } Re = 1823) \dots \dots \dots \dots \dots \dots \dots$	119
4.34	Case 5: The distribution of Fourier components of streamwise ve-	
	locity disturbance $ u_{1f} $ with Fourier modes $m$ at different heights.	
	(frequency $f=24.6$ kHz, $\omega=(0.0451,\ 0.00272),\ \alpha=0.07,\ x_1=0.07$	
	0.3505m and $Re = 1823$ )	120
4.35	Case 5: Contour plot of streamwise velocity disturbance. (frequency	
	$f=24.6 \text{ kHz}, \ \omega=(0.0451,\ 0.00272),\ \alpha=0.07,\ x_1=0.3505m \ \text{and}$	
	Re = 1823 )	121
4.36	Case 6: The distribution of eigenfunction and Fourier components for	
	an anti-symmetric mode with frequency $f=23.81~\mathrm{kHz},\omega=(0.0437,$	
	$0.0025$ ), $\alpha = 0.07$ , $x_1 = 0.3505m$ and $Re = 1823$ )	122
4.37	Case 6: Contour plot of streamwise velocity disturbance $ \hat{u}_1 $ . (fre-	
	quency $f = 23.81$ kHz, $\omega = (0.0437, 0.0025), \alpha = 0.07, x_1 =$	
	0.3505m  and  Re = 1823)	123
4.38	Case 7: The distribution of eigenfunction for a symmetric mode with	
	frequency $f=23.71$ kHz. ( $\omega=(0.0434,\ 0.00316),\ \alpha=0.07,\ x_1=0.07$	
	$0.3505m \text{ and } Re = 1823) \dots \dots \dots \dots \dots \dots \dots \dots \dots$	124
4.39	Case 7: The distribution of Fourier components of streamwise ve-	
	locity disturbance $ u_{1f} $ with Fourier modes $m$ at different heights.	
	(frequency $f=23.71$ kHz, $\omega=(0.0434,\ 0.00316),\ \alpha=0.07,\ x_1=0.07$	
	$0.3505m \text{ and } Re = 1823) \dots \dots \dots \dots \dots \dots \dots$	125
4.40	Case 7: Contour plot of streamwise velocity disturbance. (frequency	
	$f = 23.71 \text{ kHz}, \ \omega = (0.0434, \ 0.00316), \ \alpha = 0.07, \ x_1 = 0.3505m \ \text{and}$	
	Re = 1823)	126

1.41	Case 7: The distribution of streamwise velocity perturbation profiles along the azimuthal direction. (frequency $f=23.71$ kHz, $\omega=(0.0434,0.00316),\alpha=0.07,x_1=0.3505m$ and $Re=1823)$ 127
1.42	Case 7: Unstable eigenvalue spectrums of a) 2D eigenvalue method and b) 1D (hollow symbols) and 2D (solid symbols) eigenvalue methods. ( $\alpha=0.07, x_1=0.3505m$ and $Re=1823$ )
4.43	Case 1: The distribution of eigenfunction and Fourier components for a symmetric mode with frequency $f = 65.8 \text{ kHz}$ . ( $\omega = (0.0391, 0.00128)$ ) and $\alpha = 0.07, x_1 = 0.033m, Re = 531)$ 129
4.44	Case 1: Contour plot of streamwise velocity disturbance $ \hat{u}_1 $ . (frequency $f = 65.8$ kHz, $\omega = (0.0391, 0.00128)$ , $\alpha = 0.07, x_1 = 0.033m$ and $Re = 531$ )
4.45	Case 1: The distribution of disturbance profiles along the azimuthal direction. (frequency $f=65.8$ kHz, $\omega=(0.0391,0.00128)$ , $\alpha=0.07$ , $x_1=0.033m$ and $Re=531$ )
4.46	Case 2: The distribution of eigenfunction and Fourier components for a symmetric mode with frequency $f=65.1$ kHz. ( $\omega=(0.0388, 0.00311)$ and $\alpha=0.07, x_1=0.033m, Re=531)$
4.47	Case 2: Contour plot of streamwise velocity disturbance $ \hat{u}_1 $ . (frequency $f = 65.1$ kHz, $\omega = (0.0388, 0.00311)$ , $\alpha = 0.07, x_1 = 0.033m$ and $Re = 531$ )
4.48	Case 3: The distribution of eigenfunction for a symmetric mode with frequency $f=110.4$ kHz. ( $\omega=(0.0656,\ 0.000114),\ \alpha=0.1,\ x_1=0.033m$ and $Re=531)$
4.49	Case 3: The distribution of Fourier components of streamwise velocity disturbance $ u_{1f} $ with Fourier modes $m$ at different heights. (frequency $f = 110.4$ kHz, $\omega = (0.0656, 0.000114)$ , $\alpha = 0.1$ , $x_1 =$
4.50	0.033m and $Re = 531$ )

4.51	Case 3: The distribution of temperature perturbation profiles along	
	the azimuthal direction. (frequency $f=110.4~\mathrm{kHz},~\omega=(0.0656,$	
	$0.000114$ ), $\alpha = 0.1$ , $x_1 = 0.033m$ and $Re = 531$ )	137
4.52		
	frequency $f = 107.6$ kHz. ( $\omega = (0.0639, 0.00094), \alpha = 0.1, x_1 =$	
	0.033m, and $Re = 531$ )	138
4.53	Case 4: The distribution of Fourier components of streamwise veloc-	
	ity disturbance $ u_{1f} $ with Fourier modes $m$ at different heights. (fre-	
	quency $f = 107.6 \text{ kHz}, \ \omega = (0.0639, 0.00094), \ \alpha = 0.1, \ x_1 = 0.033m$	
	and $Re=531$ )	139
4.54	Case 5: The distribution of eigenfunction for a symmetric mode with	
	frequency $f = 84.8$ kHz. ( $\omega = (0.05039, 0.00164), \alpha = 0.08$ . (	
	$x_1 = 0.033m$ , and $Re = 531$ )	140
4.55	Case 5: The distribution of Fourier components of streamwise ve-	
	locity disturbance $ u_{1f} $ with Fourier modes $m$ at different heights.	
	(frequency $f = 84.8 \text{ kHz}, \ \omega = (0.05039, \ 0.00164), \ \alpha = 0.08, \ x_1 =$	
	0.033m and $Re = 531$ )	141
4.56	Case 5: The distribution of streamwise velocity perturbation pro-	
	files along the azimuthal direction. (frequency $f=84.8$ kHz, $\omega=$	
	$(0.05039, 0.00164), \alpha = 0.08, x_1 = 0.3505m \text{ and } Re = 531) \dots$	142
4.57	Case 5: The distribution of temperature perturbation profiles along	
	the azimuthal direction. (frequency $f=84.8~\mathrm{kHz},~\omega=(0.05039,$	
	0.00164), $\alpha = 0.08$ , $x_1 = 0.3505m$ and $Re = 531$ )	143
4.58	Case 6: The distribution of eigenfunction and Fourier components	
	for a symmetric mode with frequency $f=89.7$ kHz. ( $\omega=(0.0532,$	
	$0.0023$ ), $\alpha = 0.08$ , $x_1 = 0.033m$ and $Re = 531$ )	144
4.59	Case 6: The distribution of disturbance profiles along the azimuthal	
	direction. (frequency $f=89.7~\mathrm{kHz}, \omega=(0.0532,0.0023)$ and $\alpha=0.08,$	
	$x_1 = 0.033m \text{ and } Re = 531) \dots \dots \dots \dots \dots \dots$	145
4.60	Case 7: The distribution of eigenfunction for a symmetric mode with	
	frequency $f$ = 80.5 kHz. ( $\omega$ = (0.04785, 0.00137), $\alpha$ = 0.08, $x_1$ =	
	$0.033m \text{ and } Re = 531) \dots \dots \dots \dots \dots \dots$	146

4.61	Case 7: The distribution of Fourier components of streamwise ve-	
	locity disturbance $ u_{1f} $ with Fourier modes $m$ at different heights.	
	(frequency $f = 80.5 \text{ kHz}, \ \omega = (0.04785, \ 0.00137), \ \alpha = 0.08, \ x_1 =$	
	0.033m and $Re = 531$ )	147
4.62	Case 1: The distribution of eigenfunction and Fourier components for	
	a symmetric mode with frequency $f = 27.7 \text{ kHz}$ , $\omega = (0.0387, 0.00427)$ ,	
	$\alpha = 0.07, x_1 = 0.1978m \text{ and } Re = 1350) \dots$	148
4.63	Case 1: Contour plot of streamwise velocity disturbance. (frequency	
	$f = 27.7 \text{ kHz}, \ \omega = (0.0589, 0.00301), \ \alpha = 0.07, \ x_1 = 0.1978m \text{ and}$	
	Re = 1350 )	149
4.64	Case 2: The distribution of eigenfunction for a symmetric mode with	
	frequency $f=42.2$ kHz. ( $\omega=(0.0589,\ 0.00301),\ \alpha=0.09,\ x_1=0.00$	
	$0.1978m \text{ and } Re = 1350) \dots \dots \dots \dots \dots \dots$	150
4.65	Case 2: The distribution of Fourier components of streamwise ve-	
	locity disturbance $ u_{1f} $ with Fourier modes $m$ . (frequency $f=42.2$	
	kHz, $\omega = (0.0589, 0.00301), \alpha = 0.09, x_1 = 0.1978m$ and $Re = 1350$	
	)	151
4.66	Case 2: The distribution of streamwise velocity perturbation profiles	
	along the azimuthal direction. (frequency $f=42.2~\mathrm{kHz},\omega=(0.0589,$	
	$0.00301$ ), $\alpha = 0.09$ , $x_1 = 0.1978m$ and $Re = 1350$ )	152
4.67	Case 2: The distribution of temperature perturbation profiles along	
	the azimuthal direction. ( $\omega = (0.0589, 0.00301)$ and $\alpha = 0.09, x_1 =$	
	$0.1978m, Re = 1350) \dots \dots$	153
4.68	Case 3: The distribution of eigenfunction for a symmetric mode with	
	frequency $f = 41.05$ kHz, $\omega = (0.0572, 0.00348), \alpha = 0.09, x_1 =$	
	0.1978m, and $Re = 1350$ )	154
4.69	Case 3: The distribution of Fourier components of streamwise veloc-	
	ity disturbance $ u_{1f} $ with Fourier modes $m$ . (frequency $f=41.05$	
	kHz, $\omega = (0.0572, 0.00348)$ , $\alpha = 0.09, x_1 = 0.1978m$ and $Re = 1350$	
	)	155
4.70	Case 4: The distribution of eigenfunction and Fourier components	
	for a symmetric mode with frequency $f=43.36$ kHz, $\omega=(0.06056,$	
	$0.00328$ ), $\alpha = 0.08$ , $x_1 = 0.1978m$ and $Re = 1350$ )	156

4.71	Case 5: The distribution of eigenfunction and Fourier components
	for a symmetric mode with frequency $f=40.35$ kHz, $\omega=(0.0563,$
	$0.00131$ ), $\alpha = 0.09$ , $x_1 = 0.1978m$ and $Re = 1350$ ) 157
4.72	Case 6: The distribution of eigenfunction and Fourier components
	for a symmetric mode with frequency $f=41.14$ kHz. ( $\omega=(0.0574,$
	$0.00115$ ), $\alpha = 0.09$ , $x_1 = 0.1978m$ and $Re = 1350$ )
4.73	Case 6: Contour plot of streamwise velocity disturbance. (frequency
	$f = 41.14 \text{ kHz}, \ \omega = (0.0574, \ 0.00115), \ \alpha = 0.09, \ x_1 = 0.1978m \text{ and}$
	Re = 1350)
4.74	Case 6: The distribution of disturbance profiles along the azimuthal
	direction. (frequency $f=41.14~\mathrm{kHz}, \omega=(0.0574,0.00115)$ , $\alpha=0.09,$
	$x_1 = 0.1978m \text{ and } Re = 1350) \dots \dots$
4.75	Case 7: The distribution of eigenfunction and Fourier components
	for a symmetric mode with frequency $f = 39.16$ kHz. ( $\omega = (0.0546,$
	$0.00161$ ), $\alpha = 0.09$ , $x_1 = 0.1978m$ and $Re = 1350$ ) 161
4.76	Case 7: Contour plot of streamwise velocity disturbance. (frequency
	$f = 39.16 \text{ kHz}, \ \omega = (0.0546, 0.00161), \ \alpha = 0.09, \ x_1 = 0.1978m \text{ and}$
	Re = 1350)
4.77	Case 1: The distribution of eigenfunction and Fourier components
	for a symmetric mode with frequency $f=17.45~\mathrm{kHz},\omega=(0.0385,$
	$0.00445$ ), $\alpha = 0.07$ , $x_1 = 0.5105m$ and $Re = 2211$ ) 163
4.78	Case 1: Contour plot of streamwise velocity disturbance. (frequency
	$f = 17.45 \text{ kHz}, \ \omega = (0.0385, \ 0.00445), \ \alpha = 0.07, \ x_1 = 0.5105 m \ \text{and}$
	Re = 2211)
4.79	Case 2: The distribution of eigenfunction and Fourier components for
	an anti-symmetric mode with frequency $f=19.2~\mathrm{kHz},\omega=(0.0423,$
	$0.00351$ ), $\alpha = 0.07$ , $x_1 = 0.5105m$ and $Re = 2211$ ) 165
4.80	
	$f = 19.2 \text{ kHz}, \ \omega = (0.0423, \ 0.00351), \ \alpha = 0.07, \ x_1 = 0.5105m \ \text{and}$
	Re = 2211)
4.81	Case 3: The distribution of eigenfunction and Fourier components
	for an anti-symmetric mode with frequency $f=19.04$ kHz. ( $\omega=1.07$
	$(0.0419, 0.00439), \alpha = 0.07, x_1 = 0.5105m \text{ and } Re = 2211) \dots 167$

4.82	Case 3: Contour plot of streamwise velocity disturbance $ \hat{u}_1 $ . (fre-	
	quency $f=19.04$ kHz, $\omega=(0.0419,~0.00439),~\alpha=0.07,~x_1=$	
	0.5105m  and  Re = 2211 )	168
4.83	Case 4: The distribution of eigenfunction for an anti-symmetric mode	
	with frequency $f=23.03$ kHz. ( $\omega=(0.0507,0.00288),\alpha=0.08,$	
	$x_1 = 0.5105m \text{ and } Re = 2211) \dots \dots \dots \dots \dots$	169
4.84	Case 4: The distribution of Fourier components of streamwise veloc-	
	ity disturbance $ u_{1f} $ with Fourier modes $m$ . (frequency $f=23.03$	
	kHz, $\omega = (0.0507, 0.00288)$ , $\alpha = 0.08, x_1 = 0.5105m$ and $Re = 2211$	
	)	170
4.85	Case 4: Contour plot of streamwise velocity disturbance $ \hat{u}_1 $ . (fre-	
	quency $f=23.03$ kHz, $\omega=(0.0507,~0.00288),~\alpha=0.08,~x_1=$	
	0.5105m and $Re=2211$ )	170
4.86	Case 5: The distribution of eigenfunction for an anti-symmetric mode	
	with frequency $f=22.04$ kHz. ( $\omega=(0.0486,0.00427),\alpha=0.08,$	
	$x_1 = 0.5105m \text{ and } Re = 2211)$	171
4.87	Case 5: The distribution of eigenfunction for an anti-symmetric mode	
	with frequency $f=22.04$ kHz. ( $\omega=(0.0486,0.00427),\alpha=0.08,$	
	$x_1 = 0.5105m \text{ and } Re = 2211) \dots \dots \dots \dots \dots \dots$	172
4.88		173
4.89	Case 5: Contour plot of streamwise velocity disturbance $ \hat{u}_1 $ . (fre-	
	quency $f=22.04$ kHz, $\omega=(0.0486,\ 0.00427),\ \alpha=0.08,\ x_1=$	
	0.5105m and $Re=2211$ )	173
4.91	Case 6: Contour plot of streamwise velocity disturbance $ \hat{u}_1 $ . (fre-	
	quency $f=23.45$ kHz, $\omega=(0.0517,\ 0.00411),\ \alpha=0.08,\ x_1=$	
	0.5105m and $Re = 2211$ )	174
4.90	Case 6: The distribution of eigenfunction and Fourier components	
	for an anti-symmetric mode with frequency $f=23.45$ kHz. ( $\omega=$	
	$(0.0517, 0.00411), \alpha = 0.08, x_1 = 0.5105m \text{ and } Re = 2211) \dots$	175

#### CHAPTER 1

#### INTRODUCTION

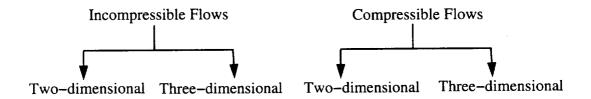
The transition of viscous flows from laminar to turbulent is one of the most challenging problems in fluid mechanics. In a typical commercial aircraft, 50 percent of the total drag force is due to the skin friction drag (Hefner and Bushnell [35] 1979). In supersonic and hypersonic vehicles, the equilibrium temperature on the surface determines the quality of material to be used in making the surfaces. Prediction of the transition onset point, the location at which the laminar boundary layer starts to become turbulent, is critical in the design of aerodynamic vehicles. The accurate prediction of the transition onset point is also very important in the application of the laminar flow control (LFC) methods to subsonic and supersonic aircrafts. Successful prediction of transition onset point depends on understanding the transition process and transferring the understandings onto a prediction tool.

Though there are several mechanisms and routes to go from a laminar to a turbulent state, in quiet environments all of them, in general, follow these fundamental processes.

- Receptivity
- Linear instability
- Nonlinear stability and saturation
- Secondary instability
- Breakdown to turbulence.

In the receptivity process, the unsteadiness in the environment and the inhomogeneities in the geometry generate instability waves inside the flow. In quiet environments, the initial amplitudes of these instability waves are small compared to any characteristic velocity and length scales in the flow. Goldstein [36] (1983) a) theoretically explained using asymptotic methods how the Tollmien-Schlichting waves (T-S waves) are generated near a leading edge of a flat plate by the long wavelength acoustic disturbances and in a companion paper [37] (1985 b) described the scattering of T-S waves from the acoustic disturbances by the streamwise variations in surface geometries. In the second stage, the amplitudes of these instability waves grow exponentially downstream and this process is governed by the linearized Navier-Stokes equations. Further downstream, the amplitude of the disturbances become large and the nonlinear effects inhibit the exponential growth and the amplitudes of the disturbances eventually saturate or attain singular values. In the next stage, these finite amplitude saturated disturbances become unstable to two and/or three dimensional disturbances. This is called secondary instability and can be analyzed using Floquet theory, Herbert (1988) [38]. Beyond this stage the spectrum broadens due to complex interactions and further instabilities and the flow becomes turbulent in a short distance downstream. In this thesis, we investigated the linear instability of three dimensional supersonic boundary layers over a sharp cone at an angle of attack.

Depending on the boundary layer profiles and flow parameters different types of linear instability waves are generated inside the boundary layers. For stability analyses, boundary layers can be divided into following groups.



In incompressible two-dimensional boundary layers, the disturbances may

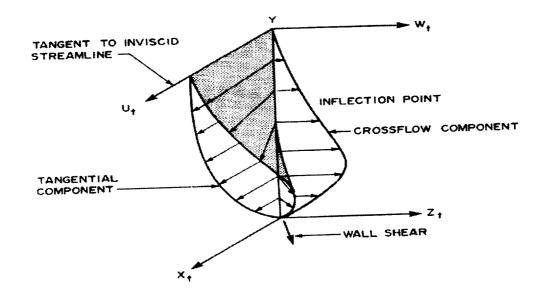


Fig. 1.1 Schematic of velocity components within a swept-wing boundary layer illustrating the definition of the cross-flow velocity (Reed & Saric).

take one of the following instability waves.

- (1) inviscid instability (Rayleigh instability)
- (2) viscous instability (Tollmien-Schlichting instability ).

Inviscid instability waves are generated by the interaction of inertia and pressure forces. This instability exists when the boundary layer contains an inflection point in the velocity distributions. The examples are boundary layer profiles in adverse pressure gradients, wakes, jets and in separated flows. Viscous instability waves are generated by the interaction of inertia, pressure and viscous forces. In this type of instability, energy is transferred from mean flow to the disturbance motion through the action of viscosity. Hence, these flows are inviscidly linearly stable but unstable to infinitesimal disturbances at finite Reynolds numbers. This instability is found in the plane Poiseuille flow and in boundary layer regions where pressure gradients are small, e.g, Blasius boundary layer.

Three-dimensional boundary layers are defined as the flows where the inviscid streamlines are curved. In a three-dimensional boundary layer, there exists another instability mode, called cross-flow instability. When the inviscid streamlines are curved, there exists a pressure gradient in the direction normal to the inviscid streamlines. Inside the boundary layer, due to the viscous effects, the velocity is smaller than that in the inviscid region. Hence, this pressure gradient causes a velocity component inside the boundary layer that is perpendicular to the inviscid-velocity vector. This component is called cross-flow. A schematic diagram showing different components of the velocity inside a boundary layer is given in figure 1.1. The cross-flow velocity profile has a maximum velocity somewhere in the middle of the boundary layer and goes to zero on the body surface and at the boundary layer edge, therefore exhibiting an inflection point. The description of the instability caused by the cross-flow was first given in the classic paper by Gergory, Walker, Stuart [40] (1956). When the cross-flow component is combined with the velocity component in the inviscid direction, they form a mean velocity profile that has an inflection point at which the velocity is zero. This permits a neutral disturbance with zero frequency. This neutral disturbance appears as vortices that all rotate in the same direction and take on the form of the familiar "cat's eye" structure when viewed in the stream direction. This phenomena is observed in several flow geometries such as rotating cones (figure 1.2), swept wings (figure 1.3), spheres (figure 1.4) and rotating disks (figure 1.5).

The stability characteristics of compressible two-dimensional and axi-symmetric boundary layers have been thoroughly investigated (Lees and Lin (1946) [41], Lees and Reshotko(1962) [42], Mack(1969) [43], Gaponov(1981) [44], Malik and Spall(1991) [45]). The main conclusions that are drawn from these investigations can be summarized as follows. (1) The quantity  $(\rho'U)' = \frac{d}{dy}(\rho \frac{dU}{dy})$ , where  $\rho$  and U are the density and the streamwise velocity distributions of the meanflow and y the

coordinate normal to the wall, plays the same role in the compressible stability theory as U'' does in the incompressible theory. The location where  $(\rho'U)'=0$  is called the "Generalized inflection point". In most of the compressible boundary layers, the density profile has an inflection point  $\rho''=0$  and due to this compressible boundary layers exhibit generalized inflection points. As a consequence, the flat-plate/ cone compressible boundary layers are unstable to purely inviscid disturbances. This is one of the important difference between the instability of incompressible and compressible flows. (2) When the mean flow relative to the neutral disturbance phase velocity becomes supersonic over some portion of the boundary layer, there exist several unstable modes. For two-dimensional disturbances, it is the first of the additional modes, called the second mode, which is the most unstable at all Mach numbers for which the relative flow is supersonic. (3) At higher Mach numbers, the viscosity has only a stabilizing influence on the boundary layer. (4) Considering three-dimensional disturbances, the amplification rate of the first mode increases while the amplification rate of the higher modes decreases with the increasing waveangles. In the inviscid limit, the phase velocity of the first mode varies from  $1-\frac{1}{M}$  to  $C_s$ , where M is the free stream Mach number and  $C_s$  is the mean flow velocity at which the generalized inflection  $(\rho'U)'=0$  occurs. To have unstable first mode disturbances the generalized inflection point should appear above the mean velocity  $1-\frac{1}{M}$ . For the second mode, the phase velocity C varies from  $C_s$  to 1. At low Mach numbers there exists no supersonic region near the wall relative to the phase velocity  $C_s$ , hence no second mode instability exists at low Mach numbers. The supersonic region first starts to appear in the inviscid limit at M=2.2 in an insulated flat plate boundary layer. The lowest Mach number at which the unstable second mode region has been located at finite Reynolds numbers is M=3. The second mode instability increases with increasing relative supersonic region.

Linear stability of axi-symmetric three-dimensional compressible boundary

layers were investigated by Balakumar and Reed (1991) [19]. As discussed previously, at low Mach numbers, in compressible flows the most amplified waves are oblique while in incompressible flows they are two-dimensional. This is due to the fact that in supersonic flows, the amplification rate increases with decreasing Mach numbers. Since in an oblique direction, the effective Mach number decreases hence the amplification rate increases for three-dimensional waves. For a free-stream Mach number of M = 3, the wave angle of the most amplified wave is inclined at about 55°. As described earlier, in incompressible flows the cross-flow velocity component introduces a new instability called "cross-flow instability" and the disturbances are inclined very close to the cross-flow direction. In compressible flows, the cross-flow basically increases the amplification rates of the first mode and makes the most amplified disturbances inclined more towards the cross-flow direction. Balakumar and Reed's calculation showed that the amplification rate of the first mode is increased by a factor of 2 to 4 due to the cross-flow compared with a two-dimensional flow and this increase decreases with increasing Mach number. It was also shown that the waveangles of the most amplified waves are increased by about 10° and the effect of the cross-flow on the second mode is as expected small.

In general three-dimensional boundary layers, the mean boundary layer profiles vary in all three directions: streamwise, spanwise or azimuthal and normal directions. However, in the high Reynolds number boundary layer flows the variations in the streamwise and in the spanwise directions are smaller than that in the normal directions. In the classical stability theory, these variations in the streamwise and in the spanwise directions are neglected and it is assumed that the boundary layer profiles vary only in the normal direction and uniform in the other two directions. This makes the coefficients of the linearized Navier-Stokes equations to be independent of the streamwise and spanwise coordinates and permit one to seek a

solution in the normal mode form

$$\Phi(x_1, x_2, x_3, t) = \Phi(x_3)e^{i\alpha x_1 + i\beta x_2 - i\omega t},$$
(1.1)

where  $x_1$ ,  $x_2$  and  $x_3$  are the coordinates in the streamwise, spanwise and in the normal directions, t is the time.  $\Phi(x_3)$  is the eigenfunction,  $\alpha, \beta$  are the wavenumbers in the streamwise and spanwise directions and  $\omega$  is the frequency. In general,  $\alpha, \beta$  and  $\omega$  are complex.

$$\alpha = \alpha_r + i\alpha_i \,, \tag{1.2}$$

$$\beta = \beta_r + i\beta_i \,, \tag{1.3}$$

$$\omega = \omega_r + i\omega_i \, \cdot \tag{1.4}$$

When the normal mode form Eq. 1.1 is substituted into the linearized Navier-Stokes equations, a homogeneous system of ordinary differential equations with homogeneous boundary conditions are obtained. The solution of which yields a dispersion relation among  $\alpha, \beta$  and  $\omega$  of the form

$$F(\alpha, \beta, \omega) = 0 {(1.5)}$$

The real and imaginary parts of the relation yield two equations in terms of the six unknown parameters  $(\alpha_r, \alpha_i)$ ,  $(\beta_r, \beta_i)$  and  $(\omega_r, \omega_i)$ . To determine these six unknowns one needs to specify four additional conditions. Two approaches are generally used to overcome these difficulties. One is called the temporal eigenvalue approach in which the wavenumbers  $\alpha, \beta$  are prescribed as real numbers and the complex frequency  $\omega$  is solved from the dispersion relation Eq. 1.5. The other method is called spatial eigenvalue approach in which the frequency  $\omega$  and the spanwise wavenumber  $\beta$  are prescribed as real numbers and the complex wavenumber  $\alpha$  is solved from the dispersion relation.

#### Temporal Problem

 $\alpha = \alpha_r$ , real prescribed

 $\beta = \beta_r$ , real prescribed

 $\omega = \omega_r + i\omega_i$ , solved from eigen relation

 $\omega_r$  = frequency of the disturbance

 $\omega_i$  = amplification rate of the disturbance in time

 $\omega_i < 0$ , the boundary layer is stable

= 0, the boundary layer is neutrally stable

> 0, the boundary layer is unstable

#### Spatial Problem

 $\omega = \omega_r$ , real prescribed

 $\beta = \beta_r$ , real prescribed

 $\alpha = \alpha_r + i\alpha_i$ , solved from eigen relation

 $\alpha_r$  = wavenumber in the streamwise direction

 $-\alpha_i$  = growth rate in the streamwise direction

 $-\alpha_i < 0$ , the boundary layer is stable

= 0, the boundary layer is neutrally stable

> 0, the boundary layer is unstable

In the temporal method,  $\omega_i$  measures the amplification of the disturbances in time and in the spatial method,  $-\alpha_i$  measures the growth rate of the disturbances in the streamwise direction. The boundary layer is stable, neutrally stable or unstable to small disturbances depending on whether the amplification rate  $\omega_i$  or  $-\alpha_i$  is less than , equal to or greater than zero respectively. Most of the linear stability computations

have been performed based on these classical approaches. In this work, this approach is called 1D method.

The next step is to estimate the correction to the eigenvalues that is obtained from the parallel theory due to the small variation of the meanflow in the streamwise and in the spanwise directions. Three methods are available to compute the evolution of small disturbances in a non-parallel flow. One and the oldest method is the multiple scale approach (Saric, Nayfeh [46]). The second is the Parabolized Stability Equations (PSE) approach (Herbert 1979 [53]) and the third method is to solve the full Navier-Stokes equations in a non-parallel flow (Fasel [49], Joslin [51]). In the linear regime, instead of solving the full Navier-Stokes equation, the linearized Navier-Stokes equations are solved [52]. In the multiple scale and in the PSE methods the disturbances are written in the form

$$\Phi(x_1, x_3) = \Phi_o(x_1, x_3) e^{i \int \alpha(x_1) dx_1 + i\beta x_2 - i\omega t} . \tag{1.6}$$

Here  $\omega$  is the real frequency,  $\beta$  is the real spanwise wavenumber,  $\alpha(x_1)$  is the streamwise wavenumber which is a function of  $x_1$  and  $\Phi_o(x_1, x_3)$  is the amplitude function which is a function of both  $x_1$  and  $x_3$ . This form of the representation is mathematically and physically meaningful in a meanflow which varies only in the streamwise  $(x_1)$  and normal  $(x_3)$  direction and is uniform in the spanwise  $(x_2)$  direction. These approaches are used to compute the evolution of the disturbances in two-dimensional Blasius type boundary layers and in quasi-three dimensional, infinite swept wing, boundary layers (El Hady [48], Herbert [33] and Malik [34]).

The objective in this work is to investigate the stability and the evolution of disturbances in fully three-dimensional boundary layers. By the fully three-dimensional boundary layers it is meant boundary layer flows over finite wings, flow over non-axisymmetric geometries like ellipsoids, delta wings and flow over axisymmetric geometries at angles of attack etc. Specifically, in this thesis the stability

of supersonic boundary layer flows over a sharp axi-symmetric cone at an angle of attack (King 1992 [54]) is investigated. In this case, the meanflow varies in all three directions, streamwise, azimuthal and in normal directions. Since the mean flow varies in the azimuthal direction, it is not possible to decompose the disturbances as a sum of Fourier components as is done in the axi-symmetric or in the infinite swept wing flows. The expectation is that since the instability is directly related to the local mean flow conditions, the eigenfunctions will be confined to a region in the azimuthal direction. Hence, the normal mode is written in the form

$$\Phi(x_1, x_2, x_3) = \Phi_o(x_1, x_2, x_3) e^{i \int \alpha(x_1) dx_1 - i\omega t}.$$
(1.7)

The azimuthal variation is included in the amplitude part  $\Phi(x_1, x_2, x_3)$  which now becomes a strong function of  $x_2$  and  $x_3$  and a slowly varying function of  $x_1$ . If the  $x_1$  dependence of  $\Phi_o$  and  $\alpha$  are dropped, one can obtain an eigenvalue problem for  $\alpha$  or  $\omega$  and  $\Phi_o(x_2, x_3)$  which is a function of  $x_2$  and  $x_3$ coordinates. This is called as 2D eigenvalue problem.

Several experiments were performed to understand the stability and transition of supersonic and hypersonic two dimensional and three dimensional boundary layers. The experiments can be divided into two groups. One is transition experiments in which the transition onset is measured at different flow conditions (Potter 1974 [18], Krogmann 1977 [55], Stetson 1981 [9], King 1992 [54]). In these experiments, the unit Reynolds number effects and the effects of the angles of attack on the transition front are investigated.

Since there is no length scale in flows over sharp cones, the transition Reynolds number should not change with the free stream unit Reynolds numbers. However, experiments performed in different wind tunnels at different Reynolds numbers change with the free stream unit Reynolds number. Though transition is influenced by several factors, bluntness, angle of attack, vibration of the model, roughness,

free stream disturbance levels, spectral content of the free stream disturbance, the unit Reynolds number effects are generally attributed to the radiated acoustic field from the boundary layers on the tunnel walls. Main conclusion is that in quiet tunnels at low unit Reynolds numbers the boundary layers on the wall remain laminar and the effect of unit Reynolds number on the transition Reynolds number is minimal. In noisy wind tunnels the boundary layers on the walls become turbulent and the transition Reynolds numbers decrease with the unit Reynolds numbers.

The experiments performed over sharp and blunt cones at small angles of attack show that the transition front moves downstream on the windward ray and moves downstream on the leeward ray.

The second type of experiments are the stability experiments where the stability characteristics of the boundary layers are investigated. Stetson and his coworkers systematically investigated the stability characteristics of hypersonic boundary layers in natural conditions (Stetson et.al., 1983 [10], 1984 [11], 1985 [12], 1986 [13], 1989 [14]). Their results are summarized in a review paper by Stetson and Kimmel(1992) [15]. Experiments were performed on sharp and blunt cones with 7° half angle at a free stream Mach number of 8 at zero and nonzero angles of attack and with adiabatic and cooled surface conditions.

The experiments agree with the theoretical predictions that the transition in hypersonic boundary layers is dominated by the high frequency second mode type disturbances. However, the measured growth rates are much smaller than that is computed from the linear stability theory. It is also observed that the small nose bluntness increases the critical Reynolds number from that for a sharp cone. Flow over a sharp cone at an angle of attack showed that the boundary layer along the windward direction becomes more stable and on the leeward side it becomes more unstable compared to that is obtained at zero angle of attack. Hence transition on the leeward side moves downstream and in the leeward side moves upstream from

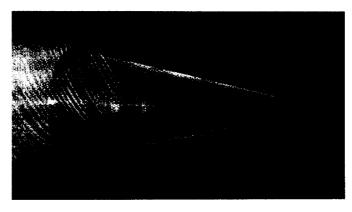
that for a sharp cone. The frequencies of the most amplified disturbances on the windward side are larger than that is obtained for a sharp cone at angle of attack. This is attributed to the finding that the frequency of the most amplified waves in hypersonic boundary layers depends inversely on the boundary layer thickness which is smaller than that is obtained at zero angle of attack, hence the frequency of the most amplified waves are higher. Unit Reynolds number effects are investigated by measuring the spectral content of the free-stream disturbances and the range of the most amplified frequencies for the boundary layer. It is observed that most of the energy in the freestream disturbances are contained in the low frequency disturbances and the spectrum for the high frequency disturbances are very small. But it was concluded that the high frequency disturbances with very small amplitudes are are sufficient to initiate the second mode disturbances. It was also observed that if the frequency of the most amplified wave for the boundary layer is much higher than the frequency limit in the free-stream disturbance spectrum, then the most amplified wave will not be initiated and the transition is dominated by the smaller frequency waves which are excited by the free-stream disturbances. Instantaneous structure and the ensemble-averaged structure of the second mode instability waves in a hypersonic boundary layer was measured by Kimmel et. al. (1997) [22], Poggie(1997) [7] in natural conditions. It is observed that the second mode disturbances travel as wavepackets confined to a small region in the circumferential direction. Recently Poggie et. al. (1998) [6] investigated the stability and transition of a hypersonic three-dimensional boundary layer over an elliptic cone. Transition front appears asymmetric with early transition close to the minor axis and delayed transition close to the major axis which is similar to that is observed in the flow over a sharp cone at an angle of attack.

King (1992) [54] investigated the transition of a three-dimensional boundary layer in NASA Langley's Mach 3.5 quiet tunnel. The experiments were performed

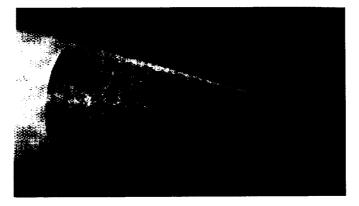
for a 5° half angle sharp cone at various angles of attack. The transition is dominated by crossflow dominated instability and the transition onset point moves downstream near the windward side and moves upstream near the leeward side. This case is chosen to investigate the stability characteristics of a three-dimensional boundary layer using the 2D eigenvalue method.



a) Rotational speed below critical- no instability apparent



b) Rotational speed slightly above critical - spiral streaks are observed



c) Rotational speed far above critical- spiral streaks are observed, then secondary instability superposed on the vortices, then transition

Fig. 1.2 Flow visualization for a spinning cone (Kobayashi et al. 1983)

e de la companya de l

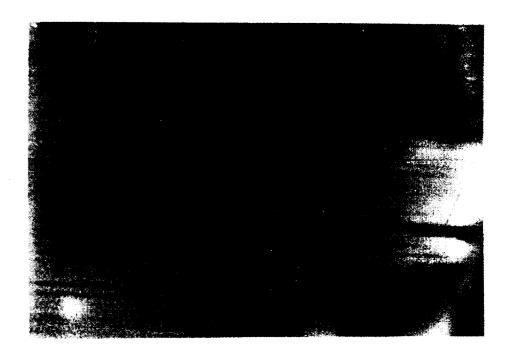


Fig. 1.3 Naphthalene surface patterns illustrating cross-flow vortices (Saric & Yeates 1985). Flow is from left to right.

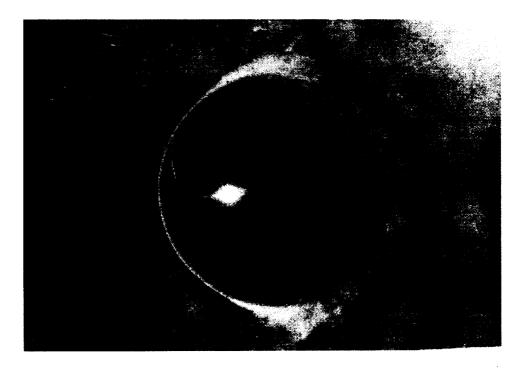


Fig. 1.4 Flow visualization for a rotating sphere: spiral streaks are observed , then the secondary instability superposed on the vortices, then transition (Kohama & Kobayashi 1983b).

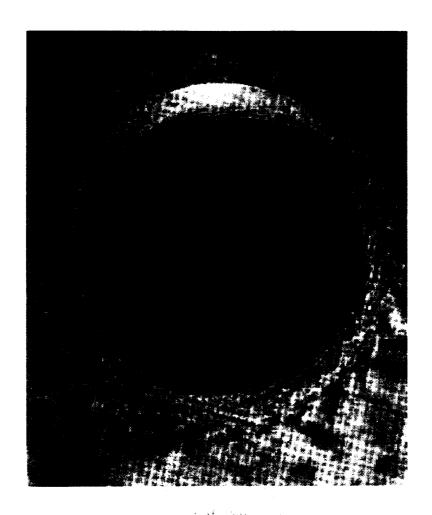


Fig. 1.5 Flow visualization illustrating the spiral vortices on a disk (Kohama 1984a).

#### CHAPTER 2

#### **FORMULATION**

This chapter describes the formulation of the linear stability theory of three-dimensional compressible boundary layer and the numerical procedure that is used to solve these equations for a model case - supersonic flow over a sharp cone at an angle of attack. The first section deals with the derivation of the linear Parabolized Stability Equations in its most generic form i.e, in generalized curvilinear coordinate system. In the second section, the classical one-dimensional stability equations and the two-dimensional stability equations are derived from the general theory as special cases.

As described in the introduction, the stability problem is formulated in two different methods. The first methodology is to make a locally parallel flow assumption i.e, neglect the meanflow variations in the streamwise and azimuthal directions and formulate the problem as a 1D eigenvalue problem. In other words, the solutions to the stability equations are sought in a line normal to the cone surface. In fact, large portion of the literature on stability computations of three-dimensional and two dimensional boundary layers are performed as 1D eigenvalue problems. But the parallel flow assumption will not hold true for flows which are highly three-dimensional and the stability computations and transition prediction will not be correct. Hence in an attempt to construct a near approximate solution to the full Navier-Stokes equation, the variation of the meanflow in the azimuthal direction is incorporated in the second method and formulated as a 2D eigenvalue problem. Thereby normal mode solution is sought in a plane at a streamwise location, rather than in a line as in the former method. In both cases, 1D and 2D eigenvalue approaches, the problem can be formulated as temporal or a spatial stability methods. In the temporal stabil-

ity the wave number in streamwise direction  $\alpha$  is known and the desired eigenvalue is the temporal frequency  $\omega$ , whereas in spatial stability  $\omega$  is fixed and  $\alpha$  is sought.

There are two classes of numerical methods that can be used for the computations of the temporal or spatial eigenvalues from the eigenvalue problems: global and local methods. In the global method a generalized eigenvalue problem is set up and the eigenvalues are obtained using some standard algorithms such as QZ available in the public-domain software library LAPACK. Here, a guess for the eigenvalues is not required. On the other hand, in the local method a guess for the eigenvalue is required and only the eigenvalue that happens to be in the neighborhood of the guessed value is computed using some iterative techniques. These methods will be discussed in detail in the last section of this chapter.

### 2.1 Formulation of the Stability Theory

The growth or decay of infinitesimal perturbations superimposed on a laminar flow is the focus of linear stability theory. The linear stability theory analyzes the characteristics of the instabilities of the mean laminar flow over the surface of interest. Transition prediction is basically composed of two tasks; (1) accurate calculation of the viscous flow field over the the body, (2) calculation of the amplification rate. The stability properties of two-dimensional incompressible and compressible boundary-layers and three-dimensional incompressible and compressible boundary-layers were discussed in the first chapter. In this section, the derivation of the linear stability equation, starting from the compressible three-dimensional Navier-Stokes equations in orthogonal curvilinear coordinate system is presented. Normal mode method is chosen in the formulation. Since the final expression for the linear stability equations in the generalized curvilinear coordinate system contain numerous terms only linearized continuity equation will be given.

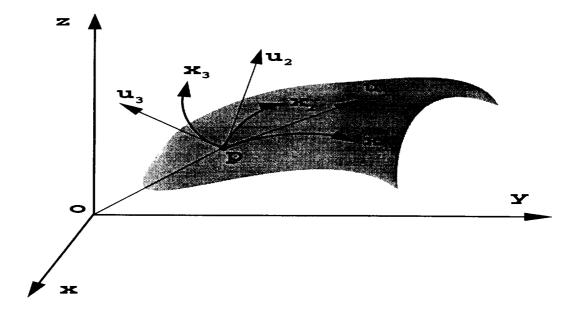


Fig. 2.1 Orthogonal curvilinear coordinate system

### 2.1.1 Governing Equations

The derivation of the stability equations starts from the Navier-Stokes equations for three-dimensional compressible flow for an ideal viscous gas in orthogonal curvilinear coordinate system. The governing equations are the continuity equation, the momentum equations in the streamwise, azimuthal and normal directions and energy equation. In addition, perfect gas equation of state is used to 'close' the system of fluid dynamic equations. A body-oriented coordinate system is used as shown in figure 2.1, with  $x_1$  taken along the streamwise direction,  $x_2$  along the azimuthal direction and  $x_3$  normal to the surface. The Navier-Stokes equations in the vector form are:

#### Continuity equation

$$\frac{\partial \rho}{\partial t} + \nabla \cdot \rho \mathbf{V} = 0 \quad . \tag{2.1}$$

#### Momentum equations

$$\rho\left(\frac{\partial \mathbf{V}}{\partial t} + \mathbf{V} \cdot \nabla \mathbf{V}\right) = \rho \mathbf{f} + \nabla \cdot \mathbf{\Pi}_{ij} \qquad ; \quad i, j = 1, 2, 3$$
 (2.2)

#### Energy equation

$$\rho C_v \left( \frac{\partial T}{\partial t} + \mathbf{V} \cdot \nabla T \right) = \nabla \cdot (\kappa \nabla T) + \Phi \quad (2.3)$$

#### Equation of state

$$p = \rho RT \quad . \tag{2.4}$$

The first term on the right hand side of the momentum equations, Eq. 2.2, is the body force per unit volume.  $\Pi_{ij}$  represents the component of the stress tensor, which consists of normal stresses and shearing stresses.  $\Phi$  in the energy equation, Eq. 2.8, is the dissipation function.

The expanded form of these expressions as given by Anderson et.al. [32] is adopted here.

#### Continuity equation

$$\frac{\partial \rho}{\partial t} + \frac{1}{h_1 h_2 h_3} \left[ \frac{\partial}{\partial x_1} (h_2 h_3 \rho u_1) + \frac{\partial}{\partial x_2} (h_3 h_1 \rho u_2) + \frac{\partial}{\partial x_3} (h_1 h_2 \rho u_3) \right] = 0$$
 (2.5)

#### $x_1$ momentum

$$\rho \frac{\partial u_1}{\partial t} \ + \ \frac{\rho u_1}{h_1} \frac{\partial u_1}{\partial x_1} + \frac{\rho u_2}{h_2} \frac{\partial u_1}{\partial x_2} + \frac{\rho u_3}{h_3} \frac{\partial u_1}{\partial x_3} + \frac{\rho u_1 u_2}{h_1 h_2} \frac{\partial h_1}{\partial x_2} + \frac{\rho u_1 u_3}{h_1 h_3} \frac{\partial h_1}{\partial x_3}$$

$$-\frac{\rho u_2^2}{h_1 h_2} \frac{\partial h_2}{\partial x_1} - \frac{\rho u_3^2}{h_1 h_3} \frac{\partial h_3}{\partial x_1}$$

$$= \frac{1}{h_1 h_2 h_3} \left[ \frac{\partial}{\partial x_1} (h_2 h_3 \Pi_{x_1 x_1}) + \frac{\partial}{\partial x_2} (h_1 h_3 \Pi_{x_1 x_2}) + \frac{\partial}{\partial x_3} (h_1 h_2 \Pi_{x_1 x_3}) \right]$$

$$\begin{split} +\Pi_{x_1x_2}\frac{1}{h_1h_2}\frac{\partial h_1}{\partial x_2} + \Pi_{x_1x_3}\frac{1}{h_1h_3}\frac{\partial h_1}{\partial x_3} - \Pi_{x_2x_2}\frac{1}{h_1h_2}\frac{\partial h_2}{\partial x_1} \\ -\Pi_{x_3x_3}\frac{1}{h_1h_3}\frac{\partial h_3}{\partial x_1} \ \cdot \end{split}$$

 $x_2$  momentum

$$\rho \frac{\partial u_{2}}{\partial t} + \frac{\rho u_{1}}{h_{1}} \frac{\partial u_{2}}{\partial x_{1}} + \frac{\rho u_{2}}{h_{2}} \frac{\partial u_{2}}{\partial x_{2}} + \frac{\rho u_{3}}{h_{3}} \frac{\partial u_{2}}{\partial x_{3}} - \frac{\rho u_{1}^{2}}{h_{1} h_{2}} \frac{\partial h_{1}}{\partial x_{2}} + \frac{\rho u_{1} u_{2}}{h_{1} h_{2}} \frac{\partial h_{1}}{\partial x_{2}}$$

$$+ \frac{\rho u_{2} u_{3}}{h_{1} h_{3}} \frac{\partial h_{2}}{\partial x_{3}} - \frac{\rho u_{3}^{2}}{h_{2} h_{3}} \frac{\partial h_{3}}{\partial x_{2}}$$

$$= \frac{1}{h_{1} h_{2} h_{3}} \left[ \frac{\partial}{\partial x_{1}} (h_{2} h_{3} \Pi_{x_{1} x_{2}}) + \frac{\partial}{\partial x_{2}} (h_{1} h_{3} \Pi_{x_{2} x_{2}}) + \frac{\partial}{\partial x_{3}} (h_{1} h_{2} \Pi_{x_{2} x_{3}}) \right]$$

$$+ \Pi_{x_{2} x_{3}} \frac{1}{h_{2} h_{3}} \frac{\partial h_{2}}{\partial x_{3}} \Pi_{x_{1} x_{2}} \frac{1}{h_{1} h_{2}} \frac{\partial h_{2}}{\partial x_{1}} - \Pi_{x_{3} x_{3}} \frac{1}{h_{2} h_{3}} \frac{\partial h_{3}}{\partial x_{2}}$$

$$- \Pi_{x_{1} x_{1}} \frac{1}{h_{1} h_{2}} \frac{\partial h_{1}}{\partial x_{2}} . \tag{2.6}$$

 $x_3$  momentum

$$\rho \frac{\partial u_{3}}{\partial t} + \frac{\rho u_{1}}{h_{1}} \frac{\partial u_{3}}{\partial x_{1}} + \frac{\rho u_{2}}{h_{2}} \frac{\partial u_{3}}{\partial x_{2}} + \frac{\rho u_{3}}{h_{3}} \frac{\partial u_{3}}{\partial x_{3}} - \frac{\rho u_{1}^{2}}{h_{1}h_{3}} \frac{\partial h_{1}}{\partial x_{3}} - \frac{\rho u_{2}^{2}}{h_{2}h_{3}} \frac{\partial h_{2}}{\partial x_{3}}$$

$$+ \frac{\rho u_{1}u_{3}}{h_{1}h_{3}} \frac{\partial h_{3}}{\partial x_{1}} + \frac{\rho u_{2}u_{3}}{h_{2}h_{3}} \frac{\partial h_{3}}{\partial x_{2}}$$

$$= \frac{1}{h_{1}h_{2}h_{3}} \left[ \frac{\partial}{\partial x_{1}} (h_{2}h_{3}\Pi_{x_{1}x_{3}}) + \frac{\partial}{\partial x_{2}} (h_{1}h_{3}\Pi_{x_{2}x_{3}}) + \frac{\partial}{\partial x_{3}} (h_{1}h_{2}\Pi_{x_{3}x_{3}}) \right]$$

$$+ \Pi_{x_{1}x_{3}} \frac{1}{h_{1}h_{3}} \frac{\partial h_{3}}{\partial x_{1}} + \Pi_{x_{2}x_{3}} \frac{1}{h_{2}h_{3}} \frac{\partial h_{3}}{\partial x_{2}} - \Pi_{x_{1}x_{1}} \frac{1}{h_{1}h_{3}} \frac{\partial h_{1}}{\partial x_{3}}$$

$$- \Pi_{x_{2}x_{2}} \frac{1}{h_{2}h_{2}} \frac{\partial h_{2}}{\partial x_{2}} . \qquad (2.7)$$

Energy equation

$$\rho C_v \left[ \frac{\partial T}{\partial t} + \rho \frac{\partial T}{\partial t} + \frac{u_1}{h_1} \frac{\partial T}{\partial x_1} + \frac{u_2}{h_2} \frac{\partial T}{\partial x_2} + \frac{u_3}{h_3} \frac{\partial T}{\partial x_3} \right]$$

$$+\frac{p}{h_1 h_2 h_3} \left[ \frac{\partial}{\partial x_1} (h_2 h_3 u_1) + \frac{\partial}{\partial x_2} (h_1 h_3 u_2) + \frac{\partial}{\partial x_3} (h_1 h_2 u_3) \right]$$

$$= \frac{1}{h_1 h_2 h_3} \left[ \frac{\partial}{\partial x_1} (k h_2 h_3 \Pi_{x_1 x_3}) + \frac{\partial}{\partial x_2} (k h_1 h_3 \Pi_{x_2 x_3}) \right]$$

$$+ \frac{\partial}{\partial x_3} (k h_1 h_2 \Pi_{x_3 x_3}) + \Phi . \tag{2.8}$$

Here  $u_1$ ,  $u_2$  and  $u_3$  are velocities along the streamwise $(x_1)$ , azimuthal $(x_2)$  and normal $(x_3)$  directions respectively and  $\rho$  is the density, p is the pressure,  $\mu$  is the coefficient of viscosity and  $\kappa$  is the coefficient of thermal conductivity.  $h_1$ ,  $h_2$  and  $h_3$  are the metric coefficients along the coordinates  $x_1$ ,  $x_2$  and  $x_3$  respectively. In the generalized curvilinear coordinates, the dissipation function becomes

$$\Phi = \mu \left[ 2(e_{11}^2 + e_{22}^2 + e_{33}^2) + e_{23}^2 + e_{13}^2 + e_{12}^2 - \frac{2}{3}(e_{11} + e_{22} + e_{33})^2 \right] , \qquad (2.9)$$

where the expressions for the strains are

$$e_{11} = \frac{1}{h_1} \frac{\partial u_1}{\partial x_1} + \frac{u_3}{h_1 h_3} \frac{\partial h_1}{\partial x_3} + \frac{u_2}{h_1 h_2} \frac{\partial h_1}{\partial x_2} ,$$

$$e_{22} = \frac{1}{h_2} \frac{\partial u_2}{\partial x_2} + \frac{u_3}{h_2 h_3} \frac{\partial h_2}{\partial x_3} + \frac{u_1}{h_1 h_2} \frac{\partial h_2}{\partial x_1} ,$$

$$e_{33} = \frac{1}{h_3} \frac{\partial u_3}{\partial x_3} + \frac{u_1}{h_1 h_3} \frac{\partial h_3}{\partial x_1} + \frac{u_2}{h_2 h_3} \frac{\partial h_3}{\partial x_2} ,$$

$$e_{23} = \frac{1}{h_2} \frac{\partial u_3}{\partial x_2} + \frac{1}{h_3} \frac{\partial u_2}{\partial x_3} - \frac{u_2}{h_2 h_3} \frac{\partial h_2}{\partial x_3} - \frac{u_3}{h_2 h_3} \frac{\partial h_3}{\partial x_2} ,$$

$$e_{13} = \frac{1}{h_3} \frac{\partial u_3}{\partial x_1} + \frac{1}{h_1} \frac{\partial u_3}{\partial x_1} - \frac{u_1}{h_1 h_3} \frac{\partial h_1}{\partial x_3} - \frac{u_3}{h_1 h_3} \frac{\partial h_3}{\partial x_1} ,$$

$$(2.10)$$

$$e_{12} = \frac{1}{h_1} \frac{\partial u_2}{\partial x_1} + \frac{1}{h_2} \frac{\partial u_1}{\partial x_2} - \frac{u_2}{h_1 h_2} \frac{\partial h_2}{\partial x_1} - \frac{u_1}{h_1 h_2} \frac{\partial h_1}{\partial x_2} .$$

The component of stress tensors appearing in the momentum equations Eq. 2.6, Eq. 2.6 and Eq. 2.7 can be expressed as

$$\begin{split} \Pi_{x_1x_1} &= -p + \frac{2}{3}\mu \left[ \frac{2}{h_1} \frac{\partial u_1}{\partial x_1} + \frac{2u_2}{h_1h_2} \frac{\partial h_1}{\partial x_2} + \frac{2u_3}{h_1h_3} \frac{\partial h_1}{\partial x_3} - \frac{1}{h_2} \frac{\partial u_2}{\partial x_2} - \frac{u_3}{h_2h_3} \frac{\partial h_2}{\partial x_3} \right. \\ & \left. - \frac{u_1}{h_1h_2} \frac{\partial h_2}{\partial x_1} - \frac{1}{h_3} \frac{\partial u_3}{\partial x_3} - \frac{u_1}{h_1h_3} \frac{\partial h_3}{\partial x_1} - \frac{u_2}{h_2h_3} \frac{\partial h_3}{\partial x_1} \right] \,, \\ \Pi_{x_1x_2} &= \mu \left[ \frac{1}{h_1} \frac{\partial u_2}{\partial x_1} - \frac{u_2}{h_1h_2} \frac{\partial h_2}{\partial x_1} + \frac{1}{h_2} \frac{\partial u_1}{\partial x_2} - \frac{u_1}{h_1h_2} \frac{\partial h_1}{\partial x_2} \right] \,, \\ \Pi_{x_1x_3} &= \mu \left[ \frac{1}{h_3} \frac{\partial u_1}{\partial x_3} - \frac{u_1}{h_1h_3} \frac{\partial h_1}{\partial x_3} + \frac{1}{h_1} \frac{\partial u_3}{\partial x_1} - \frac{u_3}{h_1h_3} \frac{\partial h_3}{\partial x_1} \right] \,, \\ \Pi_{x_2x_2} &= -p + \frac{2}{3}\mu \left[ \frac{2}{h_2} \frac{\partial u_2}{\partial x_2} + \frac{2u_3}{h_2h_3} \frac{\partial h_2}{\partial x_3} + \frac{2u_1}{h_1h_2} \frac{\partial h_2}{\partial x_1} - \frac{1}{h_1} \frac{\partial u_1}{\partial x_1} - \frac{u_2}{h_1h_2} \frac{\partial h_1}{\partial x_2} \right. \\ & \left. - \frac{u_3}{h_1h_3} \frac{\partial h_1}{\partial x_3} - \frac{1}{h_3} \frac{\partial u_3}{\partial x_3} - \frac{u_1}{h_2h_3} \frac{\partial h_2}{\partial x_1} - \frac{u_2}{h_2h_3} \frac{\partial h_3}{\partial x_2} \right] \,, \end{aligned} \quad (2.11$$

$$\Pi_{x_2x_3} &= \frac{\mu}{Re} \left[ \frac{1}{h_2} \frac{\partial u_3}{\partial x_2} - \frac{u_3}{h_2h_3} \frac{\partial h_3}{\partial x_2} + \frac{1}{h_3} \frac{\partial u_2}{\partial x_3} - \frac{u_2}{h_2h_3} \frac{\partial h_2}{\partial x_2} - \frac{u_2}{h_2h_3} \frac{\partial h_2}{\partial x_3} \right] \,, \\ \Pi_{x_3x_3} &= -p + \frac{2}{3}\mu \left[ \frac{2}{h_3} \frac{\partial u_3}{\partial x_3} + \frac{2u_1}{h_1h_3} \frac{\partial h_3}{\partial x_1} + \frac{2u_2}{h_2h_3} \frac{\partial h_3}{\partial x_2} - \frac{1}{h_1} \frac{\partial u_1}{\partial x_1} - \frac{u_2}{h_1h_2} \frac{\partial h_1}{\partial x_2} \right. \\ & \left. - \frac{u_3}{h_1h_3} \frac{\partial h_1}{\partial x_3} - \frac{1}{h_2h_3} \frac{\partial u_2}{\partial x_2} - \frac{u_3}{h_2h_3} \frac{\partial h_2}{\partial x_2} - \frac{1}{h_1} \frac{\partial u_1}{\partial x_1} - \frac{u_2}{h_1h_2} \frac{\partial h_1}{\partial x_2} \right. \\ & \left. - \frac{u_3}{h_1h_3} \frac{\partial h_1}{\partial x_3} - \frac{1}{h_2} \frac{\partial u_2}{\partial x_2} - \frac{u_3}{h_2h_3} \frac{\partial h_2}{\partial x_3} - \frac{u_1}{h_1h_2} \frac{\partial h_2}{\partial x_3} \right] \,. \end{aligned}$$

### 2.1.2 Linearization of the equations

The principle of classical stability theory evolves around the concept of determining whether a small disturbance introduced into a laminar boundary layer will amplify or decay. If the disturbance decays, the boundary layer is stable and if the disturbance grows it is called linearly unstable. In stability theory, the first step in the methodology of analyzing the evolution of small disturbances is to assume the 'total flow' as composed of mean quantities and small disturbance quantities.

$$Q(x_1, x_2, x_3, t) = \overline{Q}(x_1, x_2, x_3, t) + q(x_1, x_2, x_3, t),$$
(2.12)

and in components form

$$U_{1} = \overline{U_{1}} + u_{1} ,$$

$$U_{2} = \overline{U_{2}} + u_{2} ,$$

$$U_{3} = \overline{U_{3}} + u_{3} ,$$

$$p = \overline{p} + \pi ,$$

$$T = \overline{T} + \theta ,$$

$$\rho = \overline{\rho} + \rho ,$$
(2.13)

where Q is the total quantity,  $\overline{Q}$  is the mean quantity and q is the disturbance quantity.

The stability equations are derived as follows: first, the expressions for total flow quantities, Eqs. 2.13, are substituted into the Navier-Stokes equations Eqs. (2.6 - 2.8). Since it is assumed that the mean-flow terms satisfy the steady Navier-Stokes equations, the mean terms can be subtracted out, resulting in terms consisting of products of mean-flow and disturbance quantities ( $\overline{Q}q$ ) and the products of disturbance terms (qq). Secondly, in the linear theory, since the nonlinear terms, the products of infinitesimal disturbances, are of lower order than rest of the terms, they are neglected. Substituting the normal mode form for the disturbances, Linear Stability Equations (LSE) are obtained.

### 2.1.3 Nondimensionalization of the Equations

As is customary and convenient, the LSE are written in nondimensional form using some characteristic quantities. The characteristic velocity is  $U_o$ , which is taken to be the value of streamwise velocity at the edge of the boundary-layer in 1D formulation and the boundary layer edge velocity at a reference station  $x_2 = 90^\circ$  in the case of 2D formulation; the characteristic length is L, which is given by the expression

$$L = \sqrt{\frac{\nu^{\star}_{e} x_{1}^{\star}}{U^{\star}_{o}}}, \qquad (2.14)$$

The thermodynamic quantities are nondimensionalized by their corresponding boundaryedge values i.e, the characteristic density, temperature and molecular viscosity are  $\rho_e$ ,  $T_e$  and  $\mu_e$  respectively, the characteristic pressure is  $\rho_e U_o^2$  and the characteristic time is  $\frac{L}{U_o}$ .

The non-dimensional quantities are

$$u_{1} = \frac{u_{1}^{*}}{U_{o}^{*}}, \qquad u_{2} = \frac{u_{2}^{*}}{U_{o}^{*}}, \qquad u_{3} = \frac{u_{3}^{*}}{U_{o}^{*}},$$

$$\pi = \frac{\pi^{*}}{\rho_{e}^{*}U_{o}^{*}}, \qquad \theta = \frac{\theta^{*}}{T_{e}^{*}}, \qquad \rho = \frac{\rho^{*}}{\rho_{e}^{*}},$$

$$\overline{U}_{1} = \frac{\overline{U}_{1}^{*}}{U_{o}^{*}}, \qquad \overline{U}_{2} = \frac{\overline{U}_{2}^{*}}{U_{o}^{*}}, \qquad \overline{U}_{3} = \frac{\overline{U}_{3}^{*}}{U_{o}^{*}},$$

$$\overline{T} = \frac{\overline{T}^{*}}{T_{e}^{*}}, \qquad \overline{\rho} = \frac{\overline{\rho}^{*}}{\rho_{e}^{*}}, \qquad \overline{\mu} = \frac{\overline{\mu}^{*}}{\mu_{e}^{*}},$$

$$x_{1} = \frac{x_{1}^{*}}{L}, \qquad x_{2} = \frac{x_{2}^{*}}{L}, \qquad x_{3} = \frac{x_{3}^{*}}{L},$$

$$t = \frac{t^{*}}{L}U_{o}^{*}. \qquad (2.15)$$

Here the superscript \* denotes the dimensional quantities. Some of the non-dimensional parameters which appear in the equations are defined below.

Free-stream Mach number

$$M = \frac{U_o}{\sqrt{\gamma R T_e}}.$$
 (2.16)

Prandtl number

$$Pr = C_p \frac{\mu}{\kappa} \,. \tag{2.17}$$

Here Prandtl number is assumed to be constant and taken to be 0.7 all through the computations. The constants of specific heat at constant pressure and volume are related by

$$C_p = \gamma C_v$$
 (2.18)

The values of ratio of specific heats  $\gamma$  and gas constant R are taken to be

$$\gamma = 1.4,\tag{2.19}$$

$$R = 287m^2/s^{2} K \cdot (2.20)$$

# 2.1.4 Reduction of the Number of Variables

The Linear Stability Equations contain perturbation terms,  $u_1, u_2, u_3, \pi, \theta, \rho, \mu$  and  $\kappa$ , which are the unknown variables. Since some of these variables are related to other variables by simple equations such as Eq. 2.4, Eq. 2.17 one can easily eliminate them from the stability equations. This will result in substantial reduction in computational effort and storage requirements.

The coefficient of viscosity  $\mu$  is assumed to be a function of temperature only and Sutherland's viscosity law is used in the computations.

$$\frac{\mu}{\mu_e} = \left(\frac{T}{T_e}\right)^{3/2} \left(\frac{1+C}{T/T_e+C}\right) ,$$
 (2.21)

where

$$C = 110.4K/T_e , (2.22)$$

and  $T_e$  is the temperature at the edge of the boundary-layer. Hence, the total viscosity term which is the sum of mean and perturbation quantities, can be written

as

$$\overline{\mu} + \mu = \mu(\overline{T} + \theta),$$

and using Taylor series expansion for small temperature fluctuation  $\theta$ , one can write

$$\mu(T+\theta) = \mu(\overline{T}) + \frac{\partial \mu(\overline{T})}{\partial \overline{T}}\theta + \cdots,$$

$$= \overline{\mu} + \frac{\partial \overline{\mu}}{\partial \overline{\overline{T}}} \theta + \cdots \qquad (2.23)$$

Hence the disturbance  $\mu$  can be written as

$$\mu = \frac{\partial \overline{\mu}}{\partial \overline{T}} \theta \ . \tag{2.24}$$

using equation Eq. 2.24 the derivatives of  $\mu$  become

$$\frac{\partial \mu}{\partial x_i} = \frac{\partial^2 \overline{\mu}}{\partial \overline{T}^2} \frac{\partial \overline{T}}{\partial x_i} \theta + \frac{\partial \overline{\mu}}{\partial \overline{T}} \frac{\partial \theta}{\partial x_i}.$$

For reasons that would become clear later in this chapter it is chosen to express  $\pi$  in terms of density fluctuation  $\rho$  and temperature fluctuation  $\theta$ , rather than eliminating  $\rho$  from LSE. The equation of state in non-dimensional form is

$$p\gamma M^2 = \rho T , \qquad (2.25)$$

The pressure fluctuation is related to density and temperature fluctuations by the expression

$$\pi \gamma M^2 = \rho \overline{T} + \overline{\rho} \theta , \qquad (2.26)$$

or,

$$\pi = \left(\frac{\overline{T}}{\gamma M^2}\right)\rho + \left(\frac{\overline{\rho}}{\gamma M^2}\right)\theta \quad . \tag{2.27}$$

And the derivatives of  $\pi$  with respect to the coordinates are

$$\frac{\partial \pi}{\partial x_i} = \left(\frac{\overline{T}}{\gamma M^2}\right) \frac{\partial \rho}{\partial x_i} + \left(\frac{\overline{\rho}}{\gamma M^2}\right) \frac{\partial \theta}{\partial x_i} + \frac{1}{\gamma M^2} \left(\frac{\partial \overline{T}}{\partial x_i}\right) \rho + \frac{1}{\gamma M^2} \left(\frac{\partial \overline{\rho}}{\partial x_i}\right) \theta . \tag{2.28}$$

Hence, the dependent variables in the stability equations are  $\hat{\mathbf{q}} = \{u_1, u_2, u_3, \rho, \theta\}^T$ .

## 2.1.5 Introduction of Harmonic Disturbances

As discussed previously, the stability of a three-dimensional boundary layer is investigated by seeking a solution of the form:

$$\mathbf{q}(x_1, x_2, x_3, t) = \hat{\mathbf{q}}(x_1, x_2, x_3)e^{i\int \alpha dx_1 - i\omega t} + c \cdot c \quad (2.29)$$

Here  $\hat{\mathbf{q}} = \{\hat{u_1}, \hat{u_2}, \hat{u_3}, \hat{\rho}, \hat{\theta}\}^T$ , is a complex amplitude function of the disturbance variables;  $\alpha(x_1)$  is the wavenumber in the streamwise direction and  $\omega$  is the temporal frequency of the disturbances.

The first and second derivatives of  $\mathbf{q}(x_1, x_2, x_3, t)$  with respect to the streamwise coordinate  $x_1$  are

$$\frac{\partial \mathbf{q}}{\partial x_1} = \left\{ i\alpha(x_1)\hat{\mathbf{q}}(x_1, x_2, x_3) + \frac{\partial \hat{\mathbf{q}}}{\partial x_1} \right\} e^{i\int \alpha dx_1 - i\omega t} . \tag{2.30}$$

$$\frac{\partial^2 \mathbf{q}}{\partial x_1^2} = \left\{ -\alpha^2(x_1) \hat{\mathbf{q}}(x_1, x_2, x_3) + i \frac{d\alpha}{\partial x_1} \hat{\mathbf{q}}(x_1, x_2, x_3) + 2i\alpha \frac{\partial \mathbf{q}}{\partial x_1} + \frac{\partial^2 \hat{\mathbf{q}}}{\partial x_1^2} \right\} e^{i \int \alpha(x_1) dx_1 - i\omega t} .$$
(2.31)

Since the variation of the amplitude part of the disturbance  $\mathbf{q}$  in the streamwise direction is very small, the term  $\frac{\partial^2 \hat{\mathbf{q}}}{\partial x_1^2}$  is neglected and the equation Eq. 2.31 becomes

$$\frac{\partial^2 \mathbf{q}}{\partial x_1^2} \approx \left\{ -\alpha^2(x_1) \hat{\mathbf{q}}(x_1, x_2, x_3) + i \frac{d\alpha}{\partial x_1} \hat{\mathbf{q}}(x_1, x_2, x_3) + 2i\alpha \frac{\partial \mathbf{q}}{\partial x_1} \right\} e^{i \int \alpha(x_1) dx_1 - i\omega t} . \tag{2.32}$$

By substituting these expressions into the linear stability equations Eq. 2.6 - 2.8 one can obtain a set of partial differential equations for  $\hat{\mathbf{q}}$ . These sets of equations incorporate the effect of meanflow variation in streamwise direction and approximate the full Navier-Stokes equations. The concept was first introduced by Herbert [33] and the resulting equations are termed Parabolized Stability Equations(PSE).

The PSE for compressible flow in generalized coordinates contain number of terms, and hence, in order to save space, only the linearized continuity equation in non-dimensional form is given here.

$$-i\omega\rho + \frac{1}{h_1h_3}\frac{\partial h_3}{\partial x_1}\rho\overline{U_1} + \frac{1}{h_1h_2}\frac{\partial h_1}{\partial x_2}\rho\overline{U_1} + \frac{1}{h_1}\frac{\partial\overline{U_1}}{\partial x_1}\rho + \frac{\overline{U_1}}{h_1}\left(i\alpha\rho + \frac{\partial\rho}{\partial x_1}\right)$$

$$+ \frac{1}{h_1h_2}\frac{\partial h_1}{\partial x_2}\rho\overline{U_2} + \frac{1}{h_2h_3}\frac{\partial h_3}{\partial x_2}\rho\overline{U_2} + \frac{1}{h_2}\frac{\partial\overline{U_2}}{\partial x_2}\rho + \frac{\overline{U_2}}{h_2}\frac{\partial\rho}{\partial x_2}$$

$$+ \frac{1}{h_2h_3}\frac{\partial h_2}{\partial x_3}\rho\overline{U_3} + \frac{1}{h_1h_3}\frac{\partial h_1}{\partial x_3}\rho\overline{U_3} + \frac{1}{h_3}\frac{\partial\overline{U_3}}{\partial x_3}\rho + \frac{\overline{U_3}}{h_3}\frac{\partial\rho}{\partial x_3}$$

$$+ \frac{1}{h_1h_3}\frac{\partial h_3}{\partial x_1}\overline{\rho}u_1 + \frac{1}{h_1h_2}\frac{\partial h_2}{\partial x_1}\overline{\rho}u_1 + \frac{1}{h_1}\frac{\partial\overline{\rho}}{\partial x_1}u_1 + \frac{\overline{\rho}}{h_1}(i\alpha u_1 + \frac{\partial u_1}{\partial x_1}) \qquad (2.33)$$

$$+ \frac{1}{h_1h_2}\frac{\partial h_1}{\partial x_2}\overline{\rho}u_2 + \frac{1}{h_2h_3}\frac{\partial h_3}{\partial x_2}\overline{\rho}u_2 + \frac{1}{h_2}\frac{\partial\overline{\rho}}{\partial x_2}u_2 + \frac{\overline{\rho}}{h_2}\frac{\partial u_2}{\partial x_2}$$

$$+ \frac{1}{h_2h_3}\frac{\partial h_2}{\partial x_3}\overline{\rho}u_3 + \frac{1}{h_1h_3}\frac{\partial h_1}{\partial x_3}\overline{\rho}u_3 + \frac{1}{h_3}\frac{\partial\overline{\rho}}{\partial x_3}u_3 + \frac{\overline{\rho}}{h_3}\frac{\partial u_3}{\partial x_3}$$

$$= 0.$$

The sets of linear PSE equations for  $\hat{\mathbf{q}}$  can be written in matrix form as

$$A_{2}\frac{\partial^{2}\hat{\mathbf{q}}}{\partial x_{2}^{2}} + A_{3}\frac{\partial^{2}\hat{\mathbf{q}}}{\partial x_{2}^{2}} + A_{12}\frac{\partial^{2}\hat{\mathbf{q}}}{\partial x_{1}\partial x_{2}} + A_{13}\frac{\partial^{2}\hat{\mathbf{q}}}{\partial x_{1}\partial x_{3}} + A_{23}\frac{\partial^{2}\hat{\mathbf{q}}}{\partial x_{2}\partial x_{3}}$$

$$+ B_1 \frac{\partial \hat{\mathbf{q}}}{\partial x_1} + B_2 \frac{\partial \hat{\mathbf{q}}}{\partial x_2} + B_3 \frac{\partial \hat{\mathbf{q}}}{\partial x_3} + C \hat{\mathbf{q}} = 0 \quad (2.34)$$

Here,  $A_2$   $A_3$ ,  $A_{12}$ ,  $A_{13}$ ,  $A_{23}$ ,  $B_1$ ,  $B_2$ ,  $B_3$  and C are (5x5) complex matrices which are functions of mean-flow quantities and their derivatives,  $\alpha$ ,  $\omega$  and the metrices  $h_1$ ,  $h_2$ ,  $h_3$  and their derivatives.

## 2.1.6 Boundary Conditions

At the solid wall, no-slip conditions apply to the disturbance velocities. The temperature perturbations are assumed to vanish at the solid boundary. This is a reasonable assumption since for almost any frequency of the gas, the temperature fluctuation will not penetrate into the solid boundary due to the thermal inertia of the solid body i.e, the wall can only remain at its mean temperature.

$$u_1 = u_2 = u_3 = \theta = 0;$$
 at  $x_3 = 0$  (2.35)

The boundary conditions in the far field are that disturbances decay to zero.

$$u_1, u_2, u_3, \theta \to 0;$$
 as  $x_3 \to \infty$ . (2.36)

The numerical procedure which is used in the computations need one more boundary condition to be specified for the density perturbation. Since the density does not vanish at the wall and the PSE equations are valid both at the solid boundary and at infinity, the linearized continuity equation or the normal momentum equation can be used as the fifth boundary condition at the wall and at the farfield.

## 2.1.7 Linear Stability Equations

#### 2D Problem

If the  $x_1$  derivative terms in the Parabolized Stability Equations are dropped. one can obtain 2D linear stability equations which are systems of partial differential equations in  $x_2$  and  $x_3$ .

$$A_{2}\frac{\partial^{2}\hat{\mathbf{q}}}{\partial x_{2}^{2}} + A_{3}\frac{\partial^{2}\hat{\mathbf{q}}}{\partial x_{3}^{2}} + A_{23}\frac{\partial^{2}\hat{\mathbf{q}}}{\partial x_{2}\partial x_{3}} + B_{2}\frac{\partial\hat{\mathbf{q}}}{\partial x_{2}} + B_{3}\frac{\partial\hat{\mathbf{q}}}{\partial x_{3}} + C\hat{\mathbf{q}} = 0 \quad (2.37)$$

This corresponds to applying classical parallel stability theory in the  $x_1$  direction and seeking normal mode solution of the form

$$\mathbf{q}(x_1, x_2, x_3, t) = \hat{\mathbf{q}}(x_2, x_3)e^{i\alpha(x_1)x_1 - i\omega t} + c \cdot c \quad (2.38)$$

Here  $\alpha$  is the streamwise wavenumber,  $\omega$  is the temporal frequency. In this work, the temporal stability computations are performed where

$$\alpha = \alpha_r$$
, real prescribed, (2.39)

$$\omega = \omega_r + i\omega_i \, \cdot \tag{2.40}$$

 $\omega$  is computed from the dispersion relation

$$F(\alpha, \omega) = 0 {(2.41)}$$

### 1D Problem

In this method of formulation the variations of meanflow in the streamwise direction and azimuthal directions are neglected and the disturbance quantities are assumed to be periodic in the azimuthal direction. This is equivalent to applying classical stability theory in  $x_1$  and  $x_3$  directions and to seeking normal mode solution of the form

$$\mathbf{q}(x_1, x_2, x_3, t) = \hat{\mathbf{q}}(x_3)e^{i\alpha x_1 + imx_2 - i\omega t} + c \cdot c \quad (2.42)$$

Applying the chain rule for the normal derivatives, one obtains

$$\frac{d\hat{\mathbf{q}}(x_3)}{dx_3} = \left(\frac{d\eta}{dx_3}\right)\frac{d\hat{\mathbf{q}}}{d\eta},$$

$$\frac{d^2\hat{\mathbf{q}}(x_3)}{dx_3^2} = \left(\frac{d\eta}{dx_3}\right)^2 \frac{d^2\hat{\mathbf{q}}}{d\eta^2} + \left(\frac{d^2\eta}{dx_3^2}\right) \frac{d\hat{\mathbf{q}}}{d\eta} \,. \tag{2.49}$$

With these transformations the stability equations in the new coordinate  $\eta$  becomes

$$\mathbf{A_3} \left(\frac{d\eta}{dx_3}\right)^2 \frac{d^2 \hat{\mathbf{q}}}{d\eta^2} + \left[im\mathbf{A_{23}} \left(\frac{d\eta}{dx_3}\right) + \mathbf{B_3}\right] \frac{d\hat{\mathbf{q}}}{d\eta}$$

$$+ \left[-m^2\mathbf{A_2} \left(\frac{d^2\eta}{dx_3^2}\right) + im\mathbf{B_2} + \mathbf{C}\right] \hat{\mathbf{q}} = 0 \quad (2.50)$$

The system of equations are discrescretized using fourth-order central finite difference scheme. At the solid boundary second-order forward differencing and at the outer boundary and second-order backward differencing are used. The second-order accurate forward difference formula at j=1

$$\frac{\partial \phi}{\partial \eta} = \frac{-3\phi_j + 4\phi_{j+1} - \phi_{j+2}}{2\Delta \eta} , \qquad (2.51)$$

$$\frac{\partial^2 \phi}{\partial \eta^2} = \frac{\phi_j - 2\phi_{j+1} + \phi_{j+2}}{\Delta \eta^2} \quad (2.52)$$

The second-order accurate backward difference formula at farfield (j=N ) are

$$\frac{\partial \phi}{\partial \eta} = \frac{3\phi_j - 4\phi_{j-1} + \phi_{j-2}}{2\Delta \eta} , \qquad (2.53)$$

$$\frac{\partial^2 \phi}{\partial \eta^2} = \frac{\phi_j - 2\phi_{j-1} + \phi_{j-2}}{\Delta \eta^2} \quad . \tag{2.54}$$

At the grid point next to the solid boundary, j = 2, equations are descretized by the

third-order four-point finite difference scheme

$$\frac{\partial \phi}{\partial \eta} = \frac{-\phi_{j-1} + 6\phi_j - 3\phi_{j+1} - 2\phi_{j+2}}{6\Delta \eta} , \qquad (2.55)$$

$$\frac{\partial^2 \phi}{\partial \eta^2} = \frac{\phi_j - 2\phi_{j+1} + \phi_{j+2}}{\Delta \eta^2} \quad (2.56)$$

Similarly at j = N - 1, third-order four-point finite difference scheme is

$$\frac{\partial \phi}{\partial \eta} = \frac{2\phi_{j-2} + 3\phi_{j-1} - 6\phi_j - 2\phi_{j+1}}{6\Delta \eta} , \qquad (2.57)$$

$$\frac{\partial^2 \phi}{\partial \eta^2} = \frac{\phi_j - 2\phi_{j+1} + \phi_{j+2}}{\Delta \eta^2} \quad . \tag{2.58}$$

At the interior points  $(j = 3 \rightarrow N - 2)$  the equations are descretized using fourth-order central difference formula

$$\frac{\partial \phi}{\partial \eta} = \frac{-\phi_{j+2} + 8\phi_{j+1} - 8\phi_{j-1} + \phi_{j-2}}{12\Delta \eta} , \qquad (2.59)$$

$$\frac{\partial^2 \phi}{\partial n^2} = \frac{-\phi_{j+2} + 16\phi_{j+1} - 30\phi_j + 16\phi_{j-1} - \phi_{j-2}}{12\Delta n^2} \quad . \tag{2.60}$$

The descretized system of equations yields an algebraic system equations of the form

$$\mathbf{AL2}\Phi_{j-2} + \mathbf{AL1}\Phi_{j-1} + \mathbf{AD}\Phi_j + \mathbf{AU1}\Phi_{j+1} + \mathbf{AU2}\Phi_{j+2} = \mathbf{0};$$

$$j = 2, N-1.$$
(2.61)

Here AL2, AL1, AD, AU1 and AU2 refer to the lower subdiagonal, subdiagonal, diagonal, superdiagonal and upper superdiagonal matrices of size (5x5) respectively.  $\Phi_j$  represents the vector  $\hat{\mathbf{q}}$  at grid point j. The descretized system of equations and the homogeneous boundary conditions at the wall and at the outer boundary yield a homogeneous block penta-diagonal system of the equations as shown in figure 2.3.

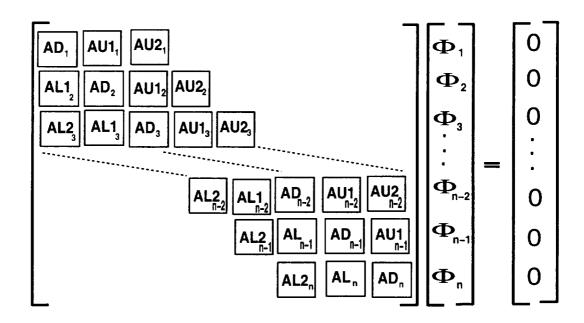


Fig. 2.3 Block penta-diagonal system

### 2.2.2 2D Eigenvalue Problem

In this section, the numerical procedure that is used to solve the 2D eigenvalue problem is described. The linear stability equations for this case is given in equation Eq. 2.37. As it was discussed previously, the eigenfunctions are now functions of azimuthal  $(x_2)$  and normal  $(x_3)$  coordinates. The derivatives in the normal direction can be descretized using the fourth-order central difference scheme that is used in the solution of 1D problem. The problem is how to descretize the derivatives in the azimuthal direction. First, they were descretized using the central finite difference scheme. The solution that was obtained were very oscillatory and it was necessary to distribute too many grid points in the  $x_2$  direction. This turned out to be very expensive and required enormous memory. Therefore, this method was abandoned and it was decided to use the Fourier series method to resolve the variables in the  $x_2$  direction.

In this method, the dependent variables  $\hat{\mathbf{q}}$  and the coefficients of the partial differential equations  $A_2$ ,  $A_3$ ,  $A_{23}$ ,  $B_2$ ,  $B_3$  and C are represented by Fourier series in the form

$$\hat{\mathbf{q}}(x_2, x_3) = \sum_{n = -\infty}^{n = \infty} \hat{\mathbf{q}}_{\mathbf{n}}(x_3)e^{inx_2}, \qquad (2.62)$$

$$\mathbf{A}(x_2, x_3) = \sum_{m=-\infty}^{m=\infty} \tilde{\mathbf{A}}_{\mathbf{m}}(x_3) e^{imx_2} , \qquad -\pi \le x_2 \le \pi .$$
 (2.63)

In the numerical procedure, it is necessary to replace the infinite Fourier series by finite sums in the form

$$\hat{\mathbf{q}}(x_2, x_3) = \sum_{n = -N_{max}}^{n = N_{max}} \hat{\mathbf{q}}_{\mathbf{n}}(x_3) e^{inx_2}, \qquad (2.64)$$

$$\mathbf{A}(x_2, x_3) = \sum_{m=-M_{max}}^{m=M_{max}} \tilde{\mathbf{A}}_{\mathbf{m}}(x_3) e^{imx_2} , \qquad -\pi \le x_2 \le \pi , \qquad (2.65)$$

where  $N_{max}$  and  $M_{max}$  are the maximum number of modes kept in the Fourier expansions for the disturbances and their coefficients respectively. The Fourier components

 $\mathbf{ ilde{A}_m}$  are obtained using the Discrete Fourier Transform formula

$$\tilde{\mathbf{A}}_{\mathbf{m}} = \frac{1}{2M_{max}} \sum_{m=-M_{max}}^{M_{max}-1} \mathbf{A}_{\mathbf{m}}(x_2, x_3) e^{imx_2} . \tag{2.66}$$

The derivatives of the eigenfunction  $\hat{\mathbf{q}}(x_2, x_3)$  in the  $x_2$  direction now become

$$\frac{\partial \hat{\mathbf{q}}(x_2, x_3)}{\partial x_2} = \sum_{n=-N_{max}}^{N_{max}} in \hat{\mathbf{q}}_{\mathbf{n}}(x_3) e^{inx_2} , \qquad (2.67)$$

$$\frac{\partial^2 \hat{\mathbf{q}}(x_2, x_3)}{\partial x_2^2} = \sum_{n = -N_{max}}^{n = N_{max}} (-n^2) \hat{\mathbf{q}}_{\mathbf{n}}(x_3) e^{inx_2}$$
 (2.68)

Substituting these expressions into the governing equation and collecting terms, one obtains the following ordinary differential equation for each Fourier mode,  $n_o$ .

$$\sum_{n=N_1}^{n=N_2} \tilde{\mathbf{A}}_{3(\mathbf{n_0}-\mathbf{n})} \frac{d^2 \hat{\mathbf{q}}_{\mathbf{n}}}{dx_3^2} + \left( in \tilde{\mathbf{A}}_{23(\mathbf{n_0}-\mathbf{n})} + \tilde{\mathbf{B}}_{3(\mathbf{n_0}-\mathbf{n})} \right) \frac{d \hat{\mathbf{q}}_{\mathbf{n}}}{dx_3}$$

$$+ \left\{ -n^2 \tilde{\mathbf{A}}_{2(\mathbf{n_0}-\mathbf{n})} + in \tilde{\mathbf{B}}_{2(\mathbf{n_0}-\mathbf{n})} + \tilde{\mathbf{C}}_{(\mathbf{n_0}-\mathbf{n})} \right\} \hat{\mathbf{q}}_{\mathbf{n}} = 0, (2.69)$$

$$n_0 = -N_{max}, N_{max}.$$

Here

$$N_{1} = min\{N_{max}, n_{o} + M_{max}\},$$

$$N_{2} = max\{-N_{max}, n_{o} - M_{max}\}.$$
(2.70)

Since the mean velocity is symmetric about the windward plane,  $x_2 = 0$ , the stability equations permit symmetric and antisymmetric type disturbances. For symmetric disturbances, the Fourier modes are related by

$$\{\hat{u}_{1(-n)}, \hat{u}_{3(-n)}, \hat{\rho}_{-n}, \hat{\theta}_{-n}\} = \{\hat{u}_{1(n)}, \hat{u}_{3(n)}, \hat{\rho}_{n}, \hat{\theta}_{n}\}, \tag{2.71}$$

$$\hat{u}_{2(-n)} = -\hat{u}_{2(n)}; \quad n = 0, N_{max}$$
 (2.72)

and for antisymmetric disturbances

$$\{\hat{u}_{1(-n)}, \hat{u}_{3(-n)}, \hat{\rho}_{-n}, \hat{\theta}_{-n}\} = -\{\hat{u}_{1(n)}, \hat{u}_{3(n)}, \hat{\rho}_{n}, \hat{\theta}_{n}\}, \tag{2.73}$$

$$\hat{u}_{2(-n)} = \hat{u}_{2(n)}; \quad n = 0, N_{max}$$
 (2.74)

Hence, it is sufficient to solve the equation, Eq. 2.69, for  $n_o = 0$ ,  $N_{max}$ . Now, the equations Eq. 2.69 which is similar to equation Eq. 2.44 in 1D problem and can be solved using the fourth-order central difference scheme. When the equation Eq. 2.69 is descretized using the fourth-order central formula, again an algebraic system of equations in the form

$$\mathbf{AL2}\Phi_{j-2} + \mathbf{AL1}\Phi_{j-1} + \mathbf{AD}\Phi_j + \mathbf{AU1}\Phi_{j+1} + \mathbf{AU2}\Phi_{j+2} = \mathbf{0};$$

$$j = 2, N-1.$$
(2.75)

is obtained. The size of the matrices AL2, AL1, AD, AU1 and AU2 now becomes  $\{5x(N_{max}+1), 5x(N_{max}+1)\}$ . The descretized system of equations and the homogeneous boundary conditions at the wall and at the outer boundary again yield a homogeneous block penta-diagonal system of equations as shown in figure 2.3.

Eventhough the block penta-diagonal system can be solved efficiently, it was found that if the system is rewritten as a banded system it can be solved two times faster using the LAPACK subroutines ZGBTRF and ZGBTRS. The transformation of penta-diagonal matrix system into a banded matrix is easily implemented as quoted in LAPACK user's guide.

If A represents the penta-diagonal matrix system i.e,

$$\mathbf{A} = \begin{bmatrix} [AD] & [AU1] & [AU2] \\ [AL1] & [AD] & [AU1] & [AU2] \\ [AL2] & [AL1] & [AD] & [AU1] & [AU2] \\ & \ddots & \ddots & \ddots \\ & & & [AL2] & [AL1] & [AD] \end{bmatrix}$$
(2.76)

minimum requirement of 50 Fourier modes in the azimuthal direction and 30 points in the wall-normal direction, the size of the matrix  $\mathbf{A}$  becomes (5x50)x30 = 7500 and it takes about 32 hours of CPU-time on a Sun-Ultra 2 workstation.

However, in real situations it is not required to find all the eigenvalues. It is sufficient to compute a few most unstable eigenmodes. This can easily be obtained using Implicitly Restarted Arnoldi Method using ARPACK software package developed by Lehoucq, Sorensen, Yang [1]. This method finds specified number of eigenvalues in a region close to a specified point in the complex  $\omega$  plane very efficiently. When applied to an eigenvalue problem with the matrix  $\mathbf{A}$  of a size of 10000, it takes only 20 minutes on the same workstation mentioned above to compute 10 eigenvalues located close to the specified point in the complex  $\omega$  plane.

The rest of the section will focus on the details involved in the formulation of generalized eigenvalue problem to be solved using the Arnoldi Method. It is observed from linear stability equation Eq. 2.34, that the frequency  $\omega$  appears as simple rems of first power.

- Continuity equation :  $-i\omega\rho + \cdots$ ,
- $x_1$  momentum equation :  $-i\omega \overline{\rho}u_1 + \cdots$ ,
- $x_2$  momentum equation :  $-i\omega \overline{\rho}u_2 + \cdots$ ,
- $x_3$  momentum equation :  $-i\omega \overline{\rho}u_3 + \cdots$ ,
- Energy equation :  $-i\omega \overline{\rho}\theta + \cdots$

Therefore, in an attempt to capture the eigenvalues accurately, the global method is formulated as a temporal one. The temporal global eigenvalue formulation is as follows.

In order to solve an eigenvalue problem like equation Eq. 2.78 using the Arnoldi algorithm using the software package ARPACK, it is required that the matrix  $\overline{\bf B}$  be a symmetric positive definite or a symmetric semi-definite. The appearance of temporal frequency  $\omega$  as a first power terms only, in the stability equations, suggest an appropriate selection of disturbance vector of  ${\bf q}=\{u_1,u_2,u_3,\rho,\theta\}^T$  with corresponding order of stability equations -  $x_1$  momentum,  $x_2$  momentum,  $x_3$  momentum equations, continuity equation and energy equation respectively. This assures the diagonal, and hence symmetric formation of matrix  $\overline{\bf B}$ . This is the reason for replacing pressure fluctuation  $\pi$  by density and temperature in the stability equations.

A further reduction of the generalized eigenvalue problem Eq. 2.78 to a more storage efficient standard eigenvalue formulation of the form

$$\overline{\mathbf{A}}\mathbf{\Phi} = \omega\mathbf{\Phi} , \qquad (2.79) \cdot$$

can be obtained by manipulating the homogeneous boundary conditions. The procedure will be explained for the case of 1D eigenvalue formulation, and the similar manipulation can be applied to 2D eigenvalue as well. The only zero rows in matrix  $\overline{\mathbf{B}}$  are that corresponds to the boundary conditions  $u_1, u_2, u_3$  and  $\theta$  as shown below.

$$\begin{bmatrix} 1 & 0 & 0 & 0 & 0 & \cdots \\ 0 & 1 & 0 & 0 & 0 & \cdots \\ 0 & 0 & 1 & 0 & 0 & \cdots \\ Cont & eqn & \cdots \\ \vdots & \vdots & \vdots & \vdots & \vdots & \ddots \end{bmatrix} \begin{bmatrix} \begin{bmatrix} u_1 \\ u_2 \\ u_3 \\ \rho \\ \theta \end{bmatrix}_1 \\ \vdots & \vdots & \vdots & \vdots \end{bmatrix} = \omega \begin{bmatrix} 0 \\ 0 \\ 0 \\ 0 \\ \vdots & \vdots & \vdots & \vdots \end{bmatrix} \begin{bmatrix} \begin{bmatrix} u_1 \\ u_2 \\ u_3 \\ \rho \\ \theta \end{bmatrix}_1 \\ \vdots & \vdots & \vdots & \vdots \end{bmatrix} \begin{bmatrix} \begin{bmatrix} u_1 \\ u_2 \\ u_3 \\ \rho \\ \theta \end{bmatrix}_1 \\ \vdots & \vdots & \vdots & \vdots \end{bmatrix}$$

And the middle elements of  $\overline{\mathbf{B}}$  take the form

$$\overline{\mathbf{B}} = \begin{bmatrix} \ddots & & & & & \\ & i\overline{\rho} & & & & \\ & & i\overline{\rho} & & & \\ & & & i\overline{\rho} & & \\ & & & i\overline{\rho} & & \\ & & & i\overline{\rho} & & \\ \vdots & \vdots & \vdots & \vdots & \vdots & \vdots & \ddots \end{bmatrix}$$
 (2.81)

Without any loss of generality in the boundary conditions, the zero terms in  $\overline{\mathbf{B}}$  can be replaced by unity. Further, dividing the continuity equation by i and momentum and energy equations by  $i\overline{\rho}$  will make  $\overline{\mathbf{B}}$  an identity matrix. Hence the resulting eigenvalue problem is reduced to equation Eq. 2.79.

#### 2.2.4 Local Method

The local methods are used to confirm and refine the eigenvalues obtained from global solver. But, global methods are computationally much more expensive than the local methods since they compute the whole or part of the eigenvalue spectrum of the descretized system. However, the local eigenvalue solvers require a guess for the eigenvalue and hence make the use of a global solver inevitable.

It was shown earlier that, the system of descretized stability equations can be formed as a lock penta-diagonal system or as banded matrix format. It can be seen that these equations are homogeneous and in order to avoid trivial solutions, Malik [34] suggests replacement of boundary condition  $u_{1(x_3=0)}=0$  by the normalizing condition that the pressure fluctuation (or equivalently density fluctuation in the present case)  $\pi_{(x_3=0)}=1$ . Thus, the equations are transformed into an inhomogeneous system. But here, a different approach will be followed. After experimenting with a number of different normalizations, it was found that a faster rate of convergence resulted by replacing continuity equation in the middle of the boundary

layer wall-normal location by the normalizing condition  $u_1 = 1$ . (In the case of 2D eigenvalue problem, a Fourier mode  $u_{1n} = 1$  is used for normalization).

Consider the missing continuity equation denoted by  $\psi(\lambda) = 0$ . Here  $\lambda$  refers to the exact eigenvalue i.e, the streamwise wavenumber  $\alpha$  if it is spatial formulation or temporal frequency  $\omega$  if the problem is considered as temporal.

Suppose  $\lambda_o$  represents the guess for the eigenvalue and  $\Delta\lambda$  the error from the exact value so that  $\psi(\lambda + \Delta\lambda) = 0$ . Now, using Taylor series expansion for  $\Delta\lambda$ 

$$\psi(\lambda_o) + \frac{\partial \psi}{\partial \Delta \lambda} \Delta \lambda = 0 , \qquad (2.82)$$

$$\Delta \lambda = -\frac{\psi(\lambda_o)}{(\partial \psi/\partial \Delta \lambda)}$$
 (2.83)

The iterative procedure for local 1D temporal stability will be described below.

- \* For a specified wavenumber  $\alpha$ , formulate the penta-diagonal system for shapefunction  $\hat{\mathbf{q}}$ , normalize the with  $u_1=1$  by replacing continuity equation at wall-normal grid point  $j_{mid}$  where the phase speed  $C=\omega_r/\alpha_r$  is about 0.7.
- \* Iterate on the guess value for temporal frequency  $\omega_o$  until the missing continuity equation is satisfied. The correction  $\Delta\omega$  is determined from the equation Eq. 2.83.

The procedure for spatial formulation is similar; where temporal frequency  $\omega$  is fixed and the Newton-Raphson iteration is done on guess value for  $\alpha$  until convergence is reached. For 2D eigenvalue problem, a Fourier component with maximum amplitude is used for the normalization.

# 2.3 Summary

To conclude this chapter, the formulation are summarized as a schematic diagram.

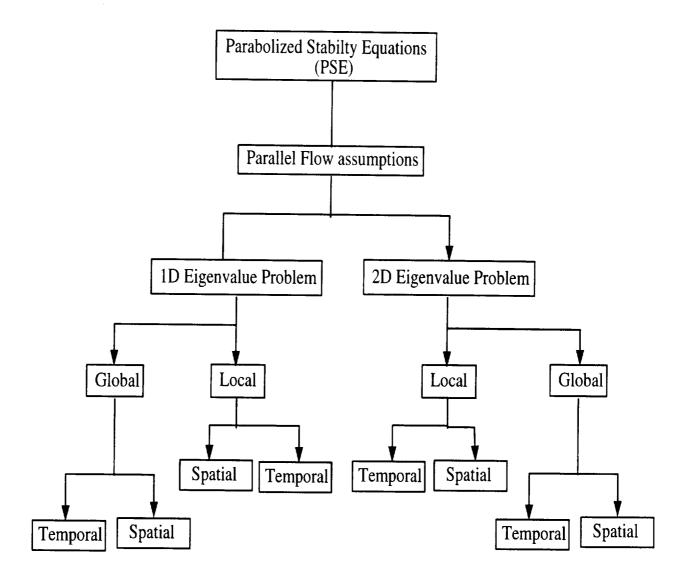


Fig. 2.4 Stability problem formulation

#### CHAPTER 3

# MEANFLOW COMPUTATIONS

The stability computations basically involve two steps. The first step is to compute the mean velocity profiles accurately. The mean flow can be obtained by solving the boundary layer equations, Parabolized Navier-Stokes (PNS) equations or full Navier-Stokes equations depending on the problem that is being analysed. In this work, we investigate the linear stability of supersonic boundary layers over a sharp axi-symmetric cone at an angle of attack. The mean flow was computed using the well developed TLNS3D code which was developed at NASA Langley Research Center by Vatsa and Wedan (1990) [3].

#### 3.1 TLNS3D

Three-dimensional time-dependent Thin-Layer Navier-Stokes equations are used in TLNS3D for modelling the flow. The set of equations are obtained from the complete Reynolds-averaged Navier-Stokes equation by retaining only the viscous diffusion terms normal to the solid surfaces. The TLNS3D code employs eddy-viscosity hypothesis to model turbulence; the Baldwin-Lomax turbulence model is used for turbulence closure. In this work, the mean flow is computed for laminar flow.

The steady-sate solutions to Thin-Layer Navier-Stokes equations are obtained using a semidiscrete cell-centered finite-volume algorithm, based on a Runge-Kutta time-stepping scheme. In order to suppress odd-even decoupling and oscillations in the vicinity of shock waves and stagnation points, a linear fourth order difference-based and nolinear second order difference-based dissipation is added. TLNS3D incorporates both the scalar and matrix forms of the artificial dissipation models; but in the mean-flow calculation over the sharp cone matrix form is used.

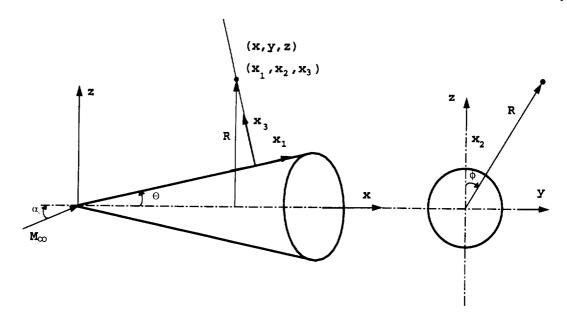


Fig. 3.1 The coordinate system for the cone located in a supersonic flow at an angle of attack ( $M_{\infty}=3.5$ ).

For the sharp cone the Cartesian coordinate system (x, y, z) is located at the vertex and a body-oriented coordinate system  $(x_1, x_2, x_3)$  fixed in time is considered with  $x_1$  along the generator,  $x_2$  in the azimuthal direction and  $x_3$  normal to the surface as shown in figure 3.1.

The coordinate transformation is given by

$$x_1 = x\cos(\Theta) + R\sin(\Theta) , \qquad (3.1)$$

$$tan(x_2) = y/z (3.2)$$

$$x_3 = R\cos(\Theta) - x\sin(\Theta) , \qquad (3.3)$$

where

$$R^2 = y^2 + z^2 \cdot$$

The govering equations can be written in the conservation form for the body-fitted coordinate system as

$$\frac{\partial}{\partial t}(J^{-1}U) + \frac{\partial F}{\partial x_1} + \frac{\partial G}{\partial x_2} + \frac{\partial H}{\partial x_3} = \frac{\partial G_v}{\partial x_3}, \qquad (3.4)$$

where U is the conserved varibale vector and F, G, and H represents the convective flux vectors.  $G_v$  represents the viscous flux vectors normal to the body surface. Here only the viscous diffusion terms in the  $x_3$ -direction are retained, due to the fact that in high-Reynolds-number flows, dominent contribution to the viscous effects are from viscous diffusion normal to the body-surface.

$$U = \left\{ \begin{array}{c} \rho \\ \rho u \\ \rho v \\ \rho w \\ \rho E \end{array} \right\} , \tag{3.5}$$

$$F = J^{-1} \begin{cases} \rho u_1 \\ \rho u_1 u + x_{1x} p \\ \rho u_1 v + x_{1y} p \\ \rho u_1 w + x_{1z} p \\ \rho u_1 H \end{cases},$$

$$G = J^{-1} \begin{cases} \rho u_2 \\ \rho u_2 u + x_{2x} p \\ \rho u_2 v + x_{2y} p \\ \rho u_2 w + x_{2z} p \\ \rho u_2 H \end{cases},$$

$$(3.6)$$

$$G = J^{-1} \left\{ \begin{array}{l} \rho u_2 \\ \rho u_2 u + x_{2x} p \\ \rho u_2 v + x_{2y} p \\ \rho u_2 w + x_{2z} p \\ \rho u_2 H \end{array} \right\} , \tag{3.7}$$

$$H = J^{-1} \begin{cases} \rho u_3 \\ \rho u_3 u + x_{3x} p \\ \rho u_3 v + x_{3y} p \\ \rho u_3 w + x_{3z} p \\ \rho u_3 H \end{cases},$$
(3.8)

$$G_{v} = \frac{\sqrt{\gamma} M_{\infty} \mu}{Re_{\infty} J} \left\{ \begin{array}{c} 0\\ \phi_{1} u_{x_{3}} + x_{3x} \phi_{2}\\ \phi_{1} v_{x_{3}} + x_{3y} \phi_{2}\\ \phi_{1} w_{x_{3}} + x_{3z} \phi_{2}\\ \phi_{1} a + \tilde{v} \phi_{2} \end{array} \right\},$$
(3.9)

where

$$\phi_{1} = x_{3x}^{2} + x_{3y}^{2} + x_{3z}^{2},$$

$$\phi_{2} = \frac{1}{3} (x_{3x}u_{x_{3}} + x_{3y}v_{x_{3}} + x_{3z}w_{x_{3}}),$$

$$q^{2} = u^{2} + v^{2} + w^{2},$$

$$a = \left(\frac{q^{2}}{2}\right)_{x_{3}} + \left(\frac{\gamma}{\gamma - 1}\right) \frac{1}{Pr} T_{x_{3}}.$$

$$(3.10)$$

Here (u, v, w) are the velocity components in the (x, y, z) directions and  $(u_1, u_2, u_3)$  are the contravarient velocity components (velocities along the body-fitted coordinate directions) which are defined as

$$u_{1} = x_{1x}u + x_{1y}v + x_{1z}w ,$$

$$u_{2} = x_{2x}u + x_{2y}v + x_{2z}w ,$$

$$u_{3} = x_{3x}u + x_{3y}v + x_{3z}w ,$$

$$(3.11)$$

 $\rho$  is the density, p is the pressure, and E is the total energy. J is the Jacobian of the transformation and  $x_{ij}$  are the direction cosines. Additionally,  $\mu$  is the viscosity,  $M_{\infty} = \frac{U_e}{\sqrt{\gamma R T_e}}$  is the free-stream Mach number,  $Re_{\infty} = \frac{U_e}{\nu_e}$  is the free-stream unit Reynolds number, and  $Pr = \frac{\mu C_p}{R}$  is the Prandtl number.

Distribution of temperature can easily be obtained from the expression

$$T = \left[E - \frac{1}{2}(u^2 + v^2 + w^2)\right] \gamma(\gamma - 1)T_{\infty}$$
 (3.12)

Since the steady state flow is symmetric about the plane through the windward and leeward rays, the mean flow computations were done in the half plane (  $x_2=0^\circ$  to  $x_2=180^\circ$  ). By symmetry,

$$\{u_1, u_3, \rho, T\}|_{x_2} = \{u_1, u_3, \rho, T\}|_{-x_2},$$
 (3.13)

$$u_2|_{x_2} = -u_2|_{x_2} (3.14)$$

## 3.2 Boundary-layer Profiles

The physical parameters for which the computations were performed are given in table 3.1.

Table 3.1 Details of the cone problem

Parameter	Value
Half cone angle	5°
Angle of attack	2°
Free-stream temperature	$94^{o}K$
Free-stream Mach number	3.5
Unit Reynolds number	$8.7 \times 10^6 / m$
Cone length	1.574m

The computations were done at the adiabatic wall conditions. In the computation of the meanflow using TLNS3D a mesh size of (97x257x49), i.e, 97 points in the streamwise direction, 257 points in the normal direction and 49 points in the azimuthal direction ( windward ray to leeward ray) were used.

The mean-flow profiles at four different streamwise locations ( $x_1 = 0.033m$ , 0.197m, 0.3505m and 0.5105m), where the linear stability computations were performed, are presented. The thickness of the boundary layers at the four streamwise locations for different azimuthal stations are plotted in figures 3.3. Here, the bound-

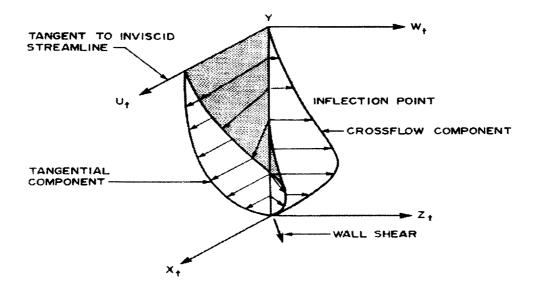


Fig. 3.2 Schematic diagram of cross-flow and streamwise velocity profile (Reed & Saric).

ary layer thickness is defined at a wall-normal location where the values of streamwise velocities at consecutive normal points differ by less than 0.1%. It is seen that the boundary layer thickness inceases sharply about three times when the flow goes from leaward to windward plane. In the left ordinate the boundary layer thickness is plotted in mm and in the right ordinate the nondimensional thickness  $x_3$  is shown, which is defined as

$$x_3 = \frac{{x_3}^*}{\sqrt{\frac{\nu^* x_1^*}{U_e^*}}}$$
 (3.15)

Figure 3.4 depict the variation of the boundary layer edge velocity  $U_e$  in the azimuthal direction at different streamwise locations. As it is seen the variation of the velocity is small in the azimuthal direction.

First, the meanflow profiles at the streamwise station  $x_1 = 0.033m$  are given. The velocity profiles tangent to the inviscid stream line at different azimuthal locations are shown in figure 3.5. There are significantly different characteristic profiles on the windward and leeward planes. On the windward side, boundary-

layer is comparatively thin and gradients are quite larger near the wall. On the leeward plane much thicker layer with smaller surface shear is apparant.

Figure 3.6 show the cross-flow profiles along azimuthal  $x_2$  locations. The cross-flow components were non-dimensionalized with the boundary-layer edge velocity, and positive cross-flow is taken towards positive  $x_2$  direction and away from  $x_1$  direction as shown in figure 3.2. The cross-flow velocities exhibit local maximum values at  $x_2 = 90^{\circ}$  and reaches values between 4% and 6% of the freestream velocity. Closer to the leeward side (around  $x_2 = 160^{\circ}$ ) negative cross-flow is evident i.e, cross-flow component changes in sign before it decays to zero towards the boundary-layer edge. As could be expected, cross-flow phenomena dissapear in windward and leeward rays due to the symmetry in the mean-flow.

Figure 3.7 shows the azimuthal velocity distributions at different azimuthal locations. Figures 3.8 and 3.9 show the density and temperature distributions at this  $x_1$  location. The similar results of the mean-flow profiles at the other three streamwise locations  $x_1 = 0.3505m$  and 0.5105m are presented in figures 3.11 to 3.19.

The velocities are nondimensionalized by the characteristic velocity  $U^*_e$  which is taken to be the local velocity at the edge of the boundary layer in the streamwise direction in 1D formulation and the boundary layer edge velocity at a reference station  $x_2 = 90^\circ$  in the case of 2D formulation. The normal coordinate is normalized by the length scale

$$\sqrt{\frac{\nu^{\star}_{e}x_{1}^{\star}}{U^{\star}_{e}}}, \qquad (3.16)$$

where  $\nu^*_e$  is the kinematic viscosity at the edge of the boundary layer. It is seen that except close to the leeward plane region the boundary layer profiles are almost linear in most part of the boundary layer and the boundary layer thickness increases gradually. Very close to the leeward plane, the profiles exhibit very strong inflectional

character, especially  $165^{\circ} < x_2 < 180^{\circ}$ . Figure 3.6 shows the crossflow velocity component in the positive  $x_2$  direction at different azimuthal locations. It is observed as expected that the crossflow velocity is zero at the windward and leeward planes and reaches maximum in the middle of the refion  $90^{\circ} < x_2 < 120^{\circ}$  The maximum crossflow velocity is about 4% of the boundary layer edge velocity. From this it is also expected that the boundary layer will be very unstable in the middle region compared to the region near the windward or leeward planes.

Figures 3.21 shows the contours of the crossflow Reynolds number defined by

$$Re_c = \frac{Q_{max}\delta_{10\%}}{\nu_e} \,, \tag{3.17}$$

in the  $x_1x_2$  plane. Here  $Q_{max}$  is the maximum cross-flow velocity (located at  $\delta_{max}$ ), and  $\delta_{10\%}$  is the thickness defined by the point above  $\delta_{max}$  at which the cross-flow velocity is 10% of  $Q_{max}$ . As expected the cross flow Reynolds number is maximum in the middle region and increases with the  $x_1$  direction. The maximum cross-flow Reynolds number is about 250 at  $x_1 = 0.5105m$ .

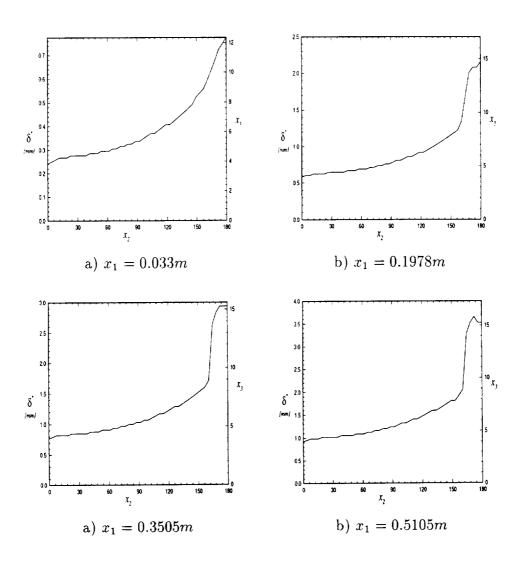


Fig. 3.3 The variation of boundary-layer thickness in the azimuthal direction at different streamwise locations.

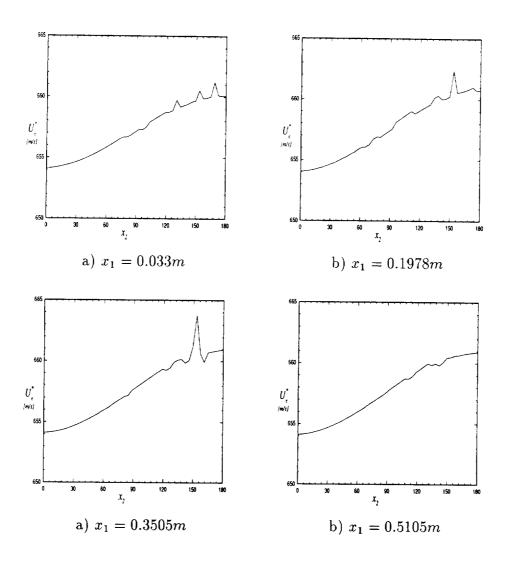


Fig. 3.4 The variation of boundary-layer edge velocity in the azimuthal direction at different streamwise locations.

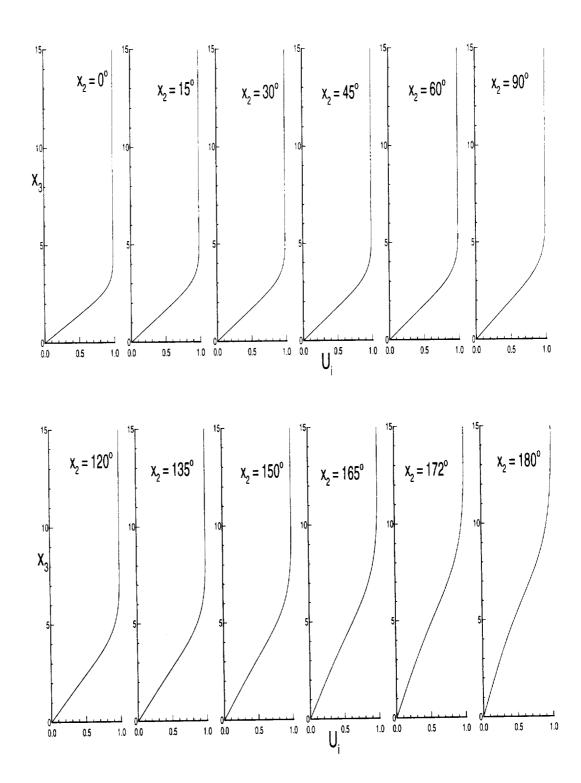
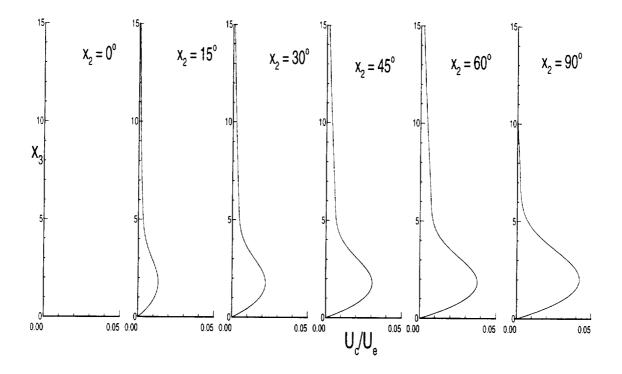


Fig. 3.5 Mean velocity profiles in the direction of the inviscid streamlines. (Re  $= 531, x_1 = 0.033m$ ).



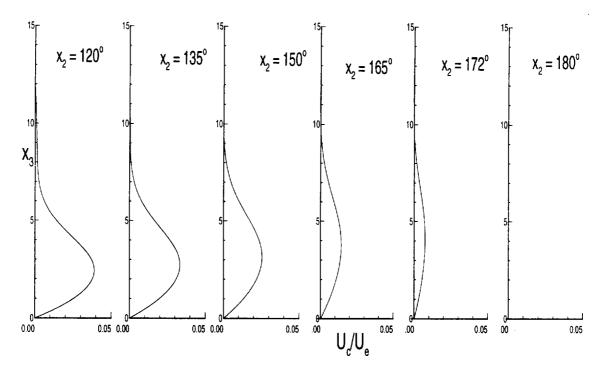
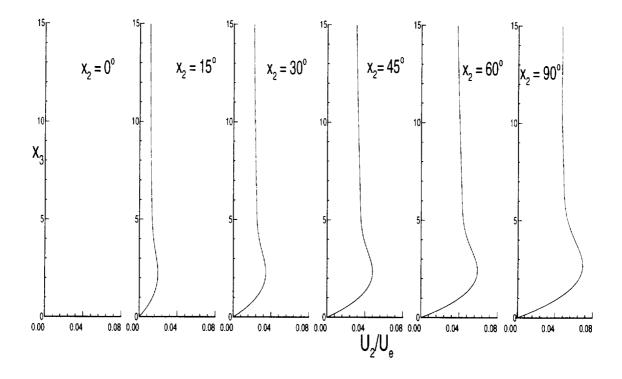


Fig. 3.6 Cross-flow velocity profiles (Re = 531,  $x_1 = 0.033m$ ).



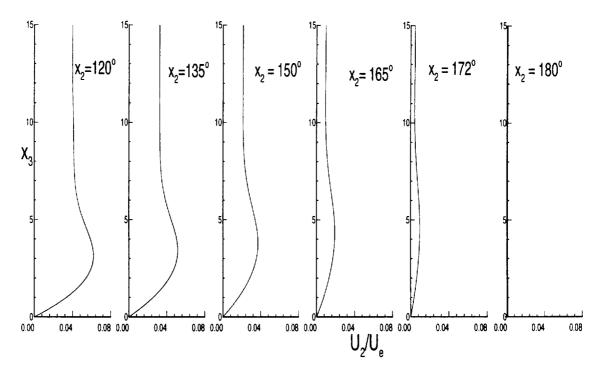


Fig. 3.7 Azimuthal velocity distributions at different  $x_2$  locations. (Re = 531,  $x_1 = 0.033m$ ).

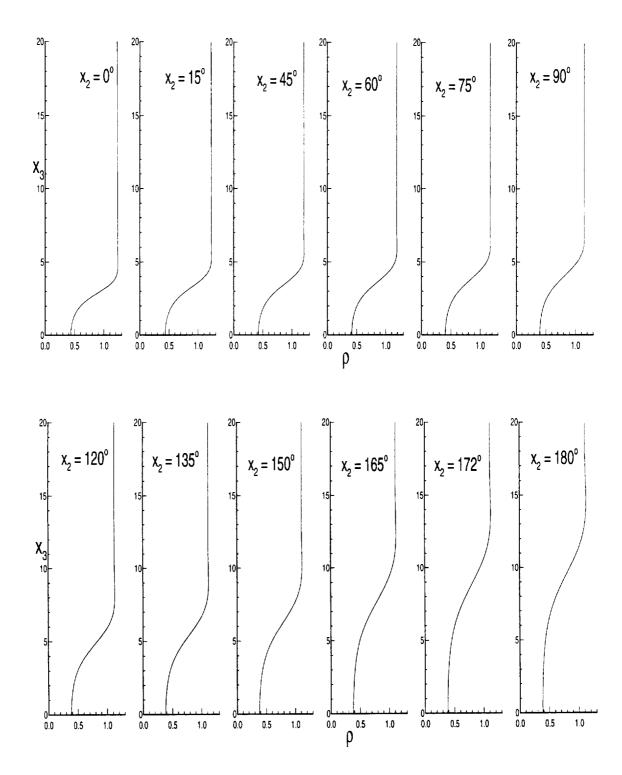


Fig. 3.8 Mean density variation in the normal direction at different  $x_2$  locations. (Re = 531,  $x_1 = 0.033m$ ).

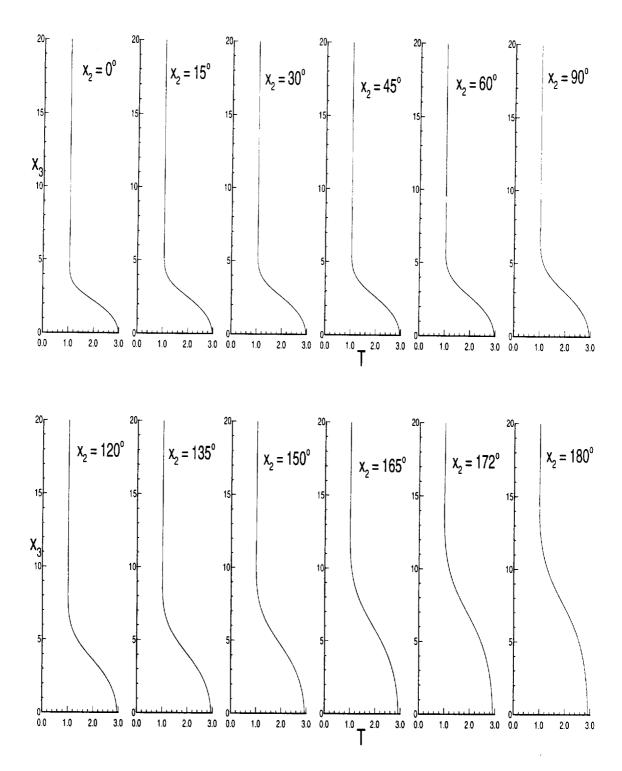


Fig. 3.9 Mean temperature variation in the normal direction at different  $x_2$  locations. (Re = 531,  $x_1 = 0.033m$ ).

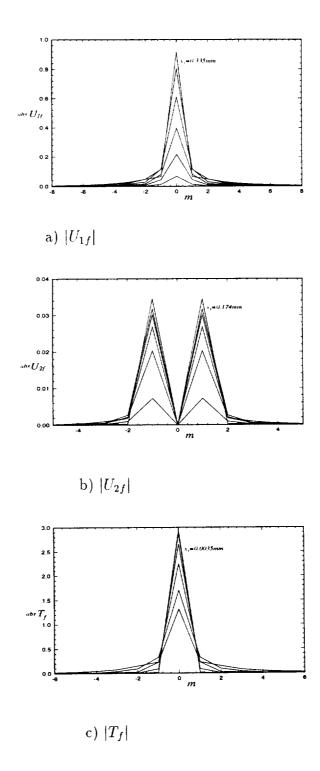


Fig. 3.10 The distribution of Fourier components of a) streamwise velocity, b) azimuthal velocity and c) temperature with Fourier modes m.

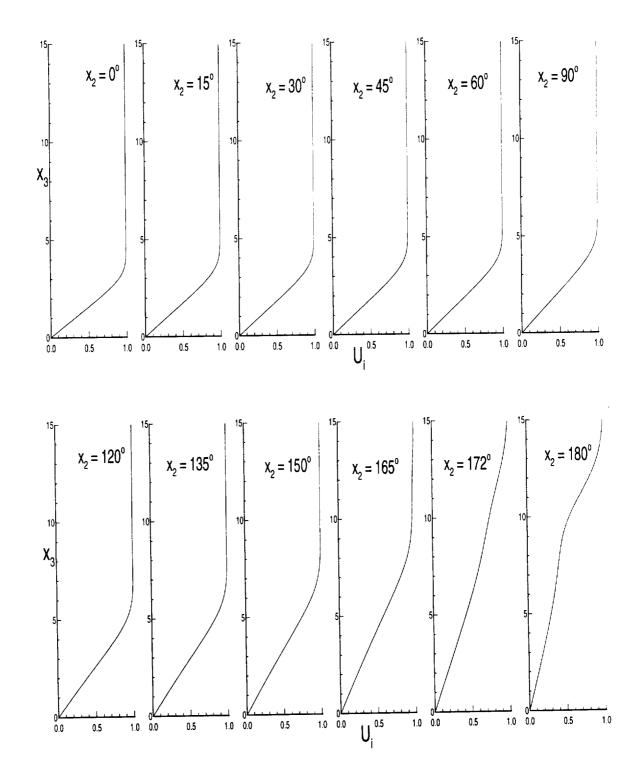
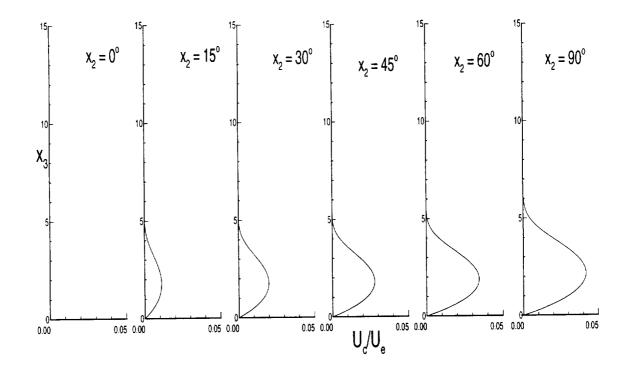


Fig. 3.11 Mean velocity profiles in the direction of the inviscid streamlines. (Re = 1823,  $x_1 = 0.3505m$ ).



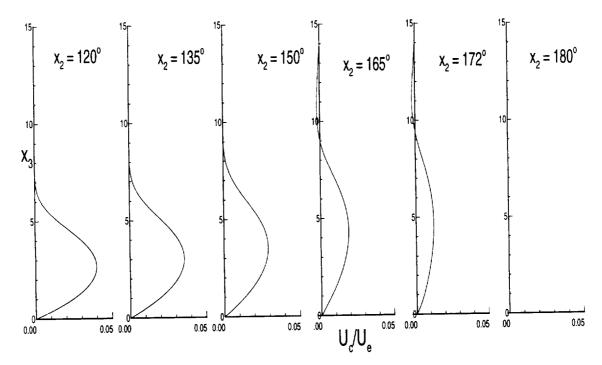


Fig. 3.12 Cross-flow velocity profiles. (Re = 1823,  $x_1 = 0.3505m$ ).

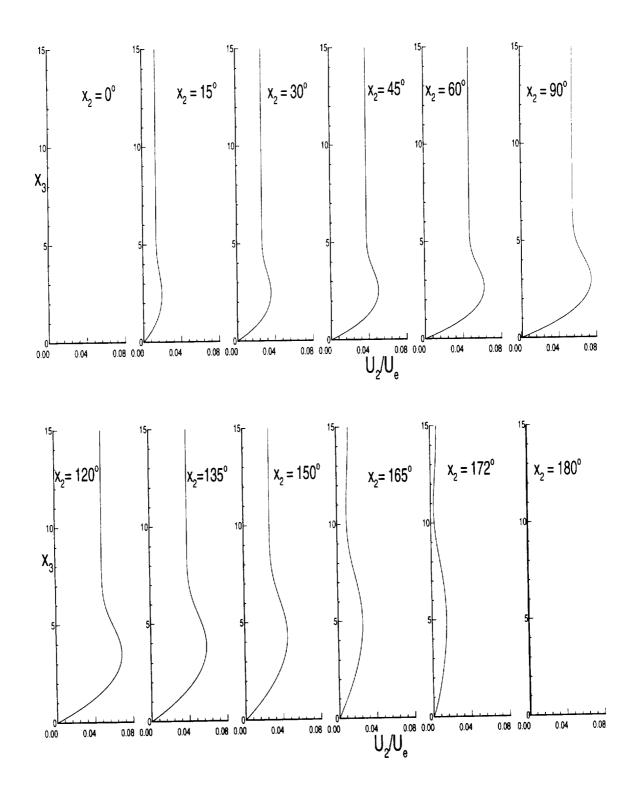


Fig. 3.13 Azimuthal velocity distributions at different  $x_2$  locations (Re = 1823,  $x_1 = 0.3505m$ ).

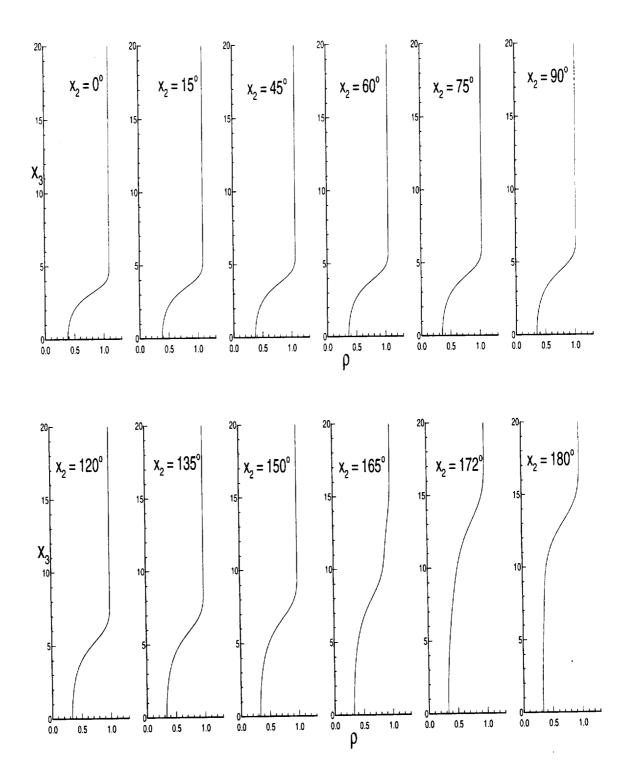


Fig. 3.14 Mean density variation in the normal direction at different  $x_2$  locations (  $Re=2211,\ x_1=0.5105\mathrm{m}$ )

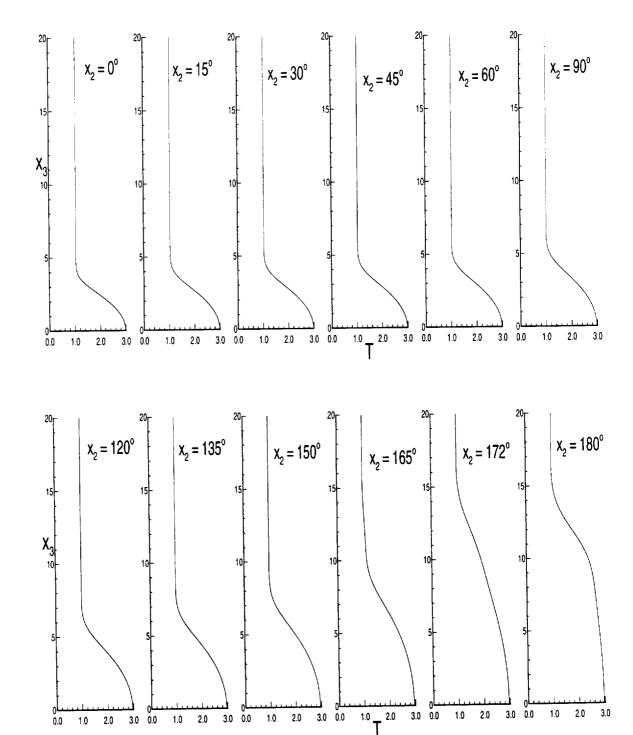


Fig. 3.15 Mean temperature variation in the normal direction at different  $x_2$  locations (Re = 2211,  $x_1 = 0.3505m$ ).

1.0

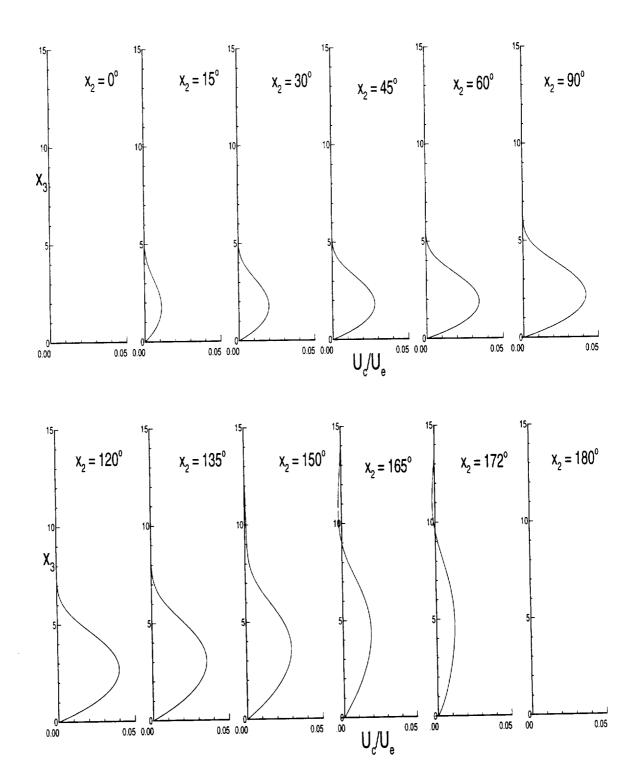
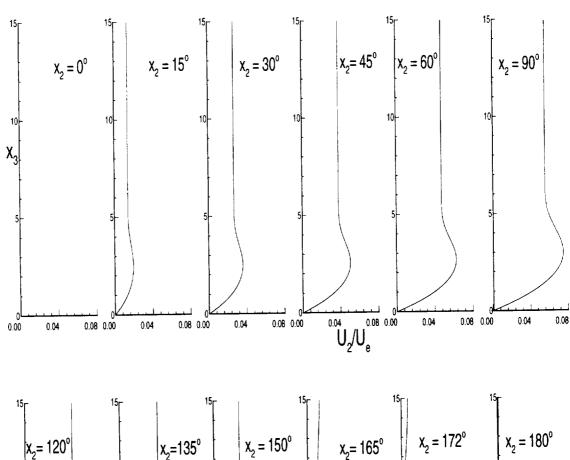


Fig. 3.17 Cross-flow velocity profiles. (Re = 2211,  $x_1 = 0.5105m$ ).



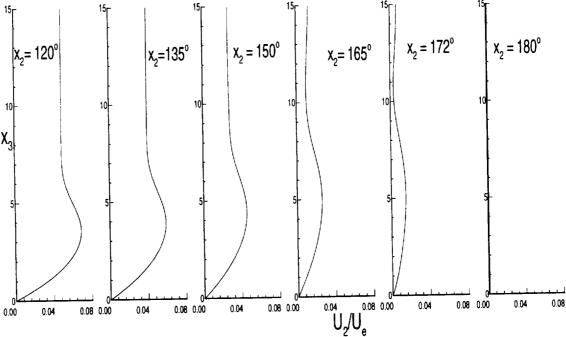


Fig. 3.18 Azimuthal velocity distributions at different  $x_2$  locations. (Re = 2211,  $x_1 = 0.5105m$ ).

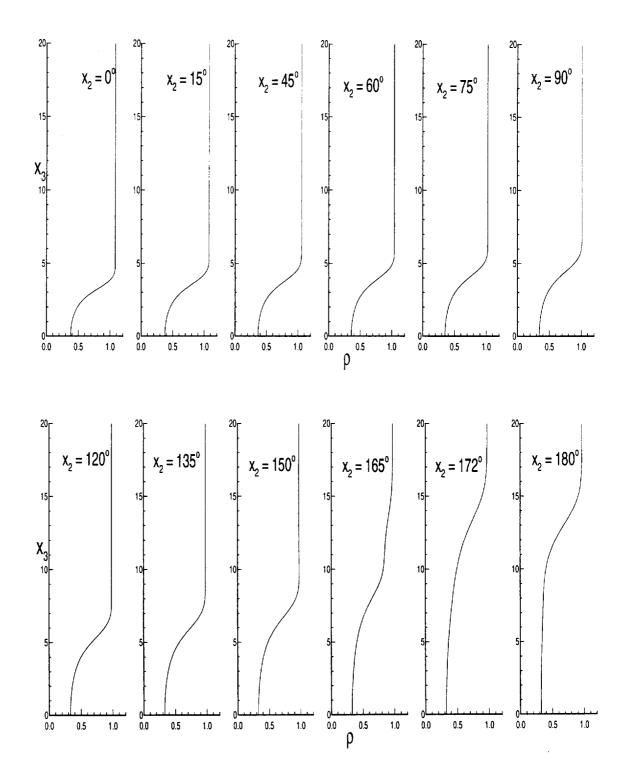


Fig. 3.19 Mean density variation in the normal direction at different  $x_2$  (Re = 2211,  $x_1 = 0.5105m$ ).

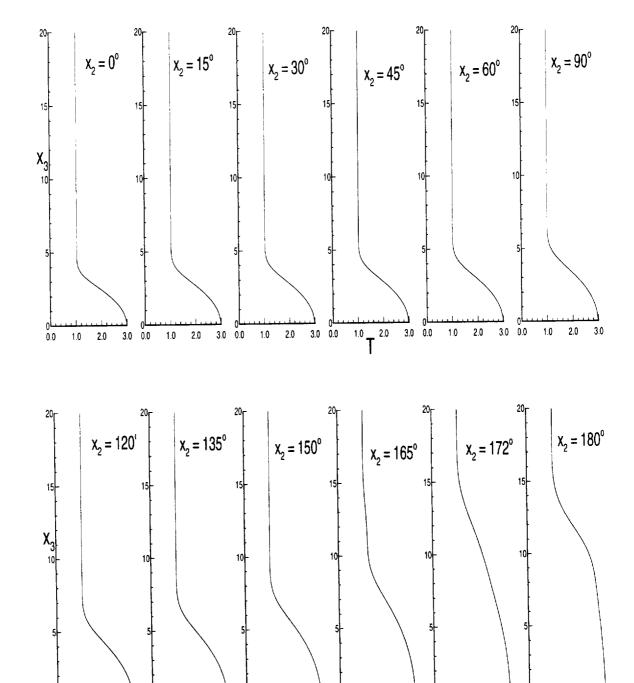


Fig. 3.20 Mean temperature variation in the normal direction at different  $x_2$  (Re = 2211,  $x_1 = 0.5105m$ ).

1.0 2.0 3.0 0.0

3.0 0.0

1.0 2.0 3.0 0.0 1.0 2.0 3.0 0.0 1.0 2.0 3.0 0.0

### CHAPTER 4

## RESULTS AND DISCUSSION

In this chapter, the linear stability results obtained using the 1D eigenvalue method and the 2D eigenvalue method are presented. In order to study the evolution of the disturbances downstream, the 1D and 2D stability computations are performed at different locations along the streamwise direction:  $x_1 = 0.033m$ , 0.197m, 0.3505m and 0.5105m. The results are presented in two sections. In the first section, the computational results from 1D eigenvalue approach are given and the results from the 2D eigenvalue approach are presented in section 2.

# 4.1 1D Eigenvalue problem

Before proceeding to present the linear 1D eigenvalue results, the computational grid used in the computations are described. As mentioned in Chapter 2, the height of the computational domain was taken to be about four times the boundary layer thickness. This was necessary because, eventhough most of the perturbations decay to zero within the boundary layer, density and normal velocity perturbations persist until about three to four times the boundary layer thickness. The computational domain consisted of 85 points in the wall-normal direction, with first 43 points clustered within the boundary layer according to the algebraic grid-stretching given by equation Eq. 2.47. Because of enormous requirement of the storage, the grids points in the 2D eigenvalue computation are limited to 49 points. To create a general platform for the comparison of linear 1D and 2D eigenvalue results, 1D eigenvalue problem was also solved on a grid size of 49 for few cases. The stability results computed on a grid size of 49 are found to be accurate within five decimal points to that of obtained with 85 grid points.

It was explained in Chapter 2 that in the eigenvalue computations, since the local method requires a guess value, a global method has to be first used to compute the whole or part of the eigenvalue spectrum. In the present work, the 1D global eigenvalue computations are performed using the QZ algorithm of the subroutine ZGEGV in LAPACK software library. For a typical 1D problem with 85 points in the normal direction, the leading dimension of the matrix  $\overline{\bf A}$  of the generalized eigenvalue problem becomes (5x85) = 425 and it takes only 30 seconds on a Sparc-Ultra-2 workstation (333MHz) to compute all of the eigenvalues. These spectrum of eigenvalues showed only one, or two physical eigenvalues which are unstable. It was found that, in 1D eigenvalue computations, the initial guess value need not be close to the unstable eigenvalue sought. Therefore, 1D eigenvalue computations are performed, in most cases, using the iterative local solver by the continuation method, i.e, using the eigenvalue at the previous location as the initial guess for the current location.

To orient the reader with the co-ordinate system used, a schematic diagram showing flow and wave propagation directions is depicted in figure 4.1. Here m which

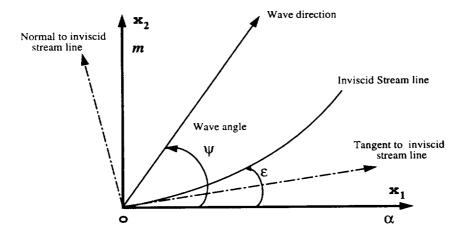


Fig. 4.1 Schematic diagram of the flow and the wave directions

is an integer, is the number of waves in the azimuthal direction. In order to determine the unstable region of the boundary layer, first several eigenvalue computations were performed along the azimuthal direction from windward ray to the leeward ray at number of fixed streamwise locations  $x_1$ , for different streamwise wavenumber  $\alpha$  and azimuthal mode number m. A sequence of such computations starting from a  $x_1$  location closer to the tip of the cone exhibited that the region up to  $x_1 = 0.03m$  is linearly stable. Hence, the linear stability results at four  $x_1$  locations starting from  $x_1 = 0.033m$  are given here. The length, velocity and time scales used to nondimensionalize the variables are as follows.

Table 4.1 Parameters used in nondimensionalization of different scales.

Parameter	Streamwise distance, $x_1/[m]$			
	0.033	0.197	0.3505	0.5105
L/[mm]	0.0627	0.146	0.192	0.231
$U_e/[m/s]$	663.3	659.7	658.4	658.2
$t \times 10^8 / [s]$	9.46	22.13	29.18	35.11

The linear 1D stability results at streamwise locations  $x_1 = 0.033m$ ,  $x_1 = 0.197m$ ,  $x_1 = 0.3505m$  and  $x_1 = 0.5105m$  are shown in the figures 4.2 to 4.6, 4.8 to 4.11, 4.12 to 4.19 and 4.20 to 4.22 respectively. Because the stability results at these stations are similar, only the results at  $x_1 = 0.033m$  and  $x_1 = 0.3505m$  are discussed in details.

### $x_1 = 0.033m$

The figures 4.2a, 4.2b, 4.3a and 4.3b show the variation of temporal amplification rates  $\omega_i$  and temporal frequency  $\omega_r$  with streamwise wavenumber  $\alpha$  for different azimuthal mode number m computed at the streamwise location  $x_1 = 0.033m$  at different azimuthal positions  $x_2 = 45^\circ$ ,  $x_2 = 90^\circ$ ,  $x_2 = 120^\circ$  and  $x_2 = 150^\circ$  respectively. The results show that the temporal frequency  $\omega_r$  varies linearly with

wavenumber  $\alpha$  for all the azimuthal mode numbers shown and that the phase speeds, defined as  $C = \frac{\alpha_r}{\omega_r}$ , are approximately constant and equal to 0.7. Further, the stationary waves, i.e,  $\omega_r = 0$ , are stable at this  $x_1$  location. At  $x_2 = 45^\circ$ , the disturbances are linearly unstable for -15 < m < -9. The maximum amplification rate is about 0.0006 and occurs at m = -12 and  $\alpha = 0.1$ . The similar variations of the temporal amplification rates are observed at  $x_2 = 90^\circ$ ,  $x_2 = 120^\circ$  and  $x_2 = 150^\circ$ . However, as one moves from the windward side  $x_2 = 45^\circ$ , toward the leeward side  $x_2 = 150^\circ$ , the unstable streamwise wavenumber  $\alpha$  shift from a range of  $(0.07 \sim .13)$  to  $(0.02 \sim 0.07)$ . The locally most amplified frequency is found to be  $\omega = (0.038, 0.00101)$  at the azimuthal location of  $x_2 = 120^\circ$  for  $\alpha = 0.07$  and m = -9 and  $\omega = (0.03, 0.00103)$  at  $x_2 = 150^\circ$  for  $\alpha = 0.05$  and m = -6. The negative sign of the mode number m indicates that the propagation of the disturbance wave is in the negative side of  $x_2$ .

The local wave propagation direction is given by

$$\psi = tan^{-1} \frac{\left(\frac{m}{R}\right)}{\alpha_r} \tag{4.1}$$

where R is the radius of the cone. The wave angles for the most amplified wave at different  $x_2$  locations are given in the Table 4.2. In this table,  $\epsilon$  is the inclination of the inviscid stream line to the  $x_1$  axis (figure 4.1). One can see that in the negative  $x_2$  direction most amplified waves are inclined at about 70° from the inviscid stream line. Figures 4.4 and 4.5 show the variation of the amplification rate  $\omega_i$  and the

Table 4.2 The waveangles for the most amplified wave at different  $x_2$  locations.

$x_2/[^o]$	$\epsilon/[^o]$	$-\psi/[^{\circ}]$	$\phi = -\psi + \epsilon$
45	1.68	69.09	70.77
90	2.73	69.09	71.82
120	2.30	71.67	73.39
150	1.22	71.02	72.24

frequency  $\omega_r$  along the azimuthal direction for a constant wavenumber  $\alpha=0.05$ 

for different azimuthal mode number m. Figures 4.6 and 4.7 depict the results for  $\alpha = 0.07$ . It is observed that the frequencies are lower in the middle than they are near the windward and leeward regions. This is due to the fact that cross-flow instability is dominated by low frequency disturbances compared to that without the cross-flow. As discussed in Chapter 2, the cross-flow is maximum in the middle region and hence the most unstable disturbances are low frequencies compared to that near the windward and leeward plane.

### $x_1 = 0.3505m$

The variation of the temporal amplification rate  $\omega_i$  and frequency  $\omega_r$  with wavenumber  $\alpha_r$  at  $x_2 = 0^{\circ}$ ,  $20^{\circ}$ ,  $41^{\circ}$ ,  $97^{\circ}$ ,  $120^{\circ}$  and  $160^{\circ}$  at the streamwise location  $x_1 = 0.3505m$  are plotted in figures 4.12a, 4.12b, 4.13a, 4.13b, 4.14a and 4.14b. Figures 4.15 and 4.16 show the variation of the amplification rate and the frequency along the azimuthal direction for a constant wavenumber  $\alpha = 0.07$  for different azimuthal mode number m. It is seen from the figure 4.12 that the amplification rates are the highest closer to  $\alpha = 0.07$ . First observation is that the amplification rates are high for disturbances with m = -30 to -40. The maximum amplification rate is  $\omega_i =$ 0.0046 and this occurs around  $x_2 = 90^\circ$  for m = -30 and  $\alpha = 0.07$ . The amplification rates between  $40^{\circ} < x_2 < 130^{\circ}$  vary in the range from 0.004 to 0.0046 and it decreases gradually to 0.0026 and 0.003 at  $x_2 = 0^\circ$  and 160° respectively. The most unstable frequencies are lower in the middle region compared to that near the windward and leeward planes. For m=-30 and  $\alpha=0.07$  the frequency of unstable disturbance is 0.039 at  $x_2 = 80^\circ$  and they are 0.046 and 0.051 at  $x_2 = 0^\circ$  and 160° respectively. These translate to 17.67 kHz at  $x_2=80^\circ$  and 20.83 kHz and 23.1 kHz at  $x_2=0^\circ$  and 160° respectively. It is also seen that the frequencies of the unstable disturbances decrease with increasing negative m. For m = -60, the unstable frequency is 0.034 at  $x_2 = 80^{\circ}$  and it is 0.041 for m = -20. The reason for this is that with increasing m, the wavevector aligns closer to the cross-flow direction and the frequencies of the unstable disturbances decrease. The results show that the amplification rate of the disturbances with positive m are small except closer to the windward plane. It is also observed that at the windward plane  $x_2 = 0^\circ$  the eigenvalues for the positive and negative m have the same values. This is due to the fact that at  $x_2 = 0^\circ$ , the cross-flow velocity is zero and the meanflow is two-dimensional and it does not differentiate between positive and negative m values. When one moves away from the windward plane the cross-flow velocity increases, hence the mean flow becomes three-dimensional and the eigenvalues depend on the positive or the negative direction at which the wavevector is aligned. Another observation is that there is an apparent symmetry about the eigenvalues about  $x_2 = 90^\circ$ . This can be explained from the observation that the maximum cross-flow velocity increases from zero to a peak value in the middle and decreases to zero again at the leeward plane. Hence the velocity profiles are approximately symmetrical about the middle plane and it is expected that the eigenvalues will also be symmetric. This observation becomes important when the results from 2D eigenvalue approach is interpreted in the next section.

As a prelude to later comparisons, all the eigenvalues obtained for different azimuthal mode numbers m at different azimuthal locations for the wavenumber  $\alpha = 0.074$  are plotted in the complex  $\omega$ -plane in figure 4.17. This is a representation of figures 4.15 and 4.16 in the complex plane. Some of the azimuthal locations  $x_2$  at which these eigenvalues are computed are also marked. One thing to conclude from this figure is that the eigenvalues are clustered in a confined region in the complex  $\omega$ -plane. Figure 4.18 and 4.19 depict the amplitudes of eigenfunction distribution for the streamwise velocity  $|u_1|$  and normal velocity  $|u_3|$  at different azimuthal locations for m=-30 and  $\alpha=0.07$ . It is seen that the eigenfunctions for the streamwise velocity decrease to zero at the edge of the boundary layer, however, the eigenfunction for the normal velocity decrease to zero slowly. Another observation is that the locations of the maximum amplitude move towards the edge of the boundary layer

when one moves toward the leeward plane from the windward plane. Similarly figures 4.20 to 4.22 show the 1D stability results obtained at the streamwise location  $x_1 = 0.5105m$ .

Summarizing the linear stability results of 1D eigenvalue method the following conclusions can be made.

- The boundary layer region up to  $x_1 = 0.03m$  is linearly stable and is unstable beyond that location. However, the neutral stability region is not a straight line across the cone at  $x_1 = 0.03m$  but is curved with the front of the neutral stability region falling near  $90^{\circ}$ . This is due to the effect of varying cross-flow components from windward to leeward locations.
- The most amplified temporal amplification rate occurs around  $x_2 = 90^{\circ}$  for a streamwise wavenumber  $\alpha = 0.07$  and azimuthal mode number m = -30, -40.
- The effect of cross-flow component is dominant in the middle region in azimuthal direction and this is manifested in the increase in the temporal amplification rate around  $x_2 = 90^{\circ}$  for negative m = -10 to -60 and the temporal amplification rate for positive m values.
- The unstable temporal disturbance waves with most amplification rate  $\omega_i$  travel in the negative side of  $x_2$  direction. The unstable waves propagating in the positive side of  $x_2$  become stable after  $x_2 = 90^{\circ}$ .

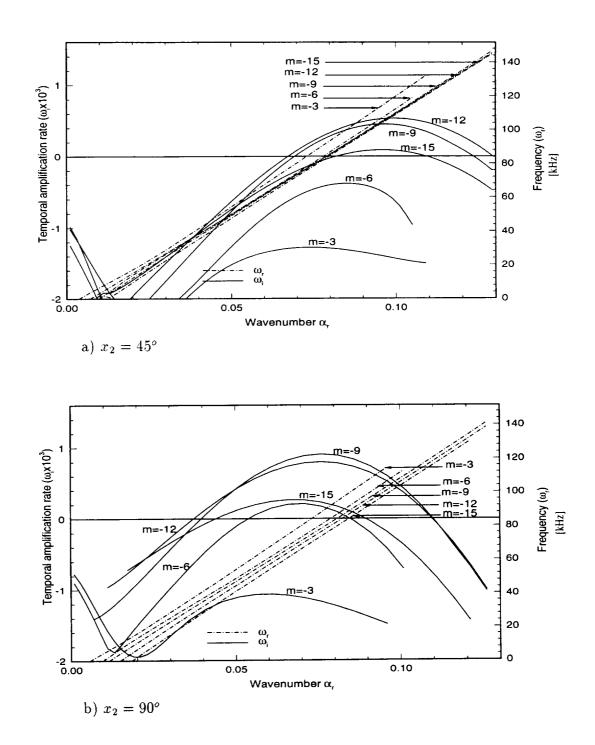


Fig. 4.2 :The variation of temporal amplification rate  $\omega_i$  and temporal frequency  $\omega_r$  with streamwise wavenumber  $\alpha$ .  $(x_1 = 0.033m)$ .

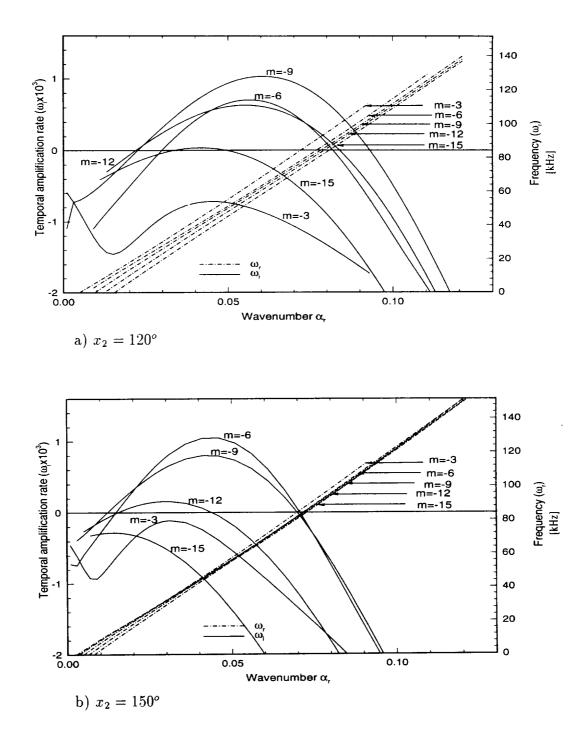


Fig. 4.3: The variation of temporal amplification rate  $\omega_i$  and temporal frequency  $\omega_r$  with streamwise wavenumber  $\alpha$ .  $(x_1 = 0.033m)$ .

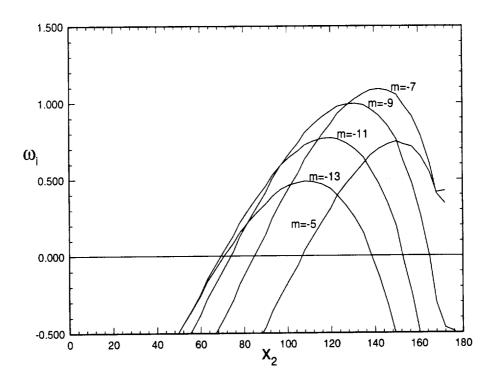


Fig. 4.4 : Distribution of temporal amplification rate  $(\omega_i)$  with  $x_2$  (streamwise location  $x_1=0.033m,~\alpha=0.05$ ).

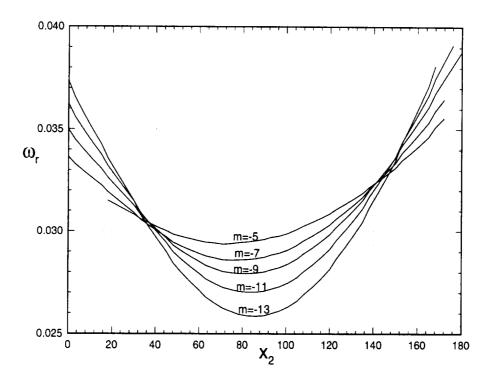


Fig. 4.5 :Distribution of temporal frequency  $(\omega_r)$  with  $x_2$  (streamwise location  $x_1=0.033m,~\alpha=0.05$ ).

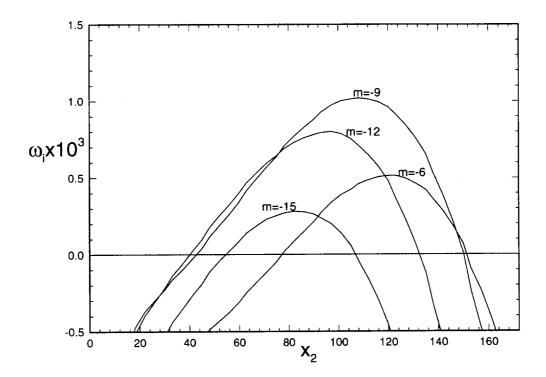


Fig. 4.6 :Distribution of temporal amplification rate  $\omega_i$  with  $x_2$ .  $(x_1 = 0.033m, \alpha = 0.07)$ .

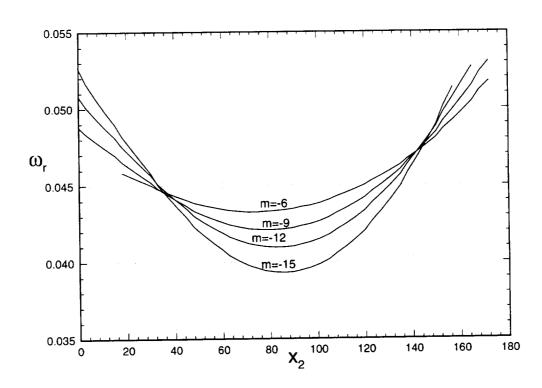


Fig. 4.7 :Distribution of temporal frequency  $(\omega_r)$  with  $x_2$  (streamwise location  $x_1=0.033m,~\alpha=0.07$ ).

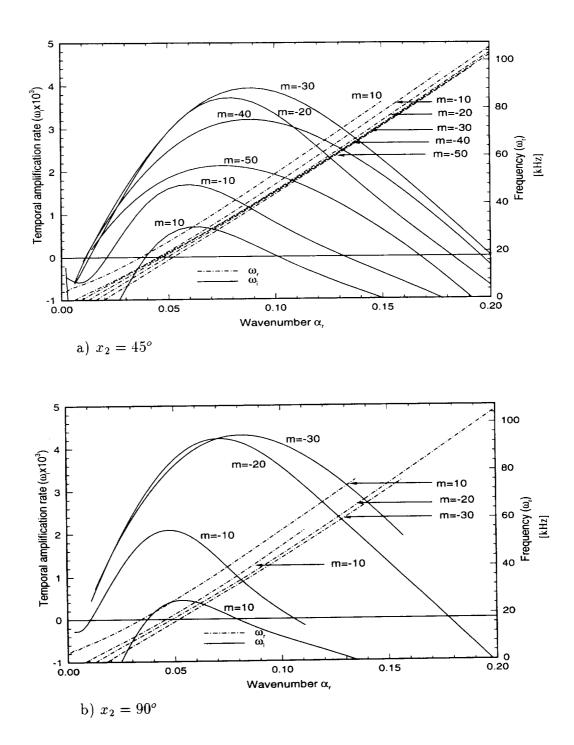
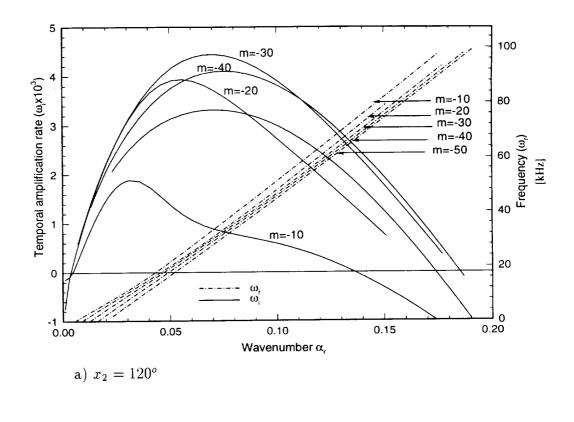


Fig. 4.8 The variation of temporal amplification rate  $\omega_i$  and temporal frequency  $\omega_r$  with streamwise wavenumber  $\alpha$ .  $(x_1 = 0.1978m)$ .



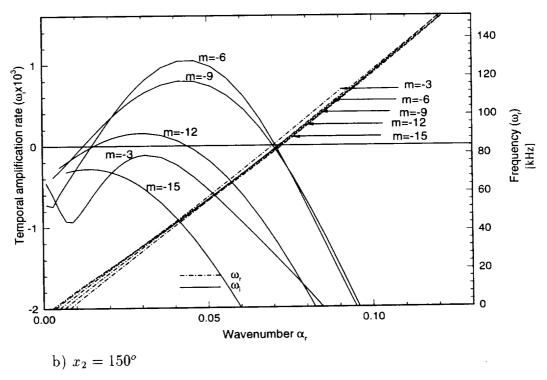


Fig. 4.9 The variation of temporal amplification rate  $\omega_i$  and temporal frequency  $\omega_r$  with streamwise wavenumber  $\alpha$ .  $(x_1 = 0.1978m)$ .

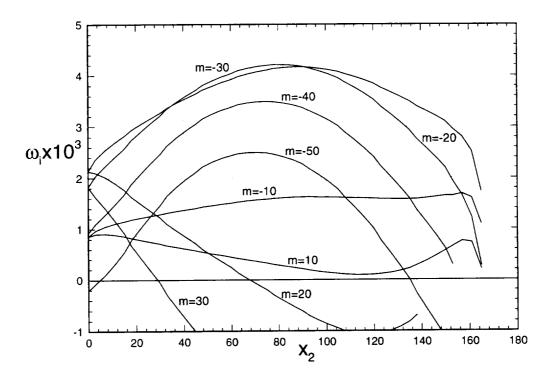


Fig. 4.10 Distribution of temporal amplification rate  $(\omega_i)$  with  $x_2$ . (streamwise location  $x_1=0.197m,~\alpha=0.07$ )

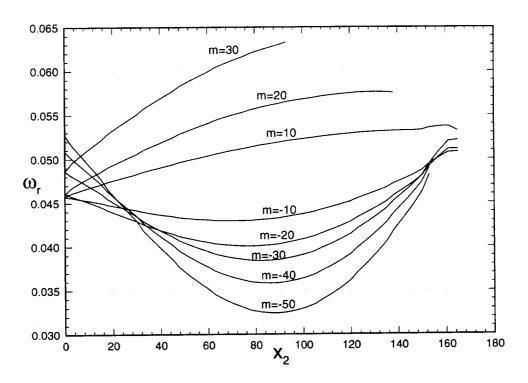


Fig. 4.11 Distribution of temporal frequency  $(\omega_r)$  with  $x_2$  (  $x_1=0.197m, \ \alpha=0.07$ ).

10

\_\_\_\_\_\_0 0.20

0.15

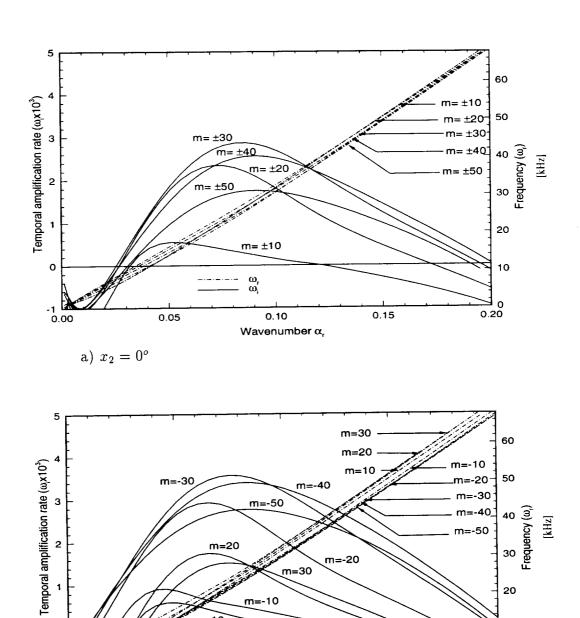


Fig. 4.12 The variation of temporal amplification rate  $\omega_i$  and temporal frequency  $\omega_r$  with streamwise wavenumber  $\alpha$ .  $(x_1 = 0.3505m)$ .

ω, ω,

0.05

0.10

Wavenumber  $\alpha_{r}$ 

1 المنا 0.00

b)  $x_2 = 20^\circ$ 

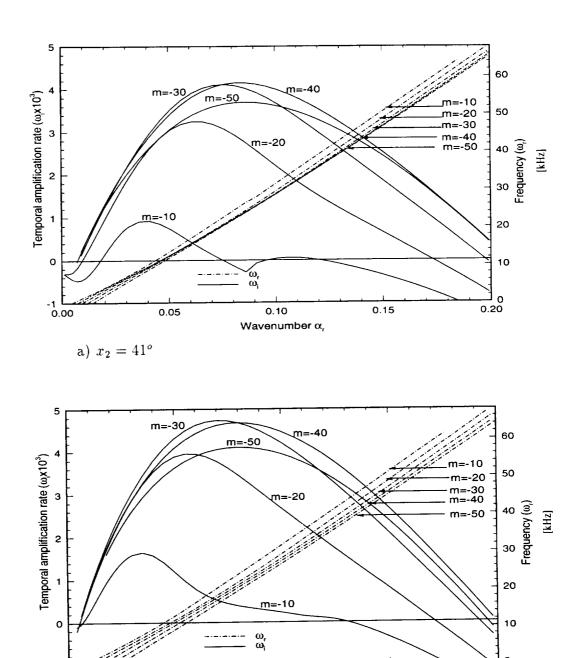


Fig. 4.13 The variation of temporal amplification rate  $\omega_i$  and temporal frequency  $\omega_r$  with streamwise wavenumber  $\alpha$ .  $(x_1 = 0.3505m)$ .

0.10

Wavenumber  $(\alpha_r)$ 

0.05

0.15

0.00

b)  $x_2 = 97^{\circ}$ 

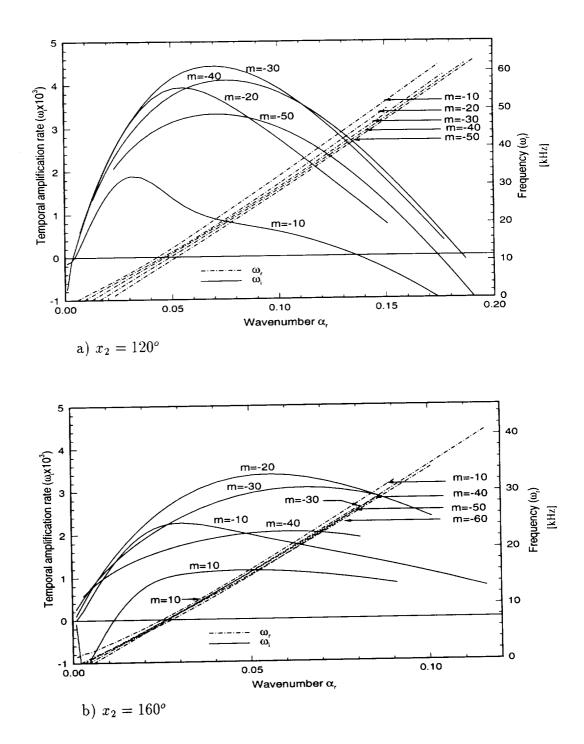


Fig. 4.14 The variation of temporal amplification rate  $\omega_i$  and temporal frequency  $\omega_r$  with streamwise wavenumber  $\alpha$ .  $(x_1 = 0.3505m)$ .

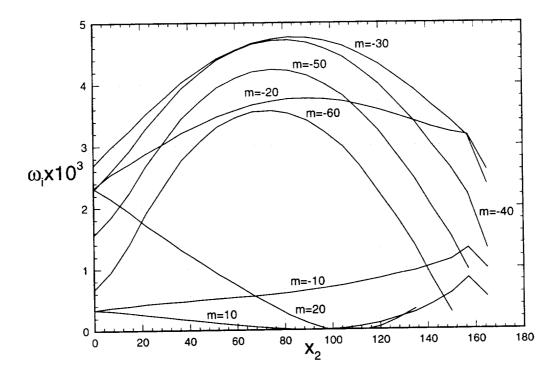


Fig. 4.15 Distribution of temporal amplification rate  $(\omega_i)$  with  $x_2$ . (streamwise location  $x_1=0.3505m,~\alpha=0.07$ ).

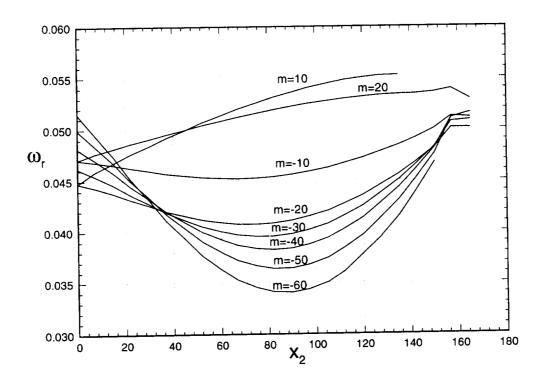


Fig. 4.16 The distribution of temporal frequency  $(\omega_r)$  with  $x_2$ . (  $x_1=0.3505m$ ,  $\alpha=0.07$ ).

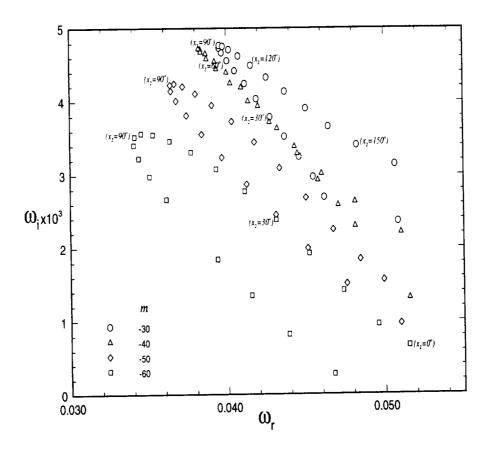


Fig. 4.17 The distribution of temporal amplification rate  $\omega_i$  with frequency  $\omega_r$ . (  $x_1=0.3505m,~\alpha=0.07$ ).

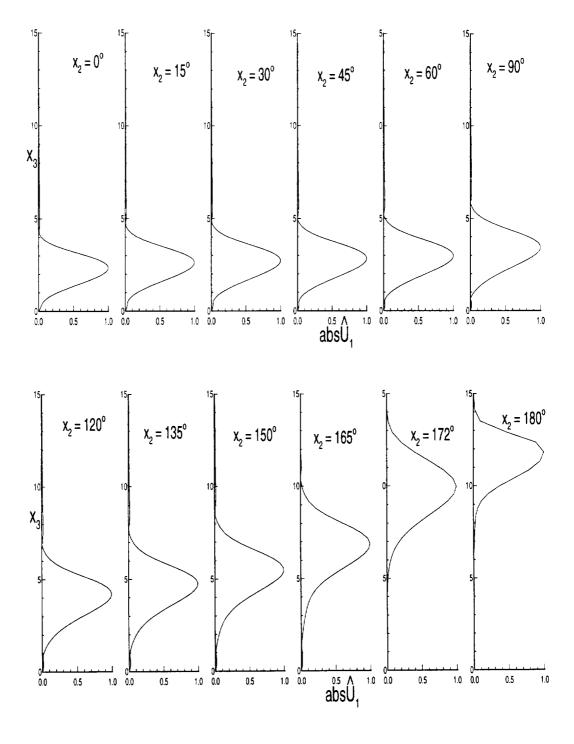
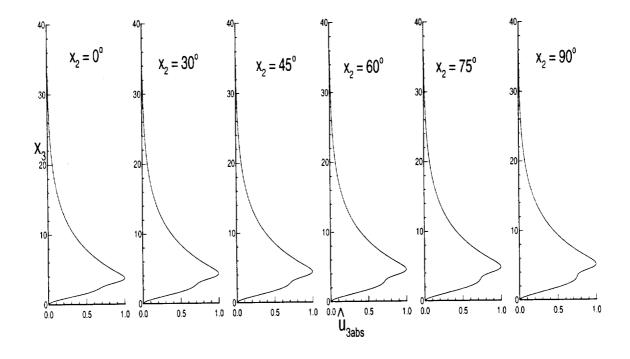


Fig. 4.18 The distribution of streamwise disturbance velocity profile  $\hat{u}_1$  along azimuthal direction.  $(x_1 = 0.3505m)$ .



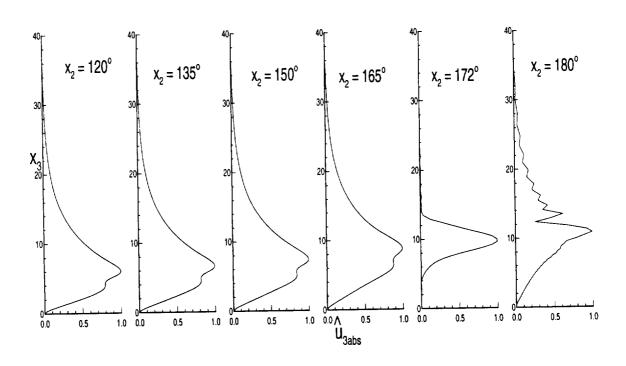


Fig. 4.19 The normal disturbance velocity profile  $\hat{u}_3$  along azimuthal direction.  $(x_1=0.3505m).$ 

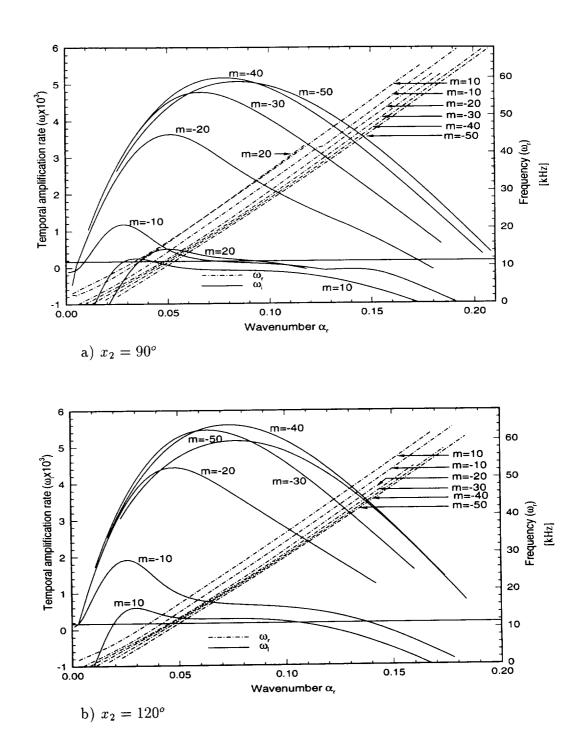


Fig. 4.20 The variation of temporal amplification rate  $\omega_i$  and temporal frequency  $\omega_r$  with streamwise wavenumber  $\alpha$ .  $(x_1 = 0.5105m)$ .

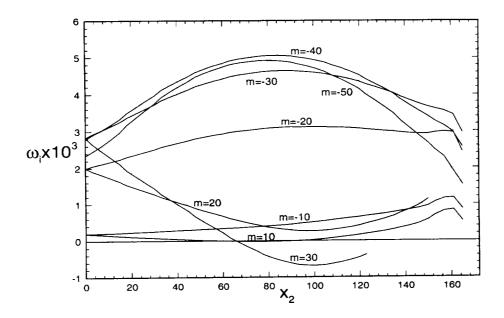


Fig. 4.21 :Distribution of temporal amplification rate  $\omega_i$  with  $x_2$ .  $(x_1=0.5105m,~\alpha=0.07).$ 

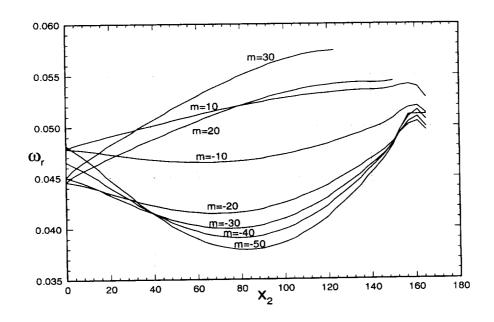


Fig. 4.22 :Distribution of temporal frequency  $(\omega_{\tau})$  with  $x_2$  (streamwise location  $x_1=0.5105m,~\alpha=0.07$ ).

## 4.2 2D Eigenvalue Problem

In this section, the results from the 2D eigenvalue computations are presented. The computations are performed at different  $x_1$  locations  $x_1 = 0.033m$ ,  $x_1 = 0.197m$ ,  $x_1 = 0.3505m$  and  $x_1 = 0.5105m$ .

As mentioned earlier, the main difficulty in the 2D eigenvalue computations is the requirement of large memory capacity. Therefore, in a typical 2D eigenvalue computations the maximum number of grid points in the wall-normal direction is limited to 49 points and the Fourier modes to a maximum of 89. However, in the regions close to the tip of the cone, it was found that most of the unstable disturbances could be captured accurately with 59 Fourier modes. This permitted the eigenvalue computations at  $x_1 = 0.033m$  be performed with 65 wall-normal points and these results are found to be consistent with that of 49 normal points and 89 Fourier modes.

Unlike in 1D stability computations where the eigenvalue spectrum for a given azimuthal mode number m consisted only of a few sparse unstable eigenvalues, it was found from the 2D eigenvalue computations that the eigenvalue spectrum showed a clustered nature of the unstable eigenvalues in the complex  $\omega$  plane. Therefore, it is necessary that prescribed initial guess for the local 2D solver be accurate, otherwise the solution might converge to some other eigenvalue. For the above mentioned typical 2D problem with 49 points in the wall-normal direction and 89 Fourier modes, the leading dimension of the matrix  $\overline{\bf A}$  of the generalized eigenvalue problem becomes (5x[89+1]x49)=22050. It takes more than 200 CPU-hours on a Sparc-Ultra-2 workstation(333MHz) and requires about 450 MW memory to compute all the eigenvalues. Therefore, the ARPACK software package employing the Implicitly Restarted Arnoldi Method (refer Chapter 2 for details) is used to obtain a specified number of eigenvalues in a region close to a given point in the complex  $\omega$  plane. When applied to the same problem of size 22050, it takes only about 2 hours to

compute 10 eigenvalues that are located close to specified region of interest, on the workstation quoted above.

The 2D stability computations performed at streamwise locations  $x_1=0.033m,\,0.197m,\,0.3505m$  and 0.5105m and the corresponding results are presented in figures 4.43 to 4.61, 4.62 to 4.76, 4.23 to 4.41 and 4.77 to 4.90 respectively. From the linear stability results of 1D eigenvalue method it was noted that the maximum temporal amplification rates in the unstable boundary layer region occurred for the range of wave numbers  $\alpha=0.06$  to 0.1. Therefore the 2D eigenvalue computations are performed for the same range of  $\alpha$ . The stability results at the above mentioned stations are found to be similar, and hence results at  $x_1=0.3505m$  are discussed in details first.

## $x_1 = 0.3505m$

Figures 4.23 to 4.41 show the results obtained at station  $x_1 = 0.3505m$  for seven different eigenvalues, both symmetric and anti-symmetric modes, for  $\alpha = 0.07$ . As it was discussed earlier, there exists large number of eigenvalues and the results are presented only for the most amplified disturbances. In the symmetric mode, the disturbances are assumed to be symmetric about the windward plane  $(x_2 = 0^\circ)$  and in the antisymmetric mode the disturbances are taken to be antisymmetric ( for detailed explanations refer Chapter 2).

Figure 4.23a shows the distribution of streamwise velocity disturbance  $\hat{u}_{1real}$  along the azimuthal direction at the wall-normal height  $x_3=0.721mm$  where it has the maximum amplitude for the wavenumber  $\alpha=0.07$  and the eigenvalue is  $\omega=(0.0386,0.00437)$ . The local Reynolds number is 1823 which is defined as

$$Re = \sqrt{\frac{U_o^* x_1}{\nu^*}} \tag{4.2}$$

It can be seen that the disturbances are symmetric about  $x_2 = 0^{\circ}$  and confined between  $80^{\circ}$  to  $140^{\circ}$  with the maximum amplitude occurring at  $120^{\circ}$ . The corre-

sponding distribution of Fourier components of the streamwise velocity disturbance  $|u_{1f}|$  with Fourier modes m is plotted in figure 4.23b. It is noted that the Fourier components  $|u_{1f}|$  falls in a bell-shape distribution with negligible magnitude until m=20 then sharply increasing to a maximum around  $m=40\sim 50$  and thereafter decaying gradually to zero around m=80. The contour plots of  $|u_1|$  and  $u_{1real}$  in the positive  $x_2x_3$  plane for the same temporal eigenvalue  $\omega$  are depicted in figure 4.24a and 4.24b. The distribution of the streamwise velocity disturbance profile and normal velocity disturbance profile are plotted in figures 4.25a and 4.25b respectively. It can be observed that the normal velocity perturbation  $\hat{u_3}$  persist until about four times the boundary layer thickness, whereas the streamwise velocity perturbation  $\hat{u_1}$  decays to zero within the boundary layer, which is equal to  $x_3=20$  in nondimensional quantity. (The variation of the boundary-layer thickness in azimuthal direction at different streamwise locations are presented in figure 3.3).

The figures 4.26 to 4.27, 4.28 to 4.29 present the results of symmetric disturbances with  $\omega = (0.04205, 0.00272)$  and  $\omega = (0.0491, 0.00264)$  which are similar to the previous results corresponding to  $\omega = (0.0386, 0.00437)$ . However, a closer examination of these results show that the clustered disturbances shift towards the leeward side with disturbance amplitude peaking at  $x_2 = 140^\circ$  and  $x_2 = 160^\circ$  for  $\omega = (0.04205, 0.00272)$  and  $\omega = (0.0491, 0.00264)$  respectively.

The 2D stability results for  $\omega = (0.04199, 0.00349)$  are shown in 4.30 to 4.32 and, in contrast to the previous results discussed, they have some different interesting features. Figure 4.30a shows the distribution of streamwise velocity disturbance  $\hat{u}_{1real}$  along the azimuthal direction at the wall-normal height  $x_3 = 0.487mm$ . An important observation is that, considering only the half azimuthal plane  $x_2 = 0^\circ$  to  $x_2 = 180^\circ$ , the disturbances are clustered in two different regions - around  $x_2 = 30^\circ$  and  $140^\circ$ . This complies with the observation of 1D results that there is an apparent symmetry of the eigenvalues about  $x_2 = 90^\circ$  caused by an approximately symmetric

distribution of cross-flow in the middle azimuthal direction. However, looking at the figure 4.30b which depicts the distribution of  $\hat{u}_{1real}$  along the azimuthal direction at  $x_3 = 0.85mm$ , it is apparent that the disturbances clustered around  $x_2 = 30^\circ$  decay to zero whereas the counterparts at  $x_2 = 140^\circ$  grow to a maximum. The corresponding distribution of Fourier components of the streamwise velocity disturbance  $|u_{1f}|$  with Fourier modes m is plotted in figure 4.31. The similar results of an eigenvalue  $\omega = (0.0451, 0.00272)$  that exhibits clustered disturbance eigenfunctions around  $x_2 = 10^\circ$  and  $150^\circ$  are shown in figures 4.33 to 4.35.

Next, the results for anti-symmetric modes are presented. The figures 4.36 to 4.37 show the results of  $\omega = (0.0437, 0.0025)$ . From figure 4.36a one can note that the disturbances are anti-symmetric and clustered around  $x_2 = -150^\circ$  and  $150^\circ$ . Also, the results for the case of  $\omega = (0.0435, 0.00315)$  are presented in figures 4.38 to 4.41. The results show that the disturbances are clustered around  $x_2 = 30^\circ$  and  $150^\circ$ , considering only the positive half of the azimuthal plane. However, the disturbances around  $x_2 = 30^\circ$  are dominant and larger than the disturbances closer to the leeward side.

An important observation about the results of symmetric and anti-symmetric disturbances is that for identical eigenvalues, there are apparently not much difference between the eigenfunction distributions of symmetric and anti-symmetric modes which are clustered around the middle of the azimuthal plane. However, eigenfunctions that peak close to the windward side exhibit a noticeable differences between symmetric and anti-symmetric modes. This observation suggest that these clustered disturbances in the middle of the azimuthal direction are not affected by the meanflow quantities (especially the azimuthal velocity components) away from them and there is not much interaction between the disturbances in the positive half and the negative half of the  $x_2x_3$  plane.

Finally, the distribution of the 2D eigenvalue spectrum need to be discussed.

Figure 4.42a shows the plot of temporal amplification rate  $\omega_i$  with frequency  $\omega_r$ for wavenumber  $\alpha = 0.07$  at  $x_1 = 0.3505m$ . The maximum amplification rate is  $\omega_i = 0.00437$  and the corresponding frequency  $\omega_\tau = 0.0386$ . The eigenfunctions for this eigenvalue are clustered in the middle of the azimuthal plane and peak around  $x_2 = 120^{\circ}$ . The  $x_2$  locations where the eigenfunctions peak are also marked on the figure. An eigenvalue marked with two angles indicates that the disturbances are clustered at two isolated  $x_2$  regions and peak at the angles quoted. In figure 4.42b, the 1D eigenvalues along with the 2D eigenvalues are plotted on complex  $\omega$  plane. A closer examination of this figure show that the most amplified temporal amplification rates of 2D stability method occur around  $x_2 = 120^{\circ}$  whereas in 1D method they fall around  $x_2 = 90^{\circ}$ . The shift in the most amplified temporal amplification rates  $\omega_i$  of the 2D eigenvalues toward the leeward side can be possibly explained as follows. The instability is determined by the degree of inflection of the meanflow profiles and the contribution of cross-flow components towards instability is maximum at  $x_2 = 90^{\circ}$ . This is clearly manifested in the maximum increase of the amplification rates of 1D eigenvalue method. However, in the case of 2D eigenvalue method which incorporates the variation of meanflow in the azimuthal direction, the meanflow is more unstable towards the leeward side and therefore shifting the most amplification rates toward the leeward side.

## $x_1 = 0.033m$

Figures 4.43 to 4.61 depict the results obtained at  $x_1 = 0.033m$  for different axial wavenumbers  $\alpha = 0.07$ , 0.08, 0.09 and 0.1. Figure 4.43 shows the distribution of eigenfunction and the Fourier components for  $\omega = (0.0391, 0.00128)$  and axial wavenumber  $\alpha = 0.07$ . The corresponding frequency is 65.8 kHz. It can be noted that the eigenfunction clustered around  $120^{\circ}$ . The maximum amplification of the eigenfunction occurs at a wall-normal height of  $x_3 = 0.255m$ , and which is about 70 % of the boundary-layer thickness ( For detailed data on distribution of boundary

layer thickness refer to figure 3.3). The contour plot for the absolute value of the streamwise perturbation velocity is shown in figure 4.44. Figure 4.43 shows the eigenfunction distribution for the axial velocity and the normal velocity at different azimuthal stations. The similar plots for an eigenvalue  $\omega = (0.0387, 0.00311)$  are given in figures 4.46 to 4.47. In figure 4.48 the plots of eigenfunction distributions are given for the frequency of f = 110.4kHz. Figures 4.49 to 4.50 show the results for the axial wavenumber  $\alpha = 0.1$  and  $\omega = (0.0656, 0.000114)$ . Unlike the previous two cases, this eigenfunctions is clustered around  $x_2 = 0^o$  for  $x_3 < 0.105mm$  and around  $x_2 = 130^{\circ}$  for  $x_3 > 0.105mm$ . Figure 4.49 shows the spectral distribution of the axial velocity at different heights with the mode number m. The distribution of streamwise velocity perturbation and temperature perturbation profiles along the azimuthal direction are depicted in figure 4.50 and 4.51 respectively. Figures 4.52 to 4.53 show the similar results for the case of anti-symmetric mode with frequency of  $107.6~\mathrm{kHz},\,\omega=(0.0639,\,0.00094)$  and  $\alpha=0.1.$  Also the figures 4.54 to 4.57 depict the similar distributions for  $\alpha = 0.08$ ,  $\omega = (0.05039, 0.00164)$  where the eigenfunction has maximum amplitude around  $x_2 = 0^\circ$  and  $140^\circ$ . Similarly figures 4.58 to 4.61 show the eigenfunction distributions and the mode shapes for anti-symmetric disturbances at  $\alpha = 0.08$ .

## $x_1 = 0.1978m$

Similarly figures 4.62 to 4.76 show the results obtained at  $x_1 = 0.1978m$  at different axial wavenumbers. Figures 4.62 to 4.63 depict the case of a symmetric mode where the eigenfunctions are clustered around 120°. In figures 4.64 to 4.67 the distribution of eigenfunctions for a symmetric mode with frequency 42.2 kHz,  $\omega = (0.0589, 0.00301)$  and wavenumber  $\alpha = 0.09$  are plotted. It can be noted that the eigenfunctions clustered around  $x_2 = 0^\circ$  and  $x_2 = 150^\circ$ . However, the amplitude of the eigenfunctions at  $x_2 = 0^\circ$  are dominant for  $x_3 = 0.287mm$  and die out gradually as one moves towards the edge of the boundary layer. Figures 4.68

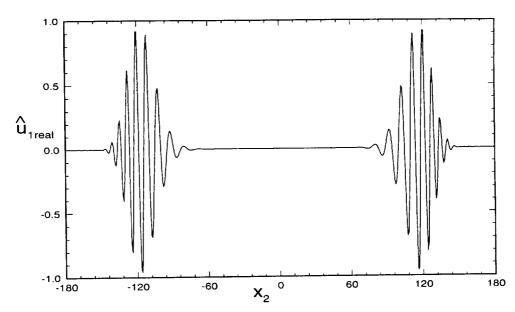
and 4.69 show the results for  $\omega = (0.0572, 0.00348)$  and figures 4.70 to 4.71, 4.72 to 4.74 and 4.75 to 4.76 show the distribution of the axial velocity fluctuations along the azimuthal direction and the spectral distributions for different  $\omega = (0.06056, 0.00328), (0.0563, 0.00131), (0.0574, 0.00115)$  and (0.0546, 0.00161). It is observed that the eigenfunctions are clustered near the windward side for these eigenvalues.  $x_1 = 0.5105m$ 

The 2D stability results at the station  $x_1 = 0.5105m$  are given in figures 4.77 to 4.90. Figures 4.77 to 4.78, 4.79 to 4.80, 4.81 to 4.82, 4.83 to 4.85. show the eigenfunctions and the spectral distribution for four different eigenvalues  $\omega = (0.0385, 0.00445), (0.0423, 0.00351), (0.0419, 0.00439), (0.0507, 0.00288) for symmetric modes. Eigenfunction corresponding to the first eigenvalue peaks around 120° and the spectral distribution has a Gausian shape as observed in other stations. The eigenfunctions corresponding to the second eigenvalue are confined to two isolated regions, one near the windward side between <math>0^{\circ}$  -  $50^{\circ}$  and the other near the leeward side between  $120^{\circ}$  -  $150^{\circ}$ . The corresponding spectral shape shows two different types of distributions at the edge of the boundary layer the shape has a Gausian distribution and near the wall a modulated shape is observed. This observation is made in other stations when the eigenfunctions are clustered in two regions. Similar observation is made for the fourth eigenvalue. Eigenfunction for the third eigenvalue peaks around  $20^{\circ}$  and the spectral distribution has a Gausian shape with a long tail at higher mode numbers.

Figure 4.86 to 4.88, 4.89 to 4.90 show the eigenfunctions and the spectral distributions for two different eigenvalues  $\omega = (0.0486, 0.0427), (0.0517, 0.00411)$  for anti-symmetric modes. The eigenfunctions are confined to two different regions, one close to the windward side and the other close to the leeward side and as it was observed earlier, the spectral distributions show two different shapes.

The results of the 2D linear stability results can be summarized as follows.

- Spectrum of 2D eigenvalues exhibits clustered nature of eigenvalues in the  $\omega$  plane.
- As expected earlier, the distributions of the disturbances along the azimuthal direction x<sub>2</sub> are clustered in confined regions. In the cases where the disturbances are clustered in two different regions in x<sub>2</sub> direction, they are nearly symmetric about x<sub>2</sub> = 90°.
- The most amplified temporal amplification rates occur around  $x_2 = 120^{\circ}$ .
- The differences between eigenfunctions of symmetric and anti-symmetric modes are pronounced when the eigenfunction distributions are confined near the windward side ( $x_2 = 0^\circ$ ). However, the differences are insignificant when the eigenfunctions are confined in the middle region.



a) The distribution velocity disturbance  $\hat{u}_{1real}$  in the azimuthal direction at wall-normal point  $x_3 = 0.721mm$ , where it has maximum amplitude.

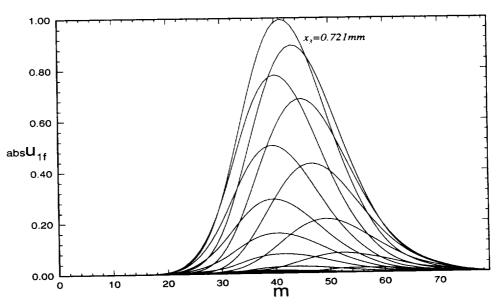
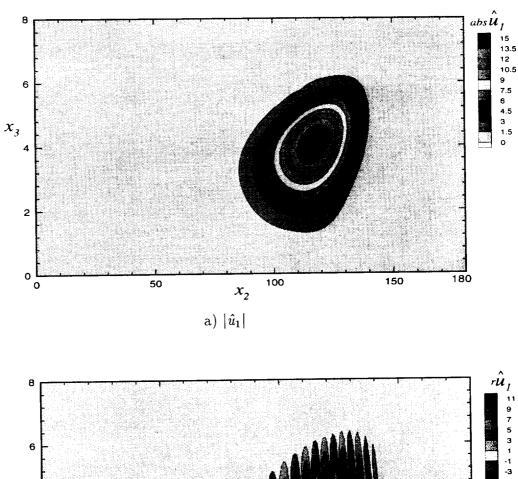
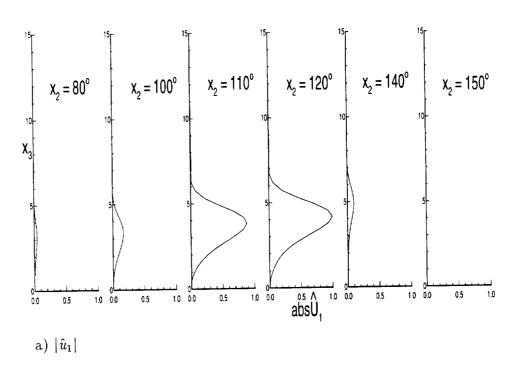


Fig. 4.23 Case 1: The distribution of eigenfunction and Fourier components for a symmetric mode with frequency f=21 kHz. (  $\omega=(0.0386,\,0.00437)$  ,  $\alpha=0.07$ . (  $x_1=0.3505m$  and Re=1823).



 $x_{3} = \begin{bmatrix} x_{3} & x_{3} & x_{4} & x_{5} & x_$ 

Fig. 4.24 Case 1: Contour plot of streamwise velocity disturbance. (frequency f=21 kHz ,  $\omega=(0.0386,\,0.00437)$  ,  $\alpha=0.07$  ,  $x_1=0.3505m$  and Re=1823 ).



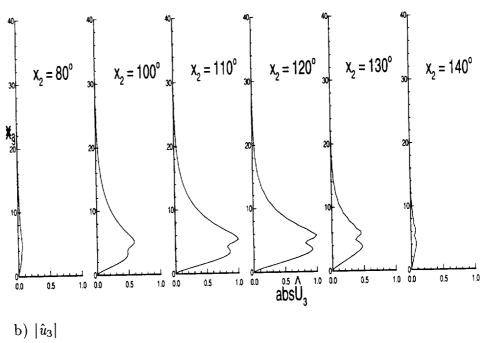
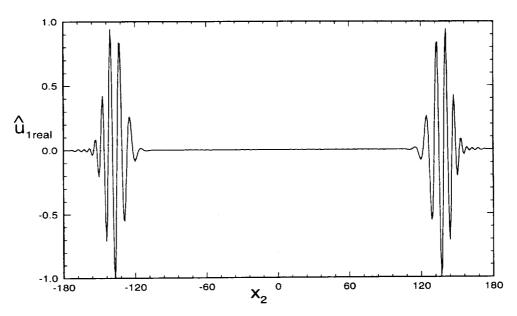
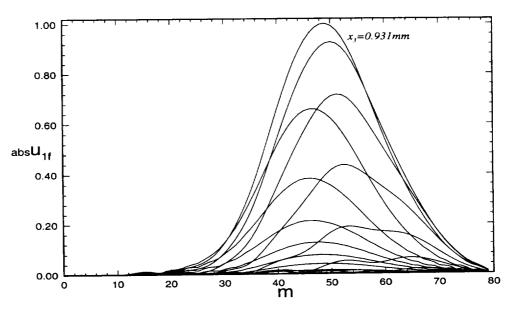


Fig. 4.25 Case 1 : The distribution of disturbance profiles along the azimuthal direction. (frequency  $f=21~\mathrm{kHz}$ ,  $\omega=(0.0386,\,0.00437)$  and  $\alpha=0.07,\,x_1=0.3505m$  and Re=1823)



a) The distribution velocity disturbance  $\hat{u}_{1real}$  in the azimuthal direction at wall-normal point  $x_3 = 0.931mm$ , where it has maximum amplitude



b) The distribution of Fourier components of streamwise velocity disturbance  $|u_{1f}|$  with Fourier modes m at different heights  $x_3$ .

Fig. 4.26 Case 2: The distribution of eigenfunction and Fourier components for a symmetric mode with frequency f=22.9 kHz. ( $\omega=(0.04205,\,0.00272)$ ),  $\alpha=0.07$ ,  $x_1=0.3505m$  and Re=1823)

1

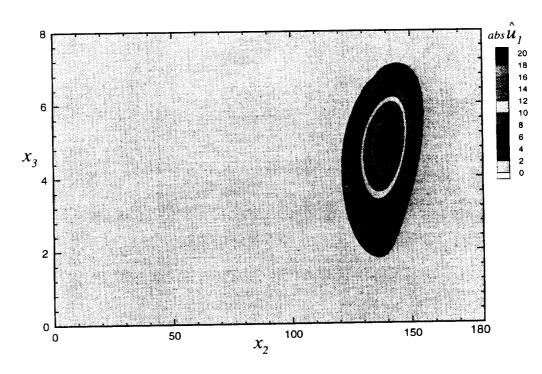
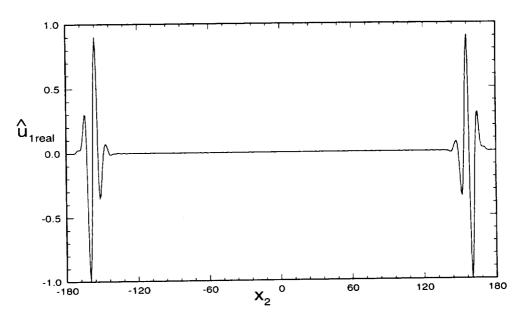


Fig. 4.27 Case 2: Contour plot of streamwise velocity disturbance  $|\hat{u}_1|$ . (frequency  $f=22.9~\mathrm{kHz}$ ,  $\omega=(0.04205,\,0.00272)$ ,  $\alpha=0.07$ ,  $x_1=0.3505m$  and Re=1823)



a) The distribution velocity disturbance  $\hat{u}_{1real}$  in the azimuthal direction at wall-normal point  $x_3 = 1.091mm$ , where it has maximum amplitude

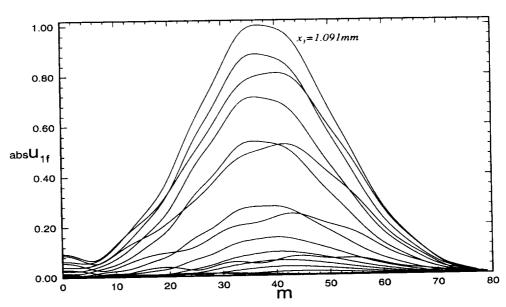


Fig. 4.28 Case 3: The distribution of eigenfunction and Fourier components for a symmetric mode with frequency f=26.8 kHz. ( $\omega=(0.0491,~0.0026)$ ),  $\alpha=0.07,$   $x_1=0.3505m$  and Re=1823)

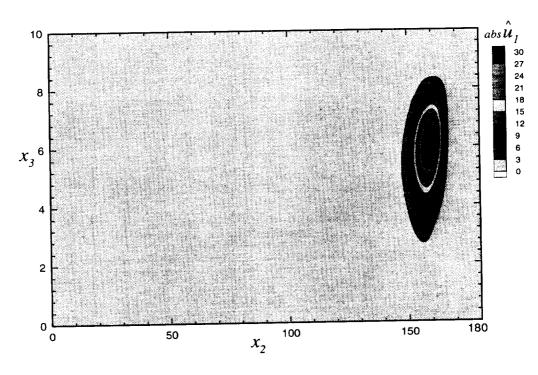
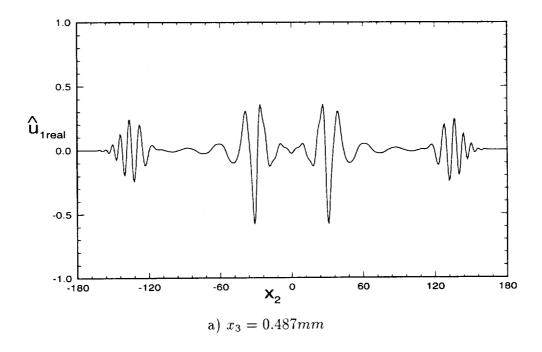


Fig. 4.29 Case 2: Contour plot of streamwise velocity disturbance  $|\hat{u}_1|$ . (frequency  $f=26.8~\mathrm{kHz}$ ,  $\omega=(0.0491,\,0.0026),\,\alpha=0.07$ ,  $x_1=0.3505m$  and Re=1823)



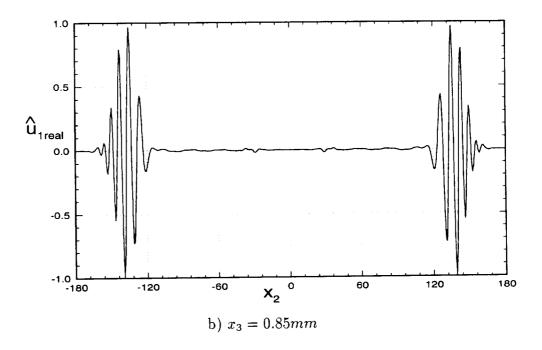


Fig. 4.30 Case 4: The distribution of eigenfunction for a symmetric mode with frequency f=22.87 kHz ,  $\omega=(0.0419,\,0.00349)$  ,  $\alpha=0.07$  ,  $x_1=0.3505m$  and Re=1823)

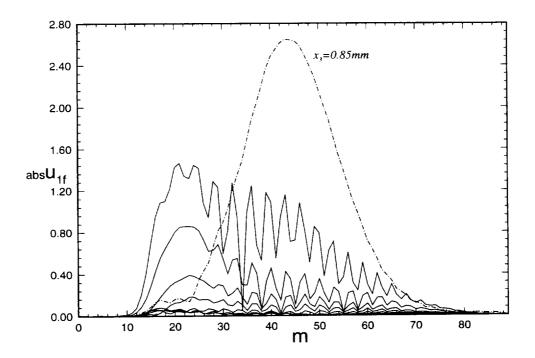
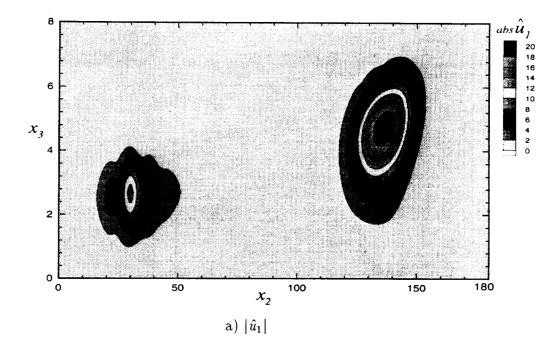


Fig. 4.31 Case 4: The distribution of Fourier components of streamwise velocity disturbance  $|u_{1f}|$  with Fourier modes m at different heights. (frequency f=22.87 kHz,  $\omega=(0.0419,\,0.00349)$ ,  $\alpha=0.07$ ,  $x_1=0.3505m$  and Re=1823).



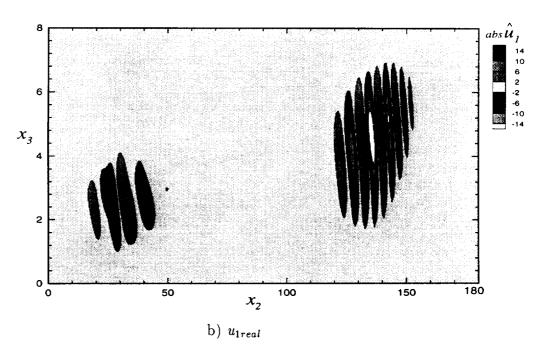
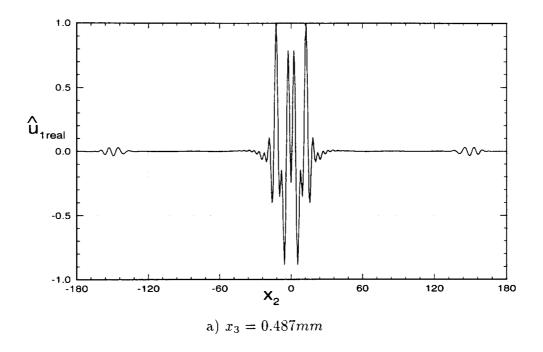


Fig. 4.32 Case 4: Contour plot of streamwise velocity disturbance. (frequency  $f=22.87~\rm{kHz}$  ,  $~\omega=(0.0419,~0.00349)$  ,  $\alpha=0.07$  ,  $x_1=0.3505m$  and ~Re=1823 )



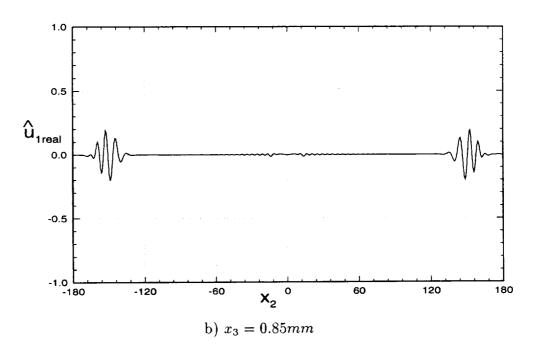


Fig. 4.33 Case 5: The distribution of eigenfunction for a symmetric mode with frequency f=24.6 kHz ,  $\omega=(0.0451,\,0.00272)$  ,  $\alpha=0.07,\,x_1=0.3505m$  and Re=1823)

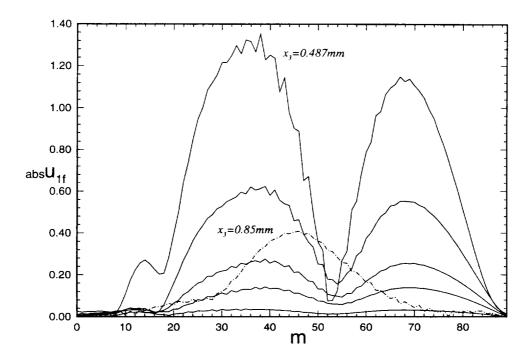
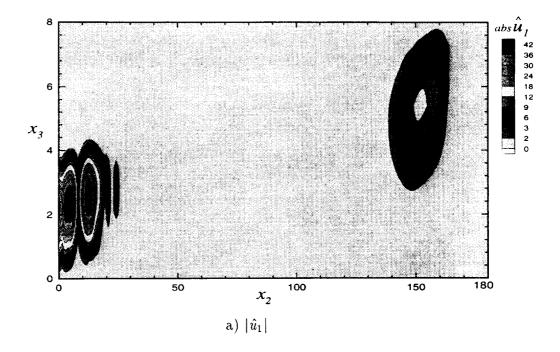


Fig. 4.34 Case 5: The distribution of Fourier components of streamwise velocity disturbance  $|u_{1f}|$  with Fourier modes m at different heights. (frequency f=24.6 kHz,  $\omega=(0.0451,\,0.00272)$ ,  $\alpha=0.07$ ,  $x_1=0.3505m$  and Re=1823).



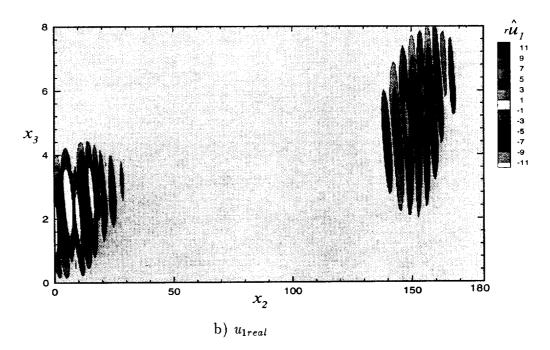
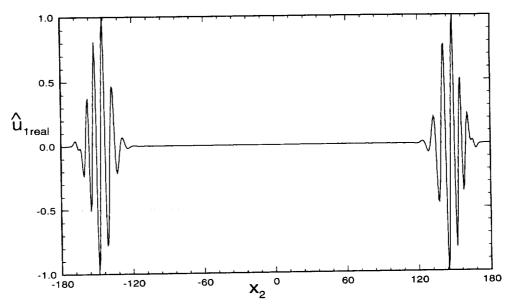


Fig. 4.35 Case 5: Contour plot of streamwise velocity disturbance. (frequency  $f=24.6~\mathrm{kHz}$  ,  $~\omega=(0.0451,~0.00272)$  ,  $\alpha=0.07$  ,  $x_1=0.3505m$  and Re=1823 ).



a) The distribution velocity disturbance  $\hat{u}_{1real}$  in the azimuthal direction at wall-normal point  $x_3 = 0.931mm$ , where it has maximum amplitude

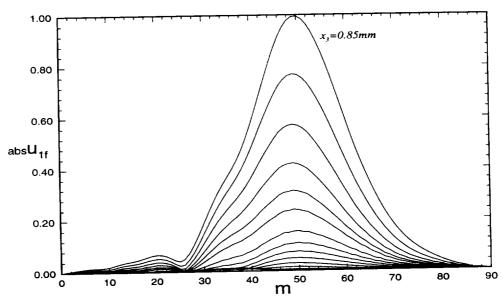


Fig. 4.36 Case 6: The distribution of eigenfunction and Fourier components for an anti-symmetric mode with frequency  $f=23.81~\mathrm{kHz}$ ,  $\omega=(0.0437,\,0.0025)$ ,  $\alpha=0.07,\,x_1=0.3505m$  and Re=1823)

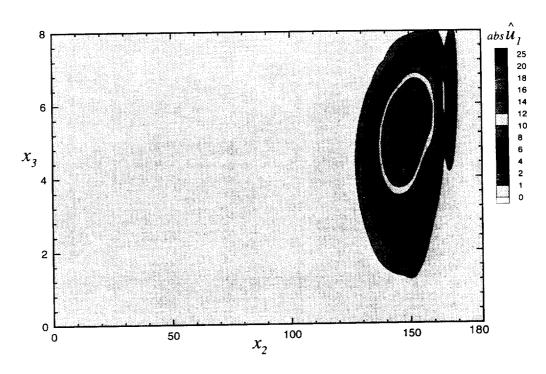


Fig. 4.37 Case 6: Contour plot of streamwise velocity disturbance  $|\hat{u}_1|$ . (frequency  $f=23.81~\mathrm{kHz}$ ,  $\omega=(0.0437,\,0.0025)$ ,  $\alpha=0.07$ ,  $x_1=0.3505m$  and Re=1823)

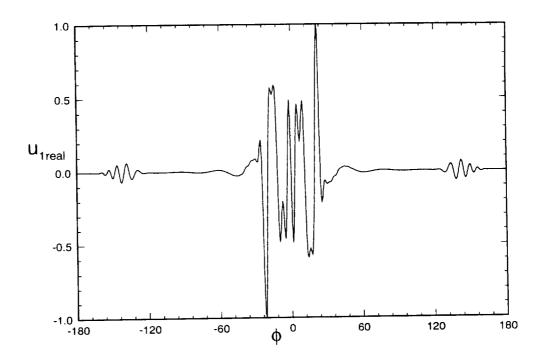
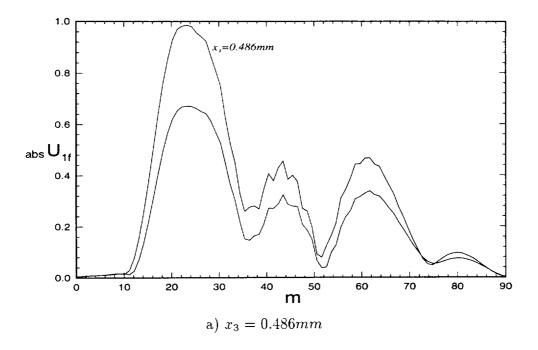


Fig. 4.38 Case 7: The distribution of eigenfunction for a symmetric mode with frequency f=23.71 kHz. ( $\omega=(0.0434,\,0.00316)$ ,  $\alpha=0.07,\,x_1=0.3505m$  and Re=1823)



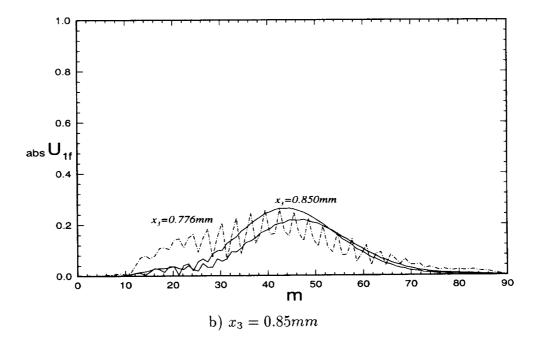
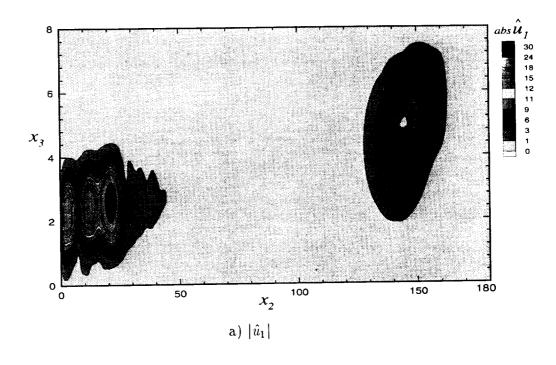


Fig. 4.39 Case 7: The distribution of Fourier components of streamwise velocity disturbance  $|u_{1f}|$  with Fourier modes m at different heights. (frequency f=23.71 kHz ,  $\omega=(0.0434,\,0.00316)$  ,  $\alpha=0.07$  ,  $x_1=0.3505m$  and Re=1823)



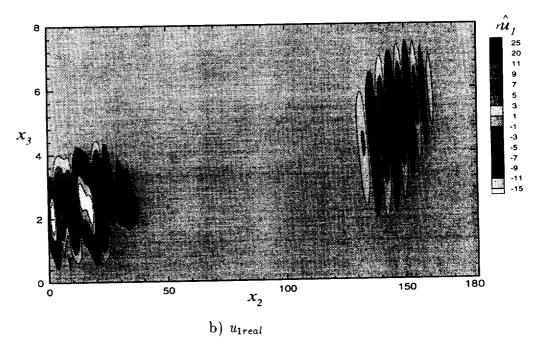


Fig. 4.40 Case 7: Contour plot of streamwise velocity disturbance. (frequency  $f=23.71~\rm{kHz}$  ,  $~\omega=(0.0434,~0.00316)$  ,  $\alpha=0.07$  ,  $x_1=0.3505m$  and ~Re=1823 )

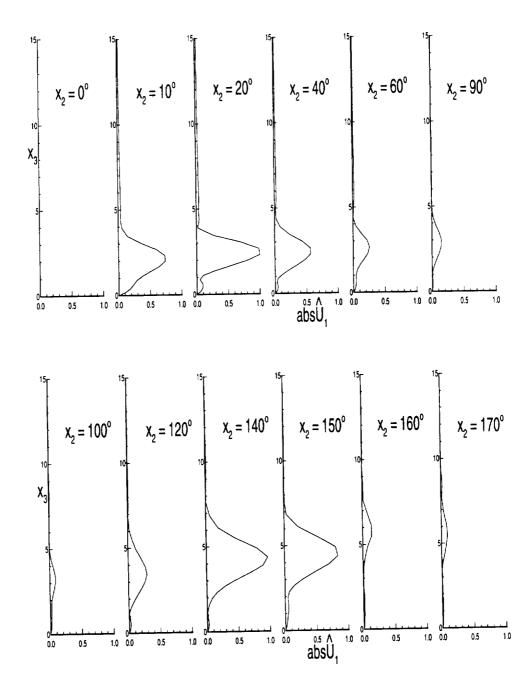
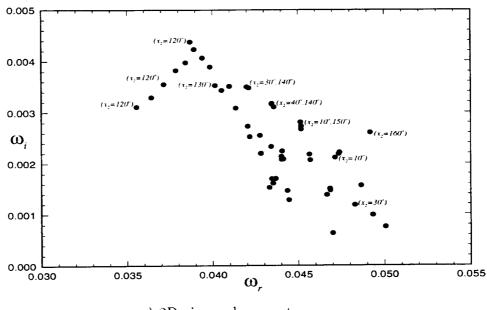


Fig. 4.41 Case 7: The distribution of streamwise velocity perturbation profiles along the azimuthal direction. (frequency f=23.71 kHz ,  $\omega=(0.0434,\,0.00316)$  ,  $\alpha=0.07,\,x_1=0.3505m$  and Re=1823)



a) 2D eigenvalue spectrum

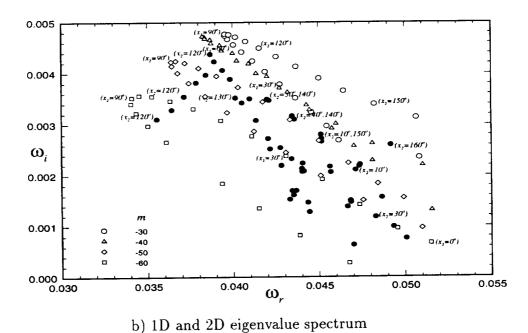
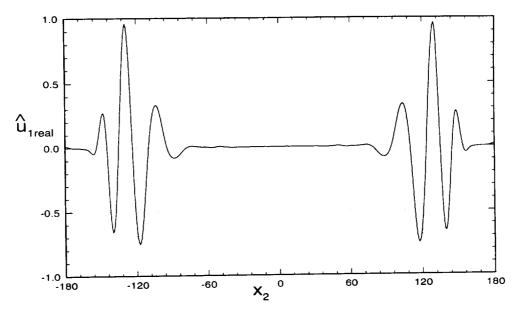


Fig. 4.42 Case 7: Unstable eigenvalue spectrums of a) 2D eigenvalue method and b) 1D (hollow symbols) and 2D (solid symbols) eigenvalue methods. (  $\alpha=0.07$ ,  $x_1=0.3505m$  and Re=1823)



a) The distribution velocity disturbance  $\hat{u}_{1real}$  in the azimuthal direction at wall-normal point  $x_3 = 0.255mm$ , where it has maximum amplitude

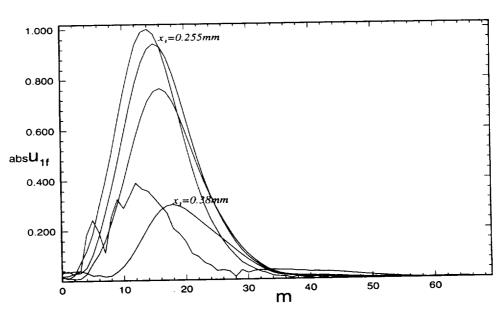


Fig. 4.43 Case 1: The distribution of eigenfunction and Fourier components for a symmetric mode with frequency f=65.8 kHz . ( $\omega=(0.0391,\,0.00128)$  and  $\alpha=0.07$ ,  $x_1=0.033m,\;Re=531$ ).

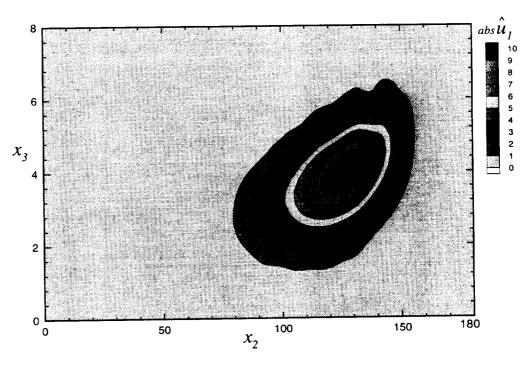
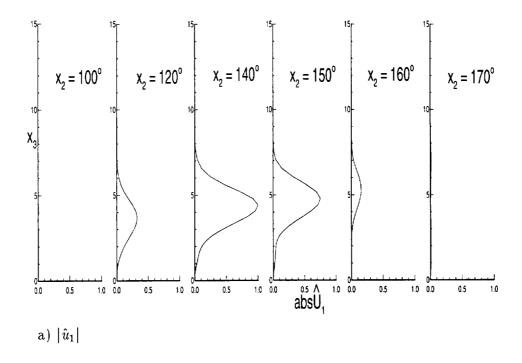


Fig. 4.44 Case 1: Contour plot of streamwise velocity disturbance  $|\hat{u}_1|$ . (frequency  $f=65.8~\mathrm{kHz}$ ,  $\omega=(0.0391,\,0.00128)$ ,  $\alpha=0.07$ ,  $x_1=0.033m$  and Re=531)



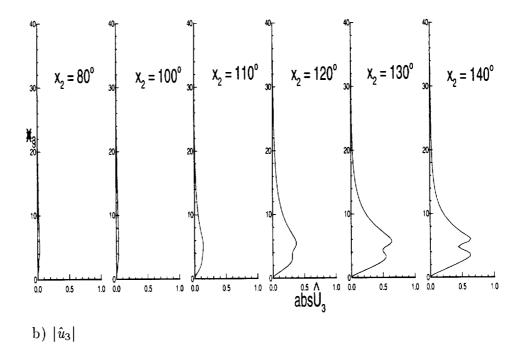
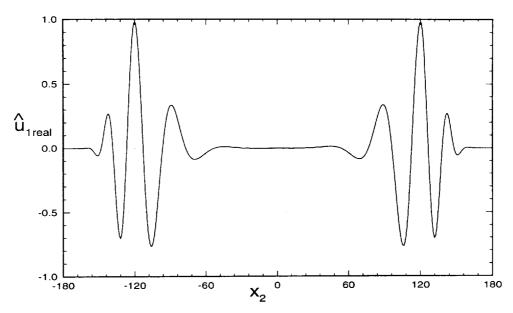


Fig. 4.45 Case 1 : The distribution of disturbance profiles along the azimuthal direction. (frequency f=65.8 kHz ,  $\omega=(0.0391,\,0.00128)$  ,  $\alpha=0.07,\,x_1=0.033m$  and Re=531)



a) The distribution velocity disturbance  $\hat{u}_{1real}$  in the azimuthal direction at wall-normal point  $x_3 = 0.215mm$ , where it has maximum amplitude

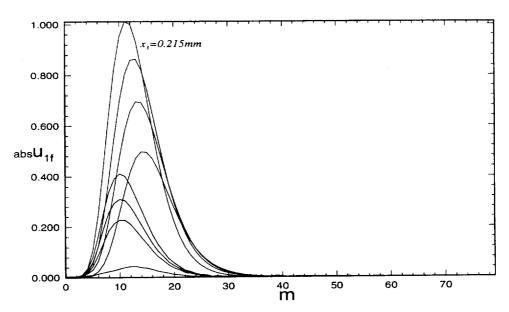


Fig. 4.46 Case 2: The distribution of eigenfunction and Fourier components for a+symmetric mode with frequency f=65.1 kHz . (  $\omega=(0.0388,\,0.00311)$  and  $\alpha=0.07$ ,  $x_1=0.033m,\;Re=531)$ 

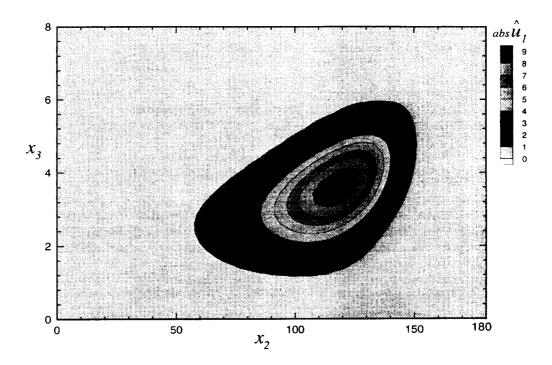
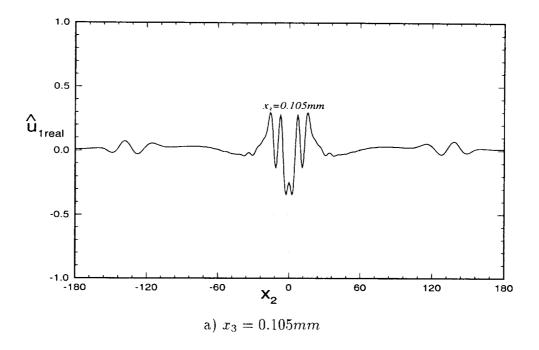


Fig. 4.47 Case 2: Contour plot of streamwise velocity disturbance  $|\hat{u}_1|$ . (frequency  $f=65.1~\mathrm{kHz}$ ,  $\omega=(0.0388,\,0.00311)$ ,  $\alpha=0.07$ ,  $x_1=0.033m$  and Re=531)



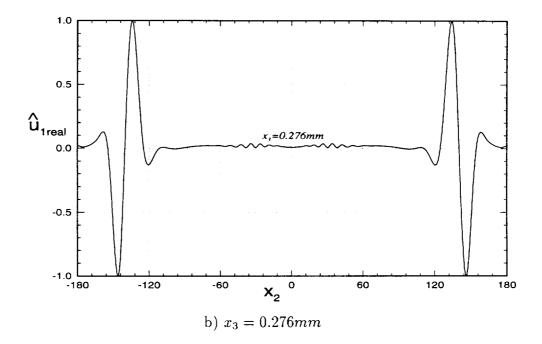


Fig. 4.48 Case 3: The distribution of eigenfunction for a symmetric mode with frequency f=110.4 kHz. (  $\omega=(0.0656,\,0.000114)$  ,  $\alpha=0.1$  ,  $x_1=0.033m$  and Re=531)

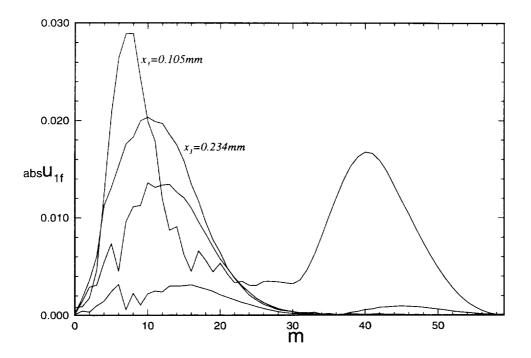


Fig. 4.49 Case 3: The distribution of Fourier components of streamwise velocity disturbance  $|u_{1f}|$  with Fourier modes m at different heights. (frequency f=110.4 kHz,  $\omega=(0.0656,\,0.000114)$ ,  $\alpha=0.1$ ,  $x_1=0.033m$  and Re=531)

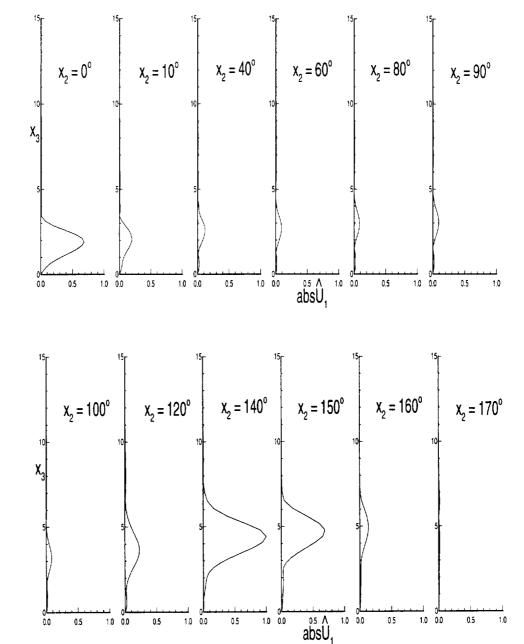
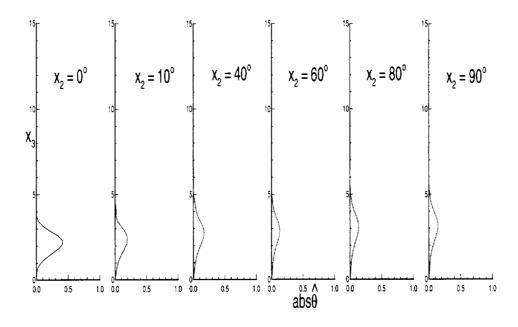


Fig. 4.50 Case 3: The distribution of streamwise velocity perturbation profiles along the azimuthal direction. (frequency  $f=110.4~\mathrm{kHz}$ ,  $\omega=(0.0656,\,0.000114)$ ,  $\alpha=0.1$ ,  $x_1=0.033m$  and Re=531)



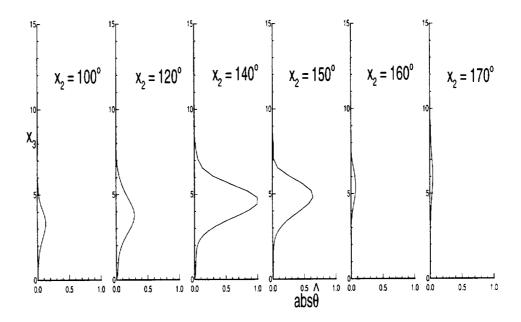
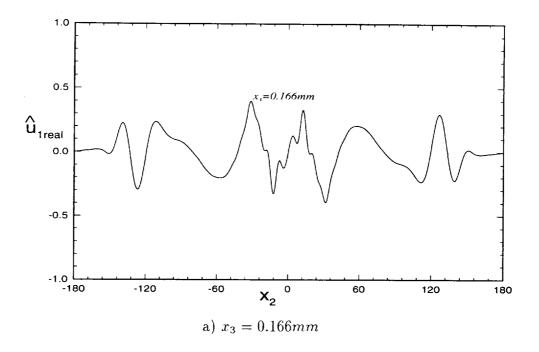


Fig. 4.51 Case 3: The distribution of temperature perturbation profiles along the azimuthal direction. (frequency f=110.4 kHz ,  $\omega=(0.0656,\,0.000114)$  ,  $\alpha=0.1$ ,  $x_1=0.033m$  and Re=531)



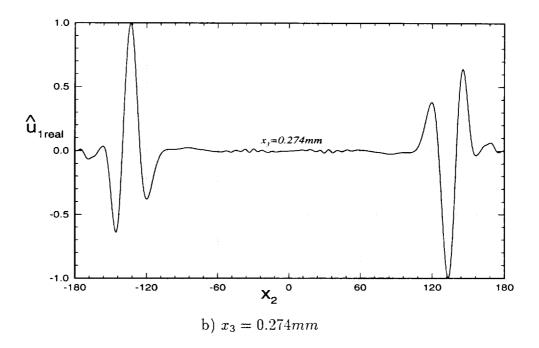


Fig. 4.52 Case 4: The distribution of eigenfunction for a symmetric mode with frequency f=107.6 kHz. (  $\omega=(0.0639,\,0.00094)$  ,  $\alpha=0.1,\,x_1=0.033m,$  and Re=531)

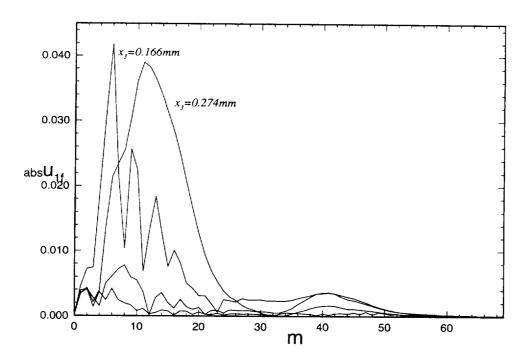
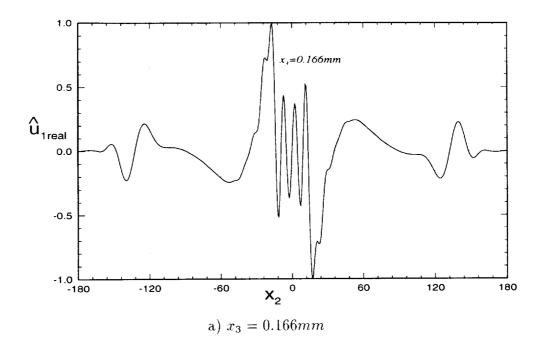


Fig. 4.53 Case 4: The distribution of Fourier components of streamwise velocity disturbance  $|u_{1f}|$  with Fourier modes m at different heights. (frequency f=107.6 kHz ,  $\omega=(0.0639,\,0.00094)$  ,  $\alpha=0.1$  ,  $x_1=0.033m$  and Re=531)



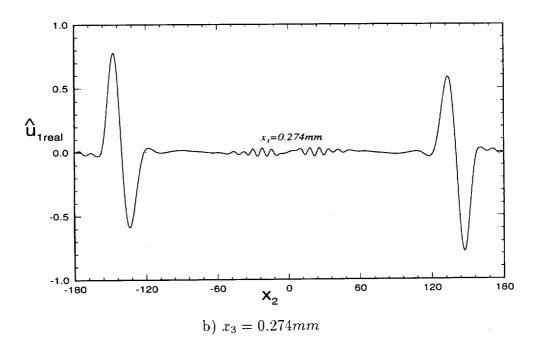


Fig. 4.54 Case 5: The distribution of eigenfunction for a symmetric mode with frequency f=84.8 kHz. (  $\omega=(0.05039,\,0.00164)$  ,  $\alpha=0.08$ . (  $x_1=0.033m$ , and Re=531)

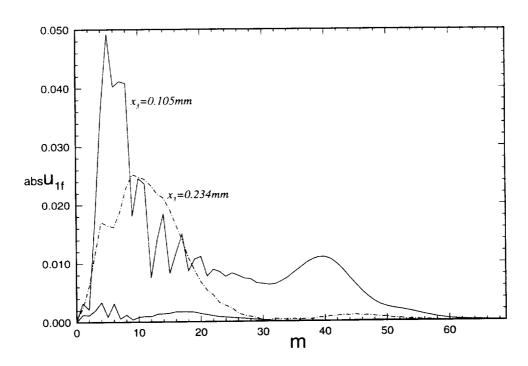


Fig. 4.55 Case 5: The distribution of Fourier components of streamwise velocity disturbance  $|u_{1f}|$  with Fourier modes m at different heights. (frequency f=84.8 kHz ,  $\omega=(0.05039,\,0.00164)$  ,  $\alpha=0.08$  ,  $x_1=0.033m$  and Re=531)

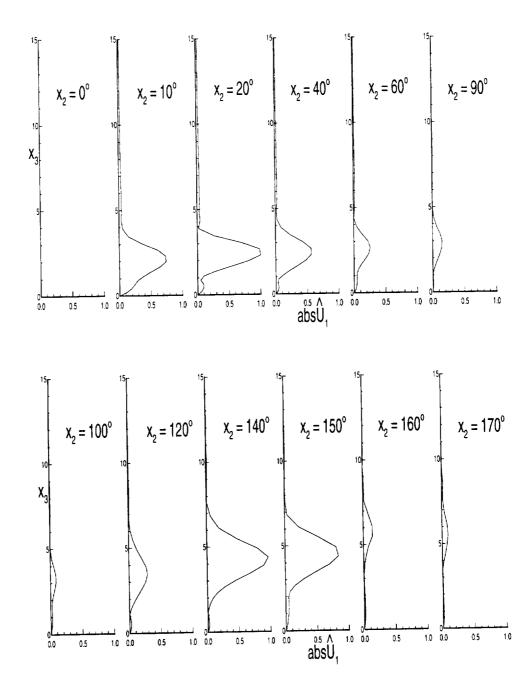


Fig. 4.56 Case 5: The distribution of streamwise velocity perturbation profiles along the azimuthal direction. (frequency  $f=84.8~\mathrm{kHz}$ ,  $\omega=(0.05039,\,0.00164)$ ,  $\alpha=0.08,\,x_1=0.3505m$  and Re=531)

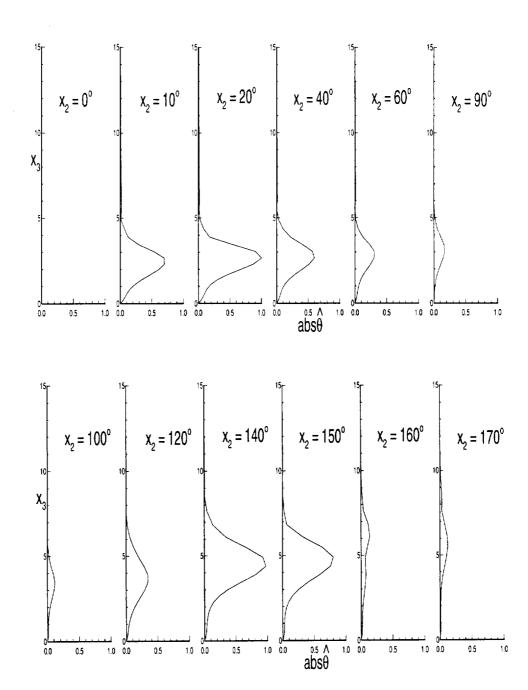
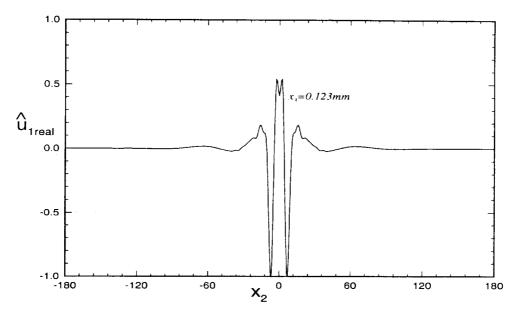


Fig. 4.57 Case 5: The distribution of temperature perturbation profiles along the azimuthal direction. (frequency f=84.8 kHz ,  $\omega=(0.05039,\ 0.00164)$  ,  $\alpha=0.08$ .  $x_1=0.3505m$  and Re=531)



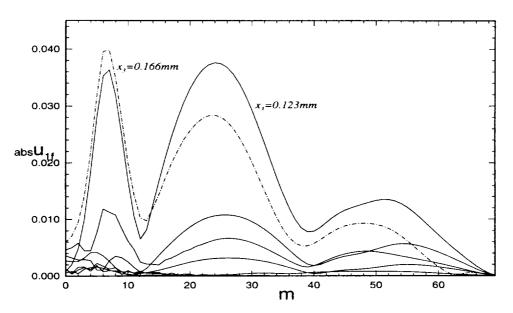
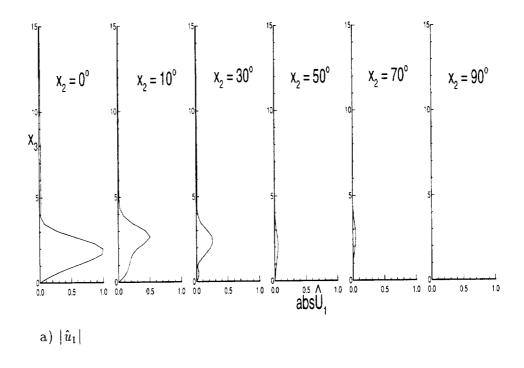


Fig. 4.58 Case 6: The distribution of eigenfunction and Fourier components for a symmetric mode with frequency f=89.7 kHz. (  $\omega=(0.0532,~0.0023)$  ,  $\alpha=0.08$  ,  $x_1=0.033m$  and Re=531)



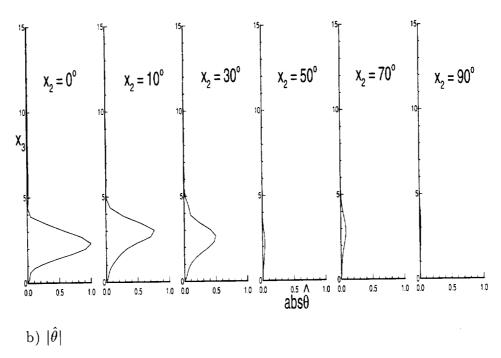
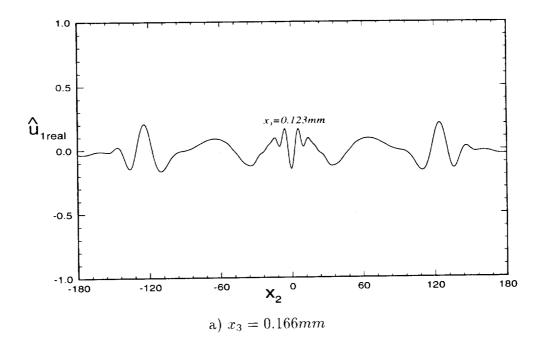


Fig. 4.59 Case 6: The distribution of disturbance profiles along the azimuthal direction. (frequency  $f=89.7~\mathrm{kHz}$ ,  $\omega=(0.0532,\,0.0023)$  and  $\alpha=0.08,\,x_1=0.033m$  and Re=531)



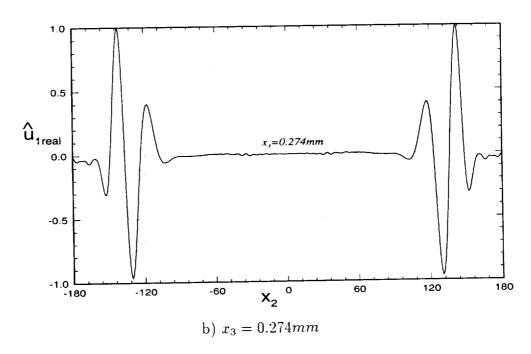


Fig. 4.60 Case 7: The distribution of eigenfunction for a symmetric mode with frequency f=80.5 kHz. (  $\omega=(0.04785,\,0.00137)$  ,  $\alpha=0.08,\,x_1=0.033m$  and Re=531)

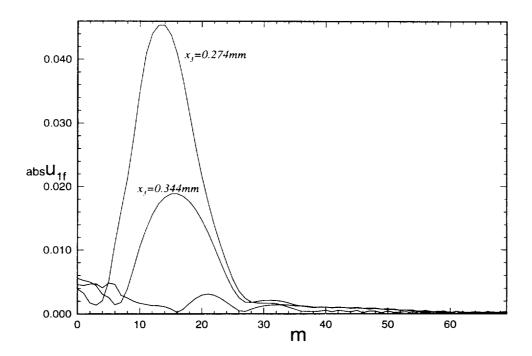
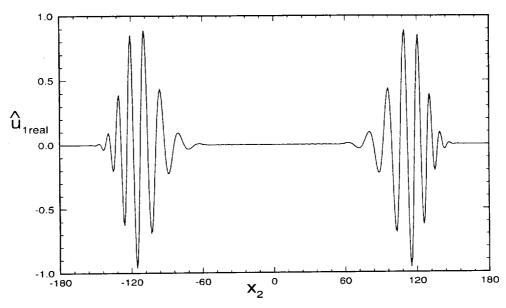
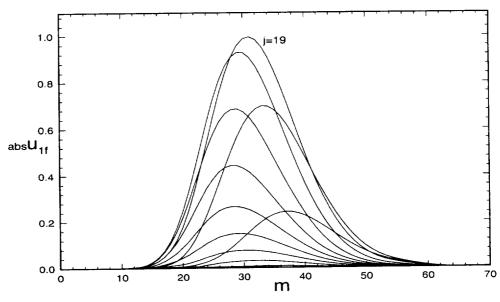


Fig. 4.61 Case 7: The distribution of Fourier components of streamwise velocity disturbance  $|u_{1f}|$  with Fourier modes m at different heights. (frequency f=80.5 kHz ,  $\omega=(0.04785,\,0.00137)$  ,  $\alpha=0.08$  ,  $x_1=0.033m$  and Re=531)





b) The distribution of Fourier components of streamwise velocity disturbance  $|u_{1f}|$  with Fourier modes m at different heights  $x_3$ .

Fig. 4.62 Case 1: The distribution of eigenfunction and Fourier components for a symmetric mode with frequency  $f=27.7~\mathrm{kHz}$ ,  $\omega=(0.0387,0.00427)$ ,  $\alpha=0.07$ ,  $x_1=0.1978m$  and Re=1350)

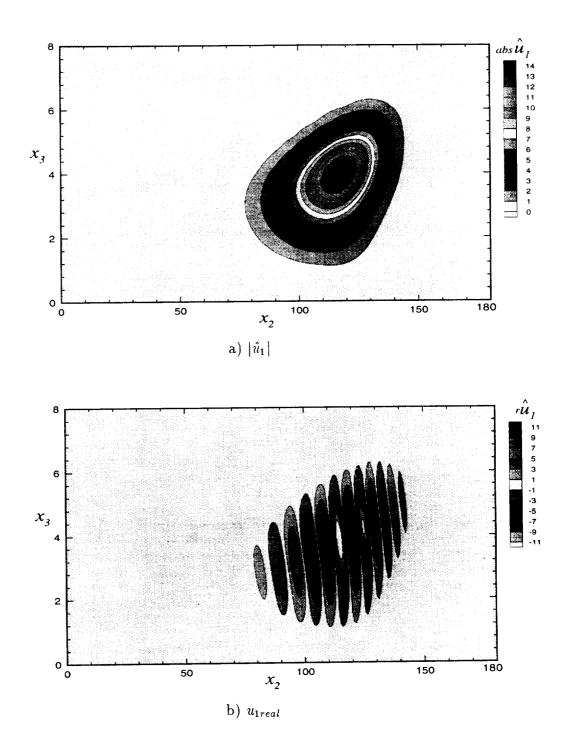
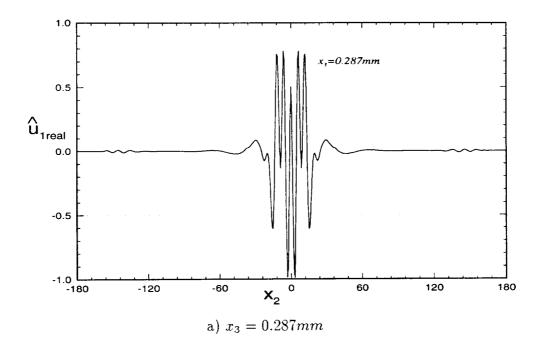


Fig. 4.63 Case 1: Contour plot of streamwise velocity disturbance. ( frequency  $f=27.7~\rm kHz$  ,  $\,\omega=(0.0589,0.00301)$  ,  $\alpha=0.07$  ,  $x_1=0.1978m$  and  $\,Re=1350$  )



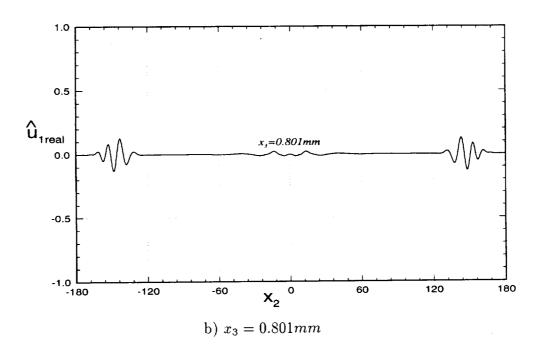


Fig. 4.64 Case 2: The distribution of eigenfunction for a symmetric mode with frequency f=42.2 kHz. (  $\omega=(0.0589~,0.00301)$  ,  $\alpha=0.09,~x_1=0.1978m$  and Re=1350)

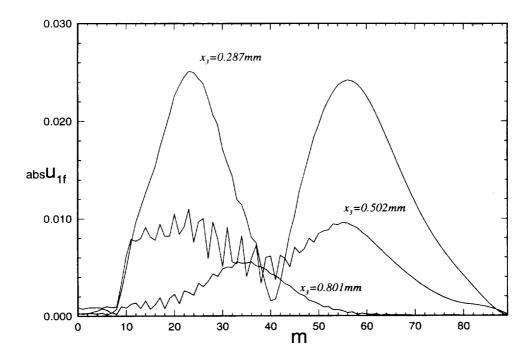


Fig. 4.65 Case 2: The distribution of Fourier components of streamwise velocity disturbance  $|u_{1f}|$  with Fourier modes m. (frequency f=42.2 kHz ,  $\omega=(0.0589,0.00301)$  ,  $\alpha=0.09$  ,  $x_1=0.1978m$  and Re=1350)

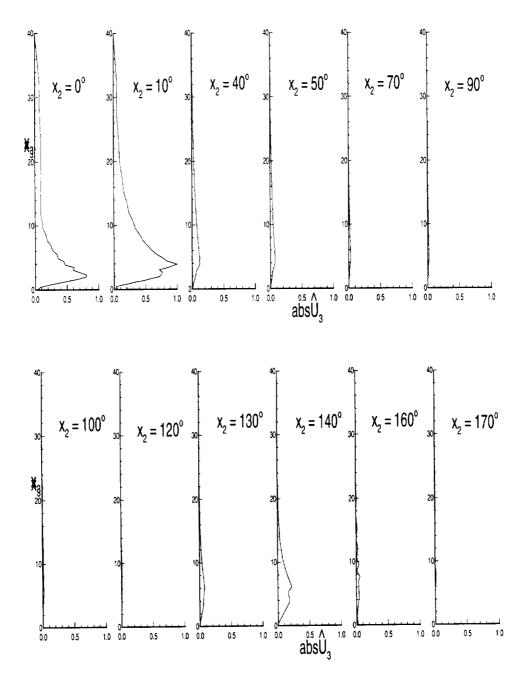


Fig. 4.66 Case 2: The distribution of streamwise velocity perturbation profiles along the azimuthal direction. (frequency  $f=42.2~\mathrm{kHz}$ ,  $\omega=(0.0589,\,0.00301)$ ,  $\alpha=0.09,\,x_1=0.1978m$  and Re=1350)

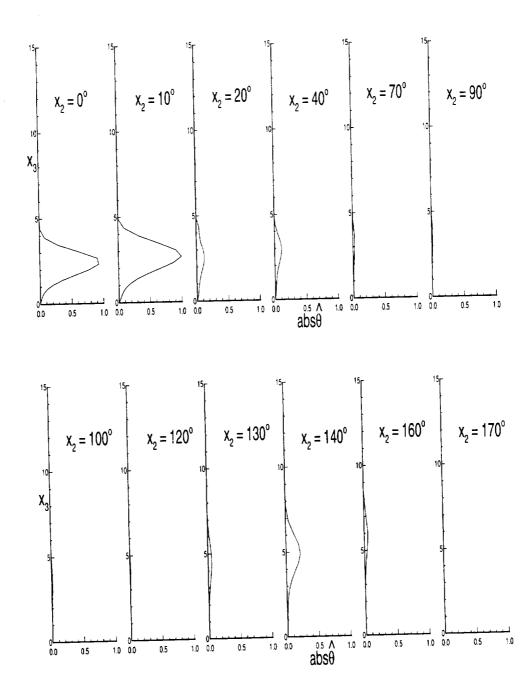
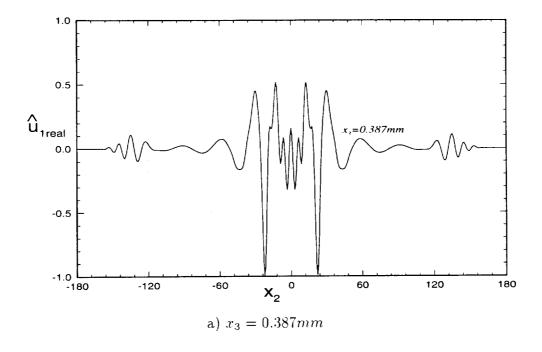


Fig. 4.67 Case 2: The distribution of temperature perturbation profiles along the azimuthal direction. (  $\omega = (0.0589, 0.00301)$  and  $\alpha = 0.09, x_1 = 0.1978m, Re = 1350)$ 



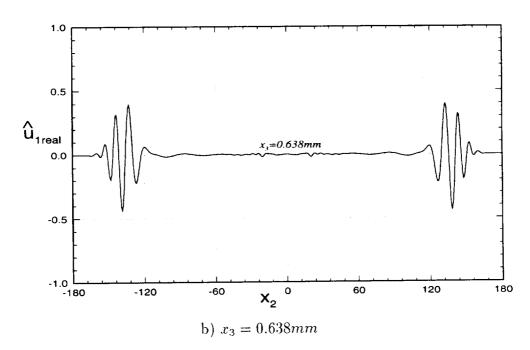


Fig. 4.68 Case 3: The distribution of eigenfunction for a symmetric mode with frequency f=41.05 kHz ,  $\omega=(0.0572,\,0.00348)$  ,  $\alpha=0.09$  ,  $x_1=0.1978m$ , and Re=1350)

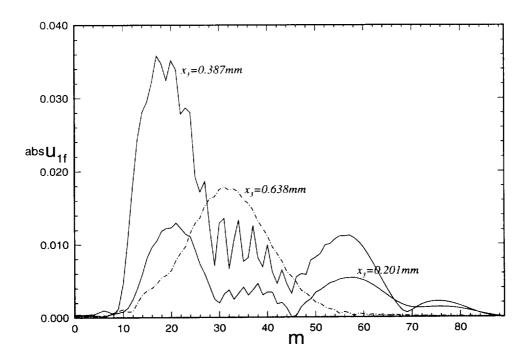
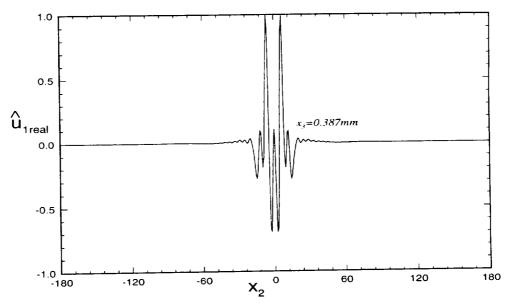


Fig. 4.69 Case 3: The distribution of Fourier components of streamwise velocity disturbance  $|u_{1f}|$  with Fourier modes m. (frequency f=41.05 kHz ,  $\omega=(0.0572,0.00348)$  ,  $\alpha=0.09$  ,  $x_1=0.1978m$  and Re=1350)



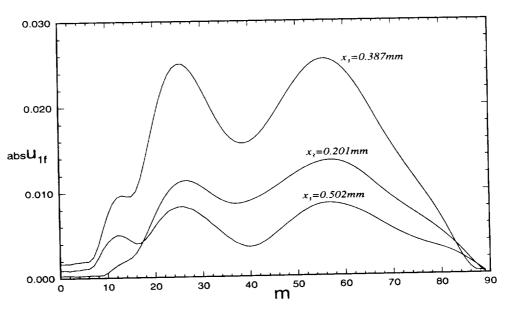
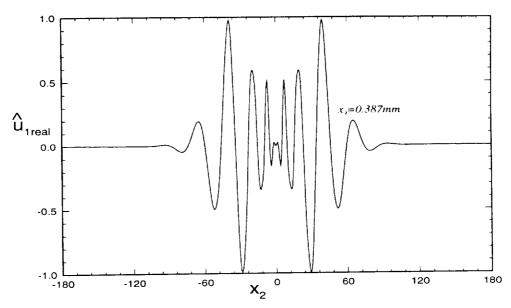


Fig. 4.70 Case 4: The distribution of eigenfunction and Fourier components for a symmetric mode with frequency f=43.36 kHz ,  $\omega=(0.06056,\,0.00328)$  ,  $\alpha=0.08$  ,  $x_1=0.1978m$  and Re=1350)



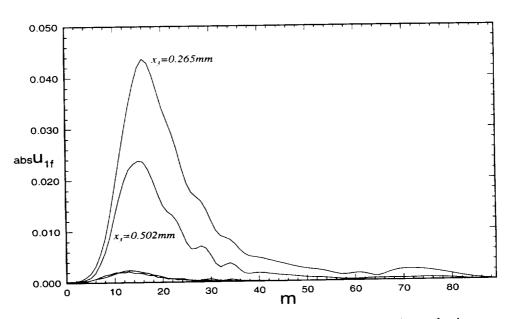
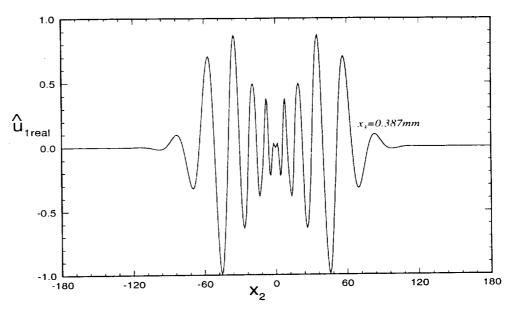


Fig. 4.71 Case 5: The distribution of eigenfunction and Fourier components for a symmetric mode with frequency f=40.35 kHz ,  $\omega=(0.0563,~0.00131)$  ,  $\alpha=0.09$  ,  $x_1=0.1978m$  and Re=1350)



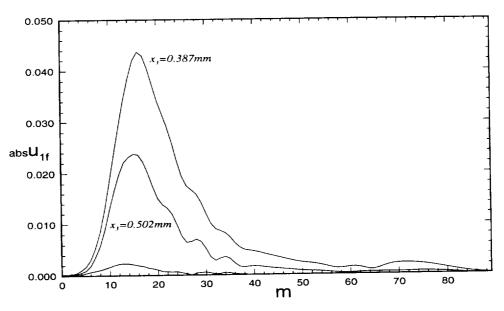


Fig. 4.72 Case 6: The distribution of eigenfunction and Fourier components for a symmetric mode with frequency f=41.14 kHz. ( $\omega=(0.0574,\,0.00115)$ ),  $\alpha=0.09,\,x_1=0.1978m$  and Re=1350)

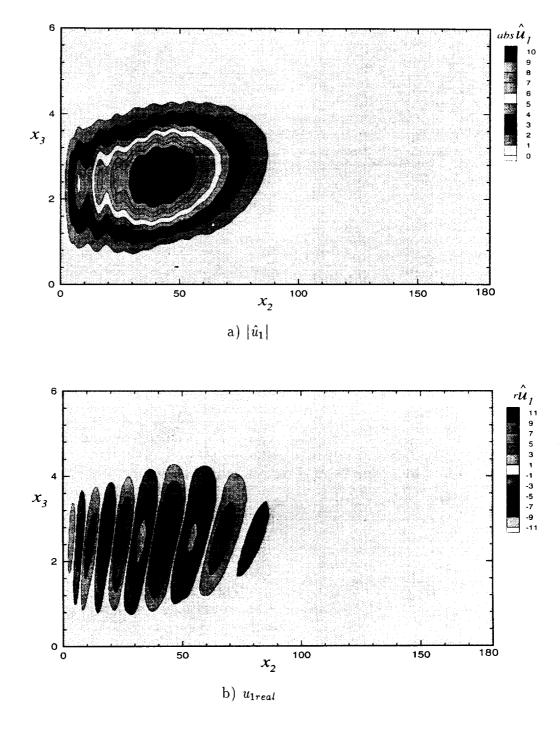
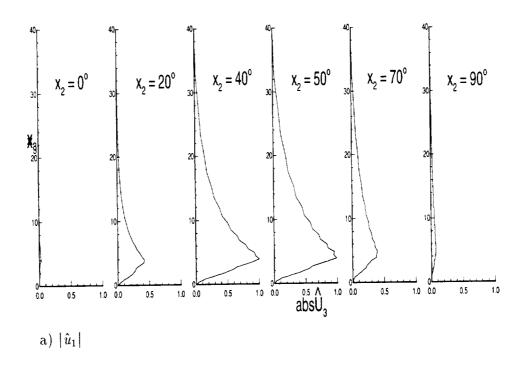


Fig. 4.73 Case 6: Contour plot of streamwise velocity disturbance. (frequency  $f=41.14~\rm{kHz}$  ,  $~\omega=(0.0574,~0.00115)$  ,  $\alpha=0.09$  ,  $x_1=0.1978m$  and ~Re=1350 )



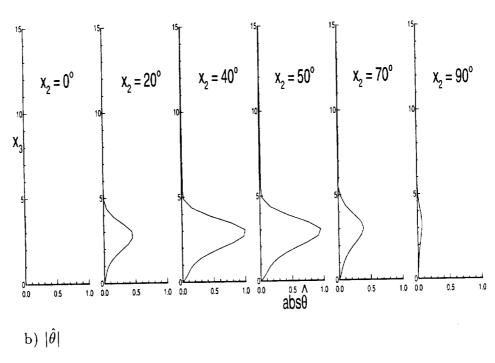
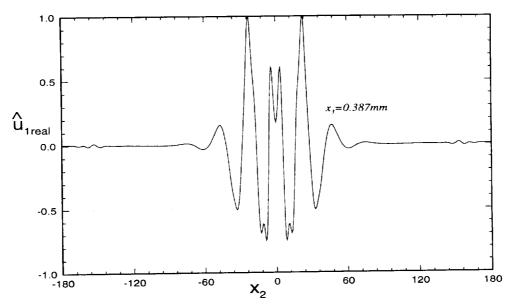


Fig. 4.74 Case 6 : The distribution of disturbance profiles along the azimuthal direction. (frequency  $f=41.14~\mathrm{kHz}$ ,  $\omega=(0.0574,\,0.00115)$ ,  $\alpha=0.09,\,x_1=0.1978m$  and Re=1350)



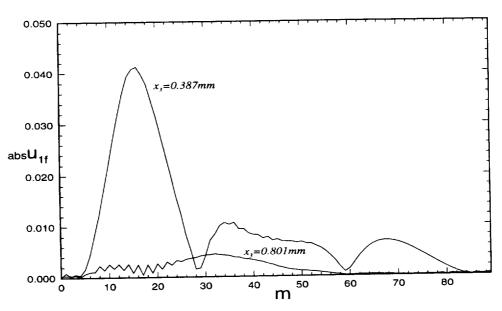


Fig. 4.75 Case 7: The distribution of eigenfunction and Fourier components for a symmetric mode with frequency f=39.16 kHz. ( $\omega=(0.0546,\,0.00161)$ ,  $\alpha=0.09,\,x_1=0.1978m$  and Re=1350)

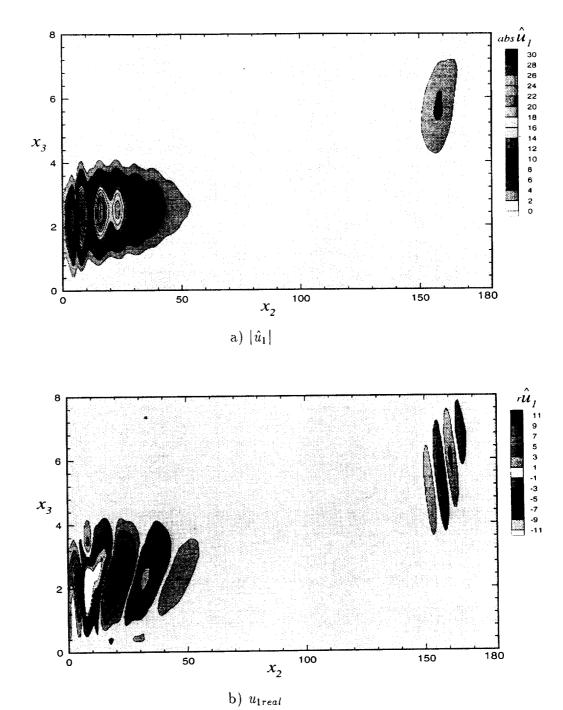
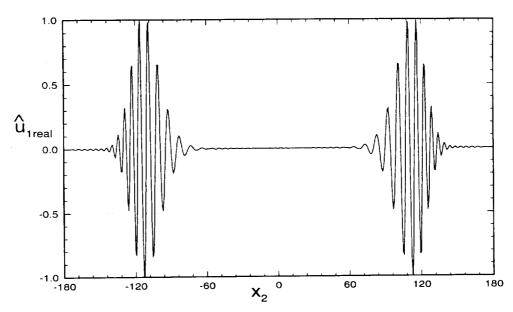


Fig. 4.76 Case 7: Contour plot of streamwise velocity disturbance. (frequency  $f=39.16~\rm{kHz}$  ,  $~\omega=(0.0546,~0.00161)$  ,  $\alpha=0.09$  ,  $x_1=0.1978m$  and ~Re=1350 )



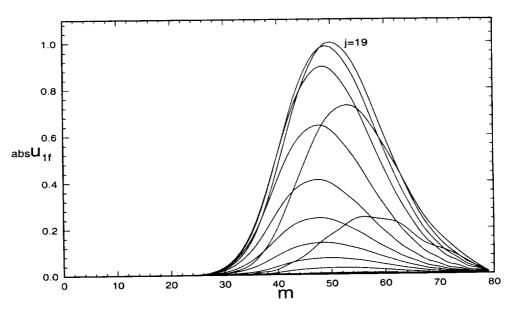


Fig. 4.77 Case 1: The distribution of eigenfunction and Fourier components for a symmetric mode with frequency f=17.45 kHz ,  $\omega=(0.0385,\,0.00445)$  ,  $\alpha=0.07,\,x_1=0.5105m$  and Re=2211)

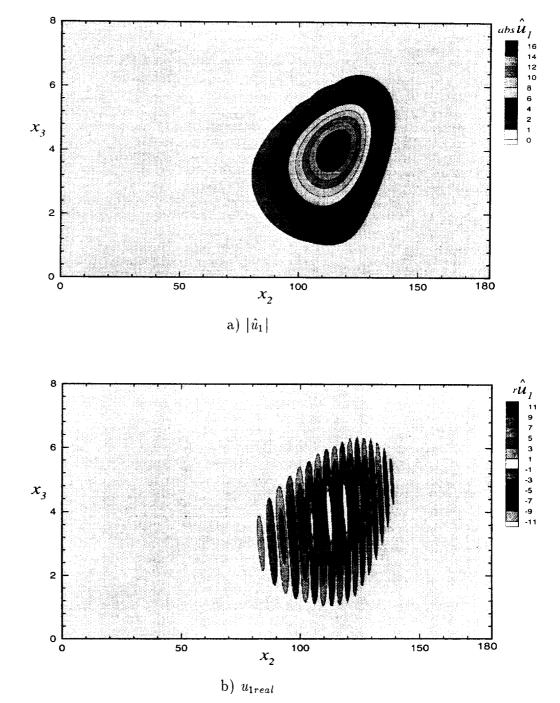
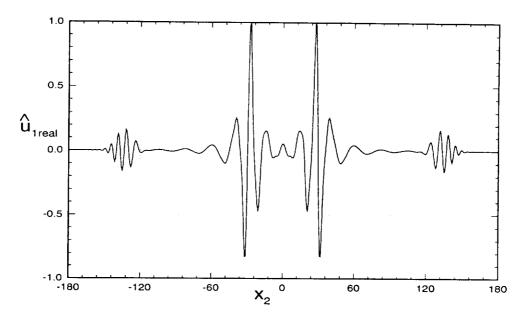


Fig. 4.78 Case 1: Contour plot of streamwise velocity disturbance. (frequency  $f=17.45~\rm{kHz}$  ,  $~\omega=(0.0385,~0.00445)$  ,  $\alpha=0.07$  ,  $x_1=0.5105m$  and ~Re=2211 )



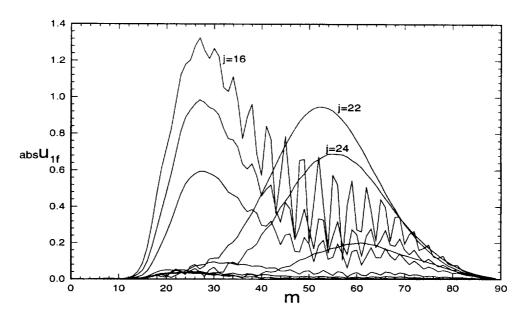


Fig. 4.79 Case 2: The distribution of eigenfunction and Fourier components for an anti-symmetric mode with frequency  $f=19.2~\mathrm{kHz}$ ,  $\omega=(0.0423,\,0.00351)$ ,  $\alpha=0.07,\,x_1=0.5105m$  and Re=2211)

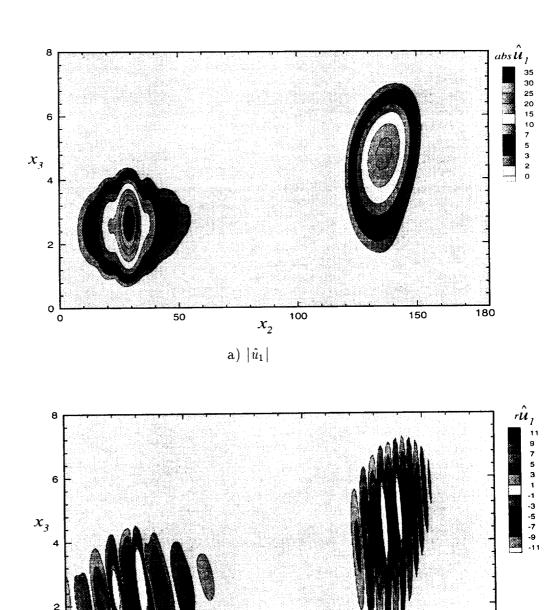
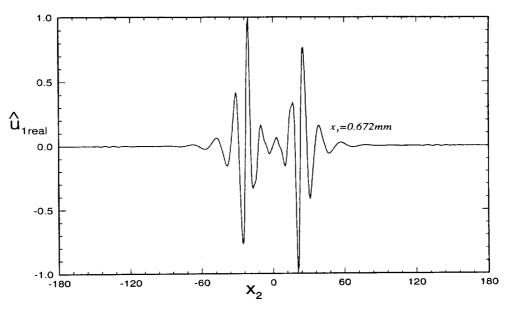


Fig. 4.80 Case 2: Contour plot of streamwise velocity disturbance. (frequency  $f=19.2~\rm kHz$  ,  $~\omega=(0.0423,~0.00351)$  ,  $\alpha=0.07$  ,  $x_1=0.5105m$  and ~Re=2211 )

b)  $u_{1real}$ 

 $x_2$ 



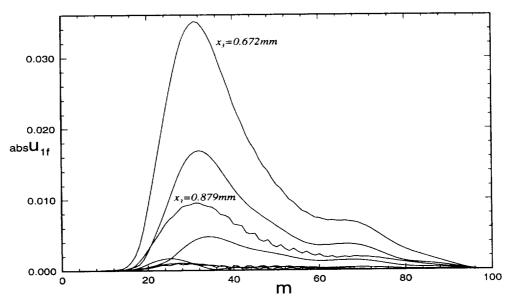


Fig. 4.81 Case 3: The distribution of eigenfunction and Fourier components for an anti-symmetric mode with frequency f=19.04 kHz. ( $\omega=(0.0419,\ 0.00439)$ ,  $\alpha=0.07,\ x_1=0.5105m$  and Re=2211)

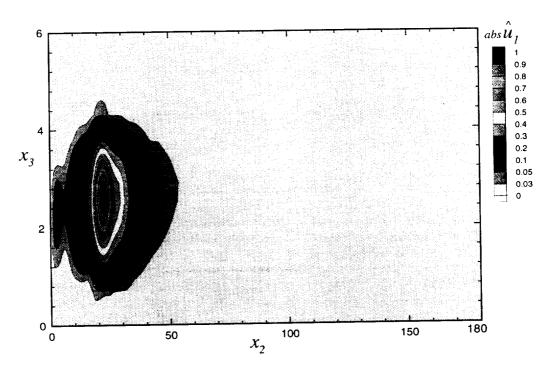
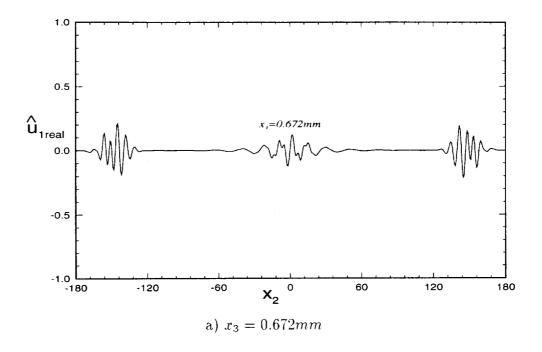


Fig. 4.82 Case 3: Contour plot of streamwise velocity disturbance  $|\hat{u}_1|$ . (frequency f=19.04 kHz ,  $\omega=(0.0419,\,0.00439),\,\alpha=0.07$  ,  $x_1=0.5105m$  and Re=2211 )



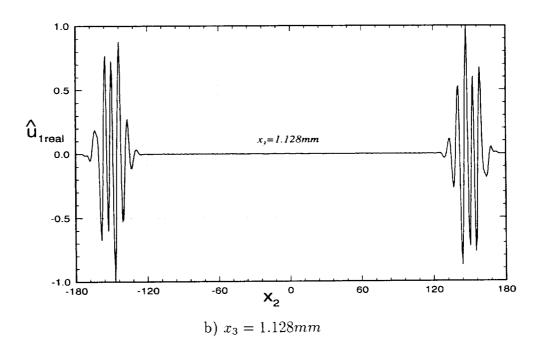


Fig. 4.83 Case 4: The distribution of eigenfunction for an anti-symmetric mode with frequency f=23.03 kHz. (  $\omega=(0.0507,\,0.00288)$  ,  $\alpha=0.08,\,x_1=0.5105m$  and Re=2211)

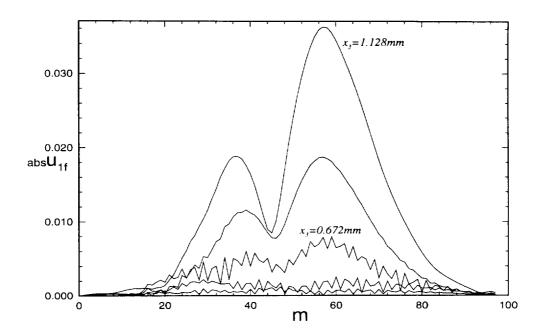


Fig. 4.84 Case 4: The distribution of Fourier components of streamwise velocity disturbance  $|u_{1f}|$  with Fourier modes m. (frequency f=23.03 kHz,  $\omega=(0.0507, 0.00288)$ ,  $\alpha=0.08, x_1=0.5105m$  and Re=2211)

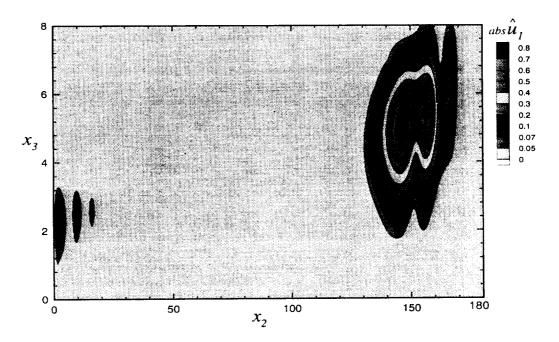
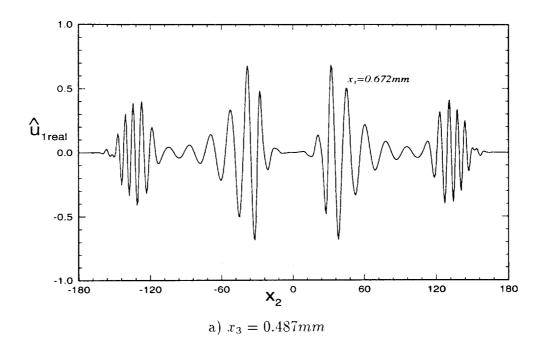


Fig. 4.85 Case 4: Contour plot of streamwise velocity disturbance  $|\hat{u}_1|$ . (frequency f=23.03 kHz,  $\omega=(0.0507,\,0.00288),\,\alpha=0.08,\,x_1=0.5105m$  and Re=2211)



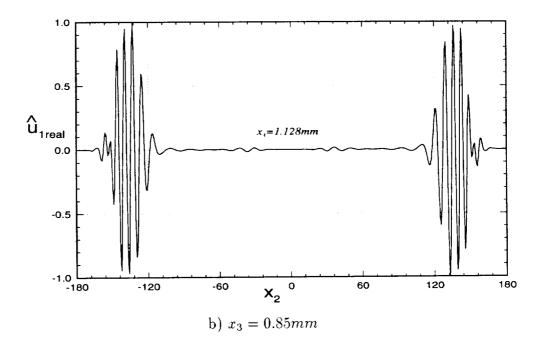


Fig. 4.86 Case 5: The distribution of eigenfunction for an anti-symmetric mode with frequency f=22.04 kHz. (  $\omega=(0.0486,~0.00427)$  ,  $\alpha=0.08$  ,  $x_1=0.5105m$  and Re=2211)

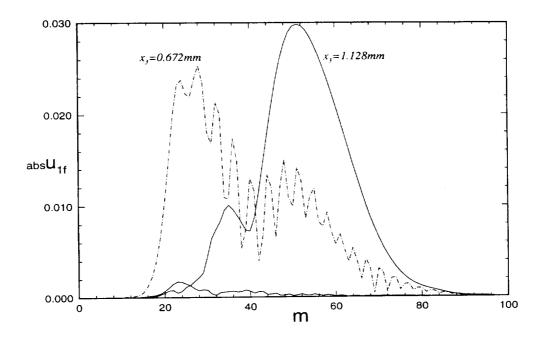


Fig. 4.87 Case 5: The distribution of Fourier components of streamwise velocity disturbance  $|u_{1f}|$  with Fourier modes m. (frequency f=22.04 kHz,  $\omega=(0.0486,0.00427)$ ,  $\alpha=0.08,\,x_1=0.5105m$  and Re=2211)

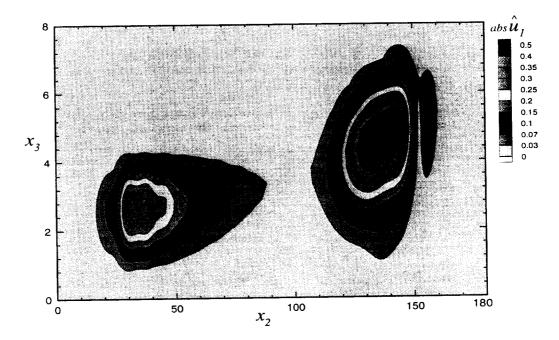
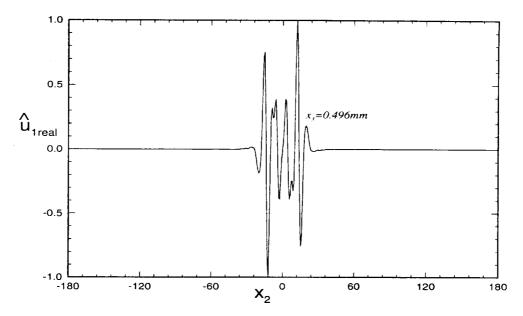
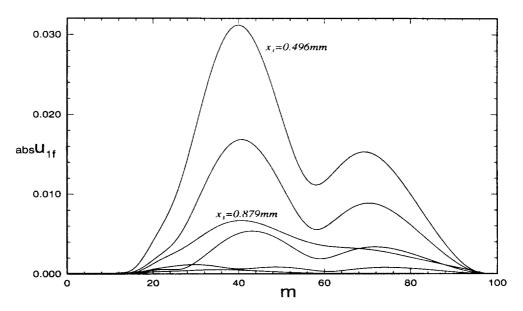


Fig. 4.88 Case 5: Contour plot of streamwise velocity disturbance  $|\hat{u}_1|$ . (frequency f=22.04 kHz,  $\omega=(0.0486,\,0.00427),\,\alpha=0.08,\,x_1=0.5105m$  and Re=2211)



a) The distribution velocity disturbance  $\hat{u}_{1real}$  in the azimuthal direction at wall-normal point  $x_3 = 0.931mm$ , where it has maximum amplitude



b) The distribution of Fourier components of streamwise velocity disturbance  $|u_{1f}|$  with Fourier modes m.

Fig. 4.89 Case 6: The distribution of eigenfunction and Fourier components for an anti-symmetric mode with frequency f=23.45 kHz. ( $\omega=(0.0517,\ 0.00411)$ ,  $\alpha=0.08,\ x_1=0.5105m$  and Re=2211)

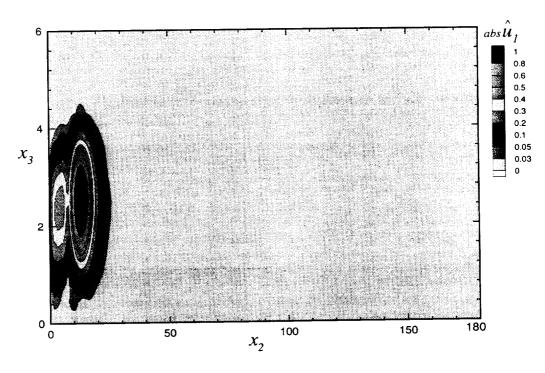


Fig. 4.90 Case 3: Contour plot of streamwise velocity disturbance  $|\hat{u}_1|$ . (frequency  $f=23.45~\mathrm{kHz}$ ,  $\omega=(0.0517,\,0.00411),\,\alpha=0.08$ ,  $x_1=0.5105m$  and Re=2211)

#### CHAPTER 5

#### CONCLUSIONS

A program is developed to investigate the linear stability of three-dimensional compressible boundary layer flows over bodies of revolutions. The problem is formulated as a 2-D eigenvalue problem incorporating the meanflow variations in the normal and azimuthal directions. Thereby, the normal mode solutions are sought in the whole plane perpendicular to the axial direction rather than in a line normal to the wall as is done in the classical theory. The case of a supersonic flow over a sharp cone with 5° half-included angle at 2° angle of attack was considered. The stability computations were done using 1D and 2D eigenvalue methods. In the case of 2D eigenvalue computations Implicitly Restarted Arnoldi Method was used to perform global eigenvalue search and those values were used as guess values for the local 2D eigenvalue computations.

In the first chapter the fundamentals of the linear stability was reviewed. The nature of the instability in compressible and incompressible two-dimensional and three-dimensional boundary layers and the formulations of the stability problems as temporal and spatial problems were explained. Also the general historical review of the research on the stability were mentioned.

Starting from the mathematical formulation of the stability problem of the three-dimensional compressible boundary layer in generalized curvilinear coordinate system, the numerical method and solution procedures for the case of a three-dimensional boundary layer over a sharp cone at an angle of attack were discussed in chapter 2. The problem was formulated as 1D and 2D eigenvalue problem. In chapter 3, the results of meanflow computation over a sharp cone with 5° half-included angle at 2° angle of attack obtained using TLNS3D were presented.

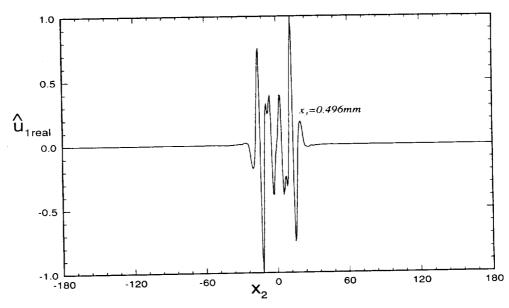
In chapter 4, the results of linear stability computations for the threedimensional compressible boundary layer over a sharp cone at an angle of attack as 1D and 2D eigenvalue method were presented. The stability computations were done at four different stations along the streamwise direction. In 1D eigenvalue problem the stability computations were performed as in classical theory - neglecting the variation of the meanflow in azimuthal and streamwise direction. The 1D stability results showed that the boundary layer region up to  $x_1 = 0.03$ m is stable and most amplified temporal amplification rate occur around  $x_2 = 90^{\circ}$ . Also the effect of crossflow component was noticed to be in the middle region in the azimuthal direction and it manifested itself as increase in the temporal amplification rate around  $x_2 = 90^{\circ}$  for negative mode numbers m and decrease in the temporal amplification rate for positive mode numbers. Unlike the 1D stability results, where the eigenvalue spectrum for a given azimuthal mode number m consisted only a few sparse unstable eigenvalues, the 2D temporal eigenvalue method showed that in the 2D eigenvalue spectrum the unstable eigenvalues were clustered in the complex  $\omega$  plane. Further, the distributions of eigenfunctions along the azimuthal direction were found to clustered in confined regions and were approximately symmetric about  $x_2 = 90^{\circ}$ . Due to the huge memory requirement it is not possible to increase the number of points and the number of modes.

# 5.1 Recommendations for the future work

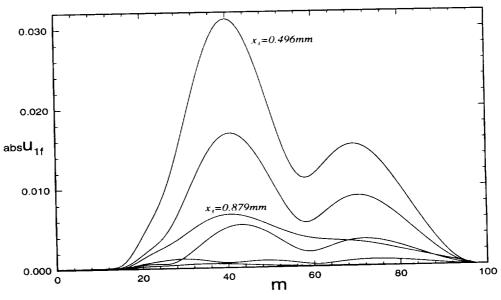
The major barriers in the stability computations as 2D eigenvalue method are required memory and the CPU time. These limitations on the computational resources make the number of Fourier modes and the grid points in the wall normal directions kept to a range. Also, as explained earlier the spatial stability computations need much more memory resources than that of temporal eigenvalue computations.

Thus, the recommendations for the future research are as follows;

- The stability computations of the three-dimensional compressible boundary layers as spatial eigenvalue problem.
- Studying of evolution of each stability mode using PSE methods.
- Computation of N-factor and prediction of transition.
- ullet Introducing a controlled disturbance , such as a point source of the form  $e^{im\theta}$  and studying the evolution of it.



a) The distribution velocity disturbance  $\hat{u}_{1real}$  in the azimuthal direction at wall-normal point  $x_3 = 0.931mm$ , where it has maximum amplitude



b) The distribution of Fourier components of streamwise velocity disturbance  $|u_{1f}|$  with Fourier modes m.

Fig. 4.89 Case 6: The distribution of eigenfunction and Fourier components for an anti-symmetric mode with frequency f=23.45 kHz. ( $\omega=(0.0517,\,0.00411)$ ,  $\alpha=0.08,\,x_1=0.5105m$  and Re=2211)

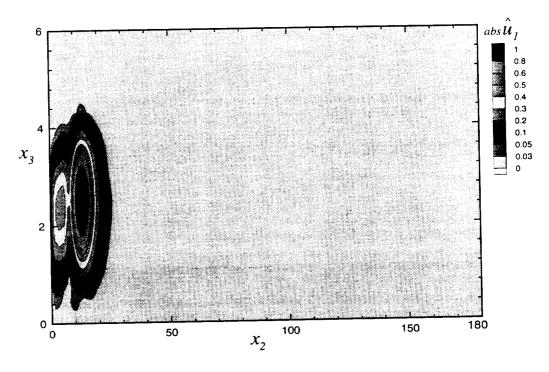


Fig. 4.90 Case 3: Contour plot of streamwise velocity disturbance  $|\hat{u}_1|$ . (frequency  $f=23.45~\mathrm{kHz}$ ,  $\omega=(0.0517,\,0.00411),\,\alpha=0.08$ ,  $x_1=0.5105m$  and Re=2211)

## CHAPTER 5

## CONCLUSIONS

A program is developed to investigate the linear stability of three-dimensional compressible boundary layer flows over bodies of revolutions. The problem is formulated as a 2-D eigenvalue problem incorporating the meanflow variations in the normal and azimuthal directions. Thereby, the normal mode solutions are sought in the whole plane perpendicular to the axial direction rather than in a line normal to the wall as is done in the classical theory. The case of a supersonic flow over a sharp cone with 5° half-included angle at 2° angle of attack was considered. The stability computations were done using 1D and 2D eigenvalue methods. In the case of 2D eigenvalue computations Implicitly Restarted Arnoldi Method was used to perform global eigenvalue search and those values were used as guess values for the local 2D eigenvalue computations.

In the first chapter the fundamentals of the linear stability was reviewed. The nature of the instability in compressible and incompressible two-dimensional and three-dimensional boundary layers and the formulations of the stability problems as temporal and spatial problems were explained. Also the general historical review of the research on the stability were mentioned.

Starting from the mathematical formulation of the stability problem of the three-dimensional compressible boundary layer in generalized curvilinear coordinate system, the numerical method and solution procedures for the case of a three-dimensional boundary layer over a sharp cone at an angle of attack were discussed in chapter 2. The problem was formulated as 1D and 2D eigenvalue problem. In chapter 3, the results of meanflow computation over a sharp cone with 5° half-included angle at 2° angle of attack obtained using TLNS3D were presented.

In chapter 4, the results of linear stability computations for the threedimensional compressible boundary layer over a sharp cone at an angle of attack as 1D and 2D eigenvalue method were presented. The stability computations were done at four different stations along the streamwise direction. In 1D eigenvalue problem the stability computations were performed as in classical theory - neglecting the variation of the meanflow in azimuthal and streamwise direction. The 1D stability results showed that the boundary layer region up to  $x_1$ = 0.03m is stable and most amplified temporal amplification rate occur around  $x_2 = 90^{\circ}$ . Also the effect of crossflow component was noticed to be in the middle region in the azimuthal direction and it manifested itself as increase in the temporal amplification rate around  $x_2 = 90^\circ$  for negative mode numbers m and decrease in the temporal amplification rate for positive mode numbers. Unlike the 1D stability results, where the eigenvalue spectrum for a given azimuthal mode number m consisted only a few sparse unstable eigenvalues, the 2D temporal eigenvalue method showed that in the 2D eigenvalue spectrum the unstable eigenvalues were clustered in the complex  $\omega$  plane. Further, the distributions of eigenfunctions along the azimuthal direction were found to clustered in confined regions and were approximately symmetric about  $x_2 = 90^{\circ}$ . Due to the huge memory requirement it is not possible to increase the number of points and the number of modes.

# 5.1 Recommendations for the future work

The major barriers in the stability computations as 2D eigenvalue method are required memory and the CPU time. These limitations on the computational resources make the number of Fourier modes and the grid points in the wall normal directions kept to a range. Also, as explained earlier the spatial stability computations need much more memory resources than that of temporal eigenvalue computations.

Thus, the recommendations for the future research are as follows;

- The stability computations of the three-dimensional compressible boundary layers as spatial eigenvalue problem.
- Studying of evolution of each stability mode using PSE methods.
- Computation of N-factor and prediction of transition.
- $\bullet$  Introducing a controlled disturbance , such as a point source of the form  $e^{im\theta}$  and studying the evolution of it.

## **BIBLIOGRAPHY**

- [1] Lehoucq, R., Sorensen, D., and Yang, C., "ARPACK Users Guide," fttp://ftp.caam.rice.edu/pub/software/ARPACK, Mar. 1997.
- [2] Vatsa, V. N., Sanetrik, M. D., and Parlette, E. B., "Development of a Flexible and Efficient Multigrid-Based Multiblock Flow Solver," AIAA Paper 93-0677 31th Aerospace Sciences Meeting and Exhibit, Jan. 11-14, 1993/ Reno, NV.
- [3] Vatsa, V. N., and Wedan, B. W., "Development of a Multigrid Code fo 3D Navier-Stokes Equations and its Application to a Grid-Refinement Study," Computers & Fluids, Vol. 18, No. 4, 1990, pp. 391-403.
- [4] Lubard, S. C., and Helliwell, W. S., "Calculation of the Flow on a Cone at Angle of Attack," AIAA Journal, Vol. 12, No. 7, July 1974, pp. 965-974.
- [5] Owen, F. K., and Horstman, C. C., "Comparison of Wing Tunnel Transition and Freestream Disturbance Measurements," AIAA Journal, Vol. 13, No. 3, Mar. 1975, pp. 266-269.
- [6] Poggie, J., and Kimmel, R. L., "Traveling Instability in Elliptic Cone Boundary Layer Transition at Mach 8," AIAA Paper 98-0435, 36th Aerospace Sciences Meeting and Exhibit, Jan. 12-15, 1998/ Reno, NV.
- [7] Poggie, J., and Kimmel, R. L., "Disturbance Evolution and Breakdown to Turbulence in a Hypersonic Boundary Layer: Instantaneous Structure," AIAA Paper 97-0556 35th Aerospace Sciences Meeting and Exhibit, Jan. 6-10, 1997/Reno, NV.

- [8] Scheider, S. P., "Survey of Flight Data for Boundary- Layer Transition at Hypersonic and Supersonic Speeds," AIAA Paper 98-0432, 36th Aerospace Sciences Meeting and Exhibit, Jan. 12-15, 1998/ Reno, NV.
- [9] Stetson, K. F., "Mach 6 Experiments of Transition on a Cone at an Angle of Attack," AIAA paper 81-1226, June 1981.
- [10] Stetson, K. F., Thompson, E. R., Donaldson, J. C., and Siler, L. G., "Laminar Boundary Layer Stability Experiments on a Cone at Mach 8, Part1: Sharp Cone," AIAA Paper No. 83-1761, July 1983.
- [11] Stetson, K. F., Thompson, E. R., Donaldson, J. C., and Siler, L. G., "Laminar Boundary Layer Stability Experiments on a Cone at Mach 8, Part2: Blunt Cone," AIAA Paper No. 84-006, Jan. 1984.
- [12] Stetson, K. F., Thompson, E. R., Donaldson, J. C., and Siler, L. G., "Laminar Boundary Layer Stability Experiments on a Cone at Mach 8, Part3: Sharp Cone at Agle of Attack," AIAA Paper No. 85-0492, Jan 1985.
- [13] Stetson, K. F., Thompson, E. R., Donaldson, J. C., and Siler, L. G., "Laminar Boundary Layer Stability Experiments on a Cone at Mach 8, Part4: On Unit Reynolds Number and Environmental Effects," AIAA Paper No. 86-1087. May 1986.
- [14] Stetson, K. F., Thompson, E. R., Donaldson, J. C., and Siler, L. G., "Laminar Boundary-Layer Stability Experiments on a cone at Mach 8, Part 5: Tests with cooled Model," AIAA Paper 89-1895, 20th Fluid Dynamics, Plasma Dynamics and Laser Conference, Jun. 12-14, 1989/ Buffalo, New York.

- [15] Stetson, K. F., and Kimmel, R. L., "On Hypersonic Boundary-Layer Stability," AIAA Paper 92-0737, 30th Aerospace Sciences Meetingand Exhibit, Jan. 6-9, 1992/ Reno, NV.
- [16] Cebeci, T., Chen, H. H., Arnal, D., and Haung, T. T., "Three-Dimensional Linear Stability Approach to Transition on Wings and Bodies of Revolution at Incidence," AIAA Journal, Vol. 29, No. 12, Dec. 1991, pp. 2077-2085.
- [17] Potter, J. L., "Boundary-Layer Transition on Supersonic Cones at Aeroballistic Range," AIAA Journal, Vol. 13, No. 3, March 1975, pp. 270-277.
- [18] Potter, J. L., "The Unit Reynolds Number Effect on Boundary-Layer Transition," Dissertation submitted in partial fulfillment of the requirements for the degree of Doctor of Philosophy, Vanderbit University, May 1974.
- [19] Balakumar, P., and Reed H. L., "Stability of Three-Dimensional Supersonic Boundary Layers," Physics of Fluids, Vol. 3, No. 4, Apr. 1991, pp. 617-632.
- [20] Moore, F. K., "Laminar Boundary Layer on a Circular Cone in Supersonic Flow at a Small Angle of Attack," NACA Technical Note 2521, Oct. 1951.
- [21] Kimmel, R. L., Schwoerke, S. N., and Klein, M. A., "Three-Dimensional Hypersonic Laminar Boundary Layer Computations for Transition Experiment Design," AIAA Paper 96-2080, 27th Aerospace Sciences Meeting and Exhibit, Jun. 17-20, 1996/ New Orleans, LA.
- [22] Kimmel, R. L., and Poggie, J., "Disturbance Evolution and Breakdown to Turbulence in a Hypersonic Boundary Layer: Ensemble-Averaged Structure," AIAA Paper 97-0555, 35th Aerospace Sciences Meeting and Exhibit, Jan. 6-10, 1997/ Reno, NV.

- [23] Dogget, G. P., and Chokani, N., "Effect of Angle of Attack on Hypersonic Boundary-Layer Stability," AIAA Journal, Vol. 35, No. 3, Mar. 1997, pp. 464-470.
- [24] Lin, T. C., and Rubin, S. G., "Viscous Flow over Spinning Cones at Angle of Attack," AIAA Journal, Vol. 12, No. 7, Jul. 1974, pp. 975-985.
- [25] Lin, T. C., and Rubin, S. G., "Viscous Flow over a Cone at Moderate Incidence. Part 1. Hypersonic Tip Region," Computer & Fluids, Pergamon Press. Vol. 1, 1973, pp. 37-57.
- [26] Lin, T. C., and Rubin, S. G., "Viscous Flow over a Cone at Moderate Incidence. Part 2.Supersonic Boundary Layer," Journal of Fluid Mechanics, Vol. 59, part 3, 1973, pp. 593-620.
- [27] Schiff, L. B., and Stegger, J. L., "Numerical Simulation of Steady Supersonic Viscous Flow," AIAA Journal, Vol. 18, No. 12, Dec. 1990, pp. 1421-1430.
- [28] Nietubicz, C. J., Pulliam, T. H., and Steger, J. L., "Numerical Solution of the Azimuthal-Invariant Thin-Layer Navier- Stokes Equations," AIAA Paper 79-0010, 17th Aerospace Sciences Meeting, Jan. 15-17, 1979/ New Orleans, LA.
- [29] Rubin, S. G., and Lin, T. C., "A Numerical Method for Three- Dimensional Viscous Flow: Application to the Hypersonic Leading Edge," *Journal of Com*putational Physics, Vol. 9, 1972, pp. 339-364.
- [30] Trella, M., and Libby, P. A., "Similar Solutions for the Hypersonic Laminar Boundary Layer Near a Plane of Symmetry," AIAA Journal, Vol. 3, No. 1, Jan. 1965, pp. 75-90.

- [31] Helliwell, W. S., Dickinson, R. P., and Lubard, S. C., "Viscous Flow Over Arbitrary Geometries at High Angle of Attack," AIAA Paper 80-0064, 18th Aerospace Sciences Meeting, Jan. 14-16, 1980/ Pasadena, CA.
- [32] Anderson, D. A., Tannehill, J. C., and Pletcher, R. H., Computational Fluid Mechanics and Heat Transfer, McGraw-Hill Book Company, 1984.
- [33] Herbert, T., "Boundary-Layer Transition-Analysis and Prediction Revisited," AIAA Paper 91-0737, 1991.
- [34] Malik, M. R., "Numerical Methods in Hypersonic boundary layer Stability." Journal of Computational Physics, Vol. 86, No.2, Feb. 1990, pp. 376-412.
- [35] Hefner, J. N., and Bushnell, D. M., "Application of Stability Theory to Laminar Flow Control," AIAA paper 79-1493, 1979.
- [36] Goldstein, M.E., "The evolution of Tollmien-Schlichting waves near a leading edge," Journal of Fluid Mechanics, Vol. 127, 1983, pp. 59-81.
- [37] Goldstein, M.E., "Scattering of acoustic waves into Tollmien-Schlichting waves by small streamwise variations in surface geometry," *Journal of Fluid Mechanics*, Vol. 154, 1985, pp. 509-529.
- [38] Herbert, T., "Secondary instability of boundary layers," Annual Review of Fluid Mechanics, Vol. 20, 1998, pp. 487-526.
- [39] Rayleigh, Lord, "On the stability, or instability, of certain fluid motions," Proceeding of London Mathematics Society," Vol. 11, pp. 55-70.
- [40] Gregory, N., Stuart, J. T., and Walker, W. S., "On the Stability of Three-dimensional boundary layers with application to the flow due to a rotating disk,"

- Philosophical Transaction of the Royal Society of London, Vol. 248, No. 943, July 1995, pp. 155-199.
- [41] Lees, L., and Lin, C. C., "Investigation of the Laminar Boundary Layer in a Compressible Fluid," NACA Technical Note, Vol. 83, Sept. 1946, pp. 115.
- [42] Lees, L., and Reshotko, E., "Stability of Compressible Boundary Layer," *Journal of Fluid Mechanics*, Vol. 12, 1962, pp. 455-477.
- [43] Mack, L., "Boundary layer on stability theory," Nov. 1969, JPL Report No. 900-277.
- [44] Gaponov, M. C., and Weinstein, L. M., "The Influence of Flow Non-parallelism on Disturbance Development in the Supersonic Boundary Layer," Prc. of the 8th Canadian Congress of Applied Mechanics, 1981, pp. 673-674.
- [45] Malik, M. R., and Spall, R. E., "On the Stability of Compressible Flow Past Axisymmetric Bodies," High Technology Report No. HTC-8905, Oct. 1989.
- [46] Saric, W., and Nayfeh, A., "Nonparallel stability of boundary layers with pressure gradients and suction," AGARD Report No.224, 1998, pp. 6.1-6.21
- [47] Gaster, M., "On the effects of boundary layer growth on flow stability," *Journal of Fluid Mechanics*, Vol. 66, 1974, pp. 465-480.
- [48] El-Hady, N. M., "Nonparallel Instability of Supersonic and Hypersonic Boundary Layers," Physics of Fluid, Vol. 3, No.9, 1991, pp. 2164-2178.
- [49] Fasel, H., "Numerical Investigation of the Three-Dimensional Development in Boundary-Layer Transition", AIAA Journal Vol. 28, No. 1, Jan. 1990, pp. 29-37.

- [50] Fasel, H., "Investigation of the stability of boundary layers by a finite-difference model of the Navier-Stokes Equations," Journal of Fluid Mechanics, Vol. 78, 1976, pp. 355-383.
- [51] Joslin , R. D., "Direct simulation of evolution and control of three-dimensional instabilities in attachment-line boundary layers," Journal of Fluid Mechanics. Vol. 291, 1995b , pp. 369.
- [52] Joslin , R. D. , Streett, C. L., and Chang, C. L., "Spatial direct numerical simulation of boundary layer transition mechanism: validation of PSE theory," Theoretical Computational Fluid Dynamics, Vol.4, 1993, pp. 271.
- [53] Herbert, T., "Parabolized stability equations," Annual Review of Fluid Mechanics, Vol. 29, 1997, pp. 245-283.
- [54] King, R. A., "Three-dimensional boundary-layer transition on a cone at Mach 3.5," Experiments in Fluids, Vol. 3, 1992, pp. 305-314.
- [55] Krogmann, P., "An Experimental Study of Boundary Layer Transition on a Slender Cone at Mach 5," AGARD conference proceedings No.224, Laminar Turbulent Transition, May 1977